Upper-mantle anisotropy in the southeastern margin of the Tibetan Plateau revealed by fullwave SKS splitting intensity tomography

Yi Lin[1] and Li Zhao[2]

[1]Chengdu University of Technology
[2]Peking University

March 04, 2024

Abstract

The southeastern margin of the Tibetan Plateau has experienced complex deformation since the Cenozoic, resulting in a high level of seismicity and seismic hazard. Knowledge about the seismic anisotropy provides important insight into the deformation mechanism and the regional seismotectonics beneath this tectonically active region. In this study, we conduct a fullwave multi-scale tomography to investigate the seismic anisotropy in the southeastern margin of the Tibetan Plateau. Broadband records from 470 teleseismic events at 111 permanent stations in the region are used to obtain 5,216 high-quality SKS splitting intensity measurements, which are then inverted in conjunction with 3D sensitivity kernels to obtain the anisotropic model for the region with a multi-scale resolution. Resolution tests show that our dataset recovers anisotropy anomalies reasonably well on the scale of 1° x 1° horizontally and ~100 km vertically. Our result suggests that in the southeastern margin of the Tibetan Plateau the deformations in the lithosphere and asthenosphere are decoupled. The anisotropy in the lithosphere varies both laterally and vertically as a result of the dynamic interactions of neighboring blocks as well as lithospheric reactivation. The anisotropy in the asthenosphere largely follows the direction of regional absolute plate motion, i.e. southeastward under the Songpan-Ganzi Terrane and the Yangtze Craton and nearly east-west south of 26°N latitude. The SKS splitting observed at the surface can be interpreted as the vertical integration of the contributions from lithosphere and asthenosphere.

Upper-mantle anisotropy in the southeastern margin of the Tibetan Plateau revealed by fullwave SKS splitting intensity tomography

Yi Lin[1,2], Li Zhao[1,3]

[1] School of Earth and Space Sciences, Peking University, Beijing 100871, China.

[2] Key Laboratory of Earth Exploration and Information Techniques of the China Ministry of Education, Chengdu University of Technology, Chengdu 610059, China.

[3] Hebei Hongshan National Geophysical Observatory, Peking University, Beijing 100871, China.

Corresponding author: L. Zhao (lizhaopku@pku.edu.cn)

Key Points:

- A 3D shear-wave anisotropy model for the SE margin of the Tibetan Plateau is obtained by fullwave SKS splitting intensity tomography
- Anisotropy distribution shows a decoupling of the deformations in the lithosphere and asthenosphere
- Lithospheric anisotropy has a complex pattern, whereas asthenospheric anisotropy follows the APM

Abstract

The southeastern margin of the Tibetan Plateau has experienced complex deformation since the Cenozoic, resulting in a high level of seismicity and seismic hazard. Knowledge about the seismic anisotropy provides important insight into the deformation mechanism and the regional seismotectonics beneath this tectonically active region. In this study, we conduct a fullwave multi-scale tomography to investigate the seismic anisotropy in the southeastern margin of the Tibetan Plateau. Broadband records from 470 teleseismic events at 111 permanent stations in the region are used to obtain 5,216 high-quality SKS splitting intensity measurements, which are then inverted in conjunction with 3D sensitivity kernels to obtain the anisotropic model for the region with a multi-scale resolution. Resolution tests show that our dataset recovers anisotropy anomalies reasonably well on the scale of 1º x 1º horizontally and ~100 km vertically. Our result suggests that in the southeastern margin of the Tibetan Plateau the deformations in the lithosphere and asthenosphere are decoupled. The anisotropy in the lithosphere varies both laterally and vertically as a result of the dynamic interactions of neighboring blocks as well as lithospheric reactivation. The anisotropy in the asthenosphere largely follows the direction of regional absolute plate motion, i.e. southeastward under the Songpan-Ganzi Terrane and the Yangtze Craton and nearly east-west south of 26ºN latitude. The SKS splitting observed at the surface can be interpreted as the vertical integration of the contributions from lithosphere and asthenosphere.

Keywords: seismic anisotropy; splitting intensity; finite-frequency; fullwave tomography; southeastern Tibetan Plateau

Plain Language Summary

The southeastern margin of the Tibetan Plateau has experienced significant deformation since the

44   Cenozoic due to the collision with the Indian Plate in the south and interactions with the Yangtze

45   Craton in the east. Knowledge about the upper mantle seismic anisotropy helps us understand the

46   reginoal deformation and dynamic evolution. In this study, we conduct a fullwave multi-scale

47   anisotropy tomography for the southeastern margin of the Tibetan Plateau using 5,216 high-quality

48   SKS splitting intensity measurements obtained from the broadband records of 470 teleseismic events

49   at 111 stations. Our result shows a decoupling between the lithosphere and asthenosphere deformations

50   in the southeastern margin of the Tibetan Plateau. The anisotropy in the lithosphere varies both laterally

51   and vertically as a result of the dynamic interactions of neighboring blocks as well as lithospheric

52   reactivation. The anisotropy in the asthenosphere is largely parallel to the regional absolute plate motion,

53   and the SKS splitting observed at the surface is the result of vertical integration of the contributions

54   from lithosphere and asthenosphere.
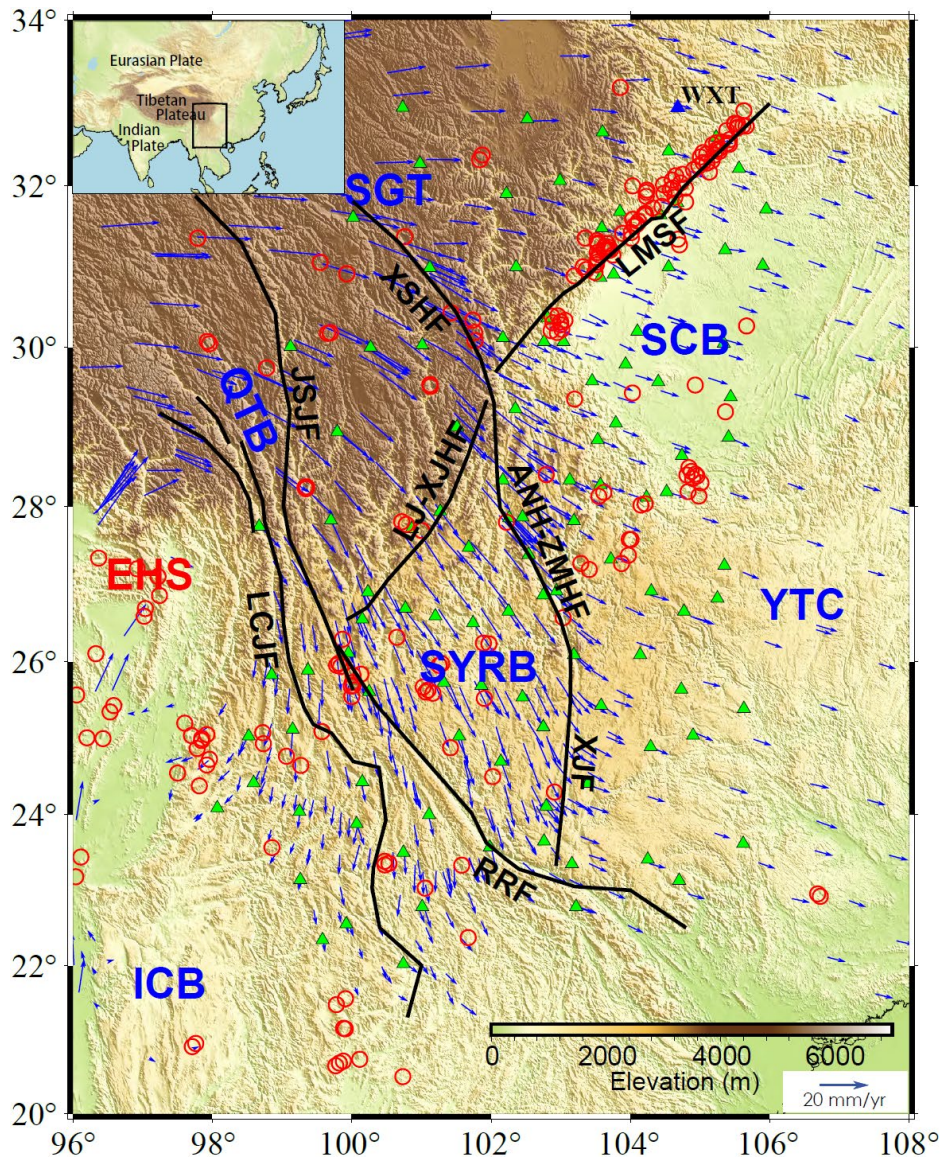
55

56   **1 Introduction**

57   The ongoing Indian-Eurasian continental collision since 50 Ma has resulted in the greatest plateau

58   on Earth and deformed large parts of central and east Asia (Yin & Harrison, 2000; Kind et al.,

59   2002). Despite decades of study, questions remain over the dynamics of the lithospheric

60   deformation and asthenosphere flow beneath the Tibetan Plateau and the surrounding regions

61   (Royden et al., 2008).

62   The region in the southeastern margin of the Tibetan Plateau involves many active tectonic

63   blocks (Figure 1), including the Songpan-Ganzi Terrane (SGT), the Sichuan Basin (SCB), the

64   Sichuan-Yunnan Rhombic Block (SYRB), the Indo-China Block (ICB), the Qiangtang Block

65   (QTB), and the Yangtze Craton (YTC). The SGT is part of central Tibetan Plateau. Its eastern part

66   is separated from the SCB and SYRB by the Longmenshan Fault (LMSF) and Lijiang-Xiaojinhe Fault

67   (LJ-XJHF), respectively, and bounded in the south by the Jinshajiang Fault (JSJF) from the QTB. The

68   convergence between the Indian and Eurasian plates caused the SGT to expand eastward against

69   the SCB during the Cenozoic (Yin & Harrison, 2000). GPS observations show eastward crustal

70   motion of the eastern SGT with the crustal strain rate decreasing abruptly from ~20 mm/year

71   (relative to the YTC reference frame) in the interior SGT to ~3–4 mm/year or less in the vicinity of

72   central and southern segments of the LMSF, indicating that the eastward expansion of the SGT is

73   apparently resisted by the SCB (Shen et al., 2005; Zhang, 2013). Low-velocity zones and high-

74   conductivity bodies in the mid-lower crust under the SGT revealed by geophysical studies (Zhao

75   et al., 2012; Bao et al., 2020) suggest the existence of mid-lower crustal flow. However, these

76   geophysical anomalies exhibit strong lateral heterogeneity in eastern Tibet, implying a complex

77   internal deformation process. The SCB and SYRB are both parts of the YTC (Zhang et al., 2013;

78   Li et al., 2021). The former forms the rigid and stable northwestern margin of the YTC, while the

79   crust of the latter is extruding southeastward along the Anninghe-Zemuhe Fault (ANH-ZMHF) and

80   Xiaojiang Fault (XJF) in the east and the Red River Fault (RRF) in the southwest (Zhang et al., 2003).

81   The Lancangjiang Fault (LCJF) separates the narrow QTB in the east and the ICB in the west.

82   Crustal movements are predominantly characterized by a clockwise rotation around the Eastern

83   Himalayan Syntaxis (EHS), transforming the movement of the plateau material from eastward

84   north of the syntaxis to southeastward and southward further south (Wang & Shen, 2020).
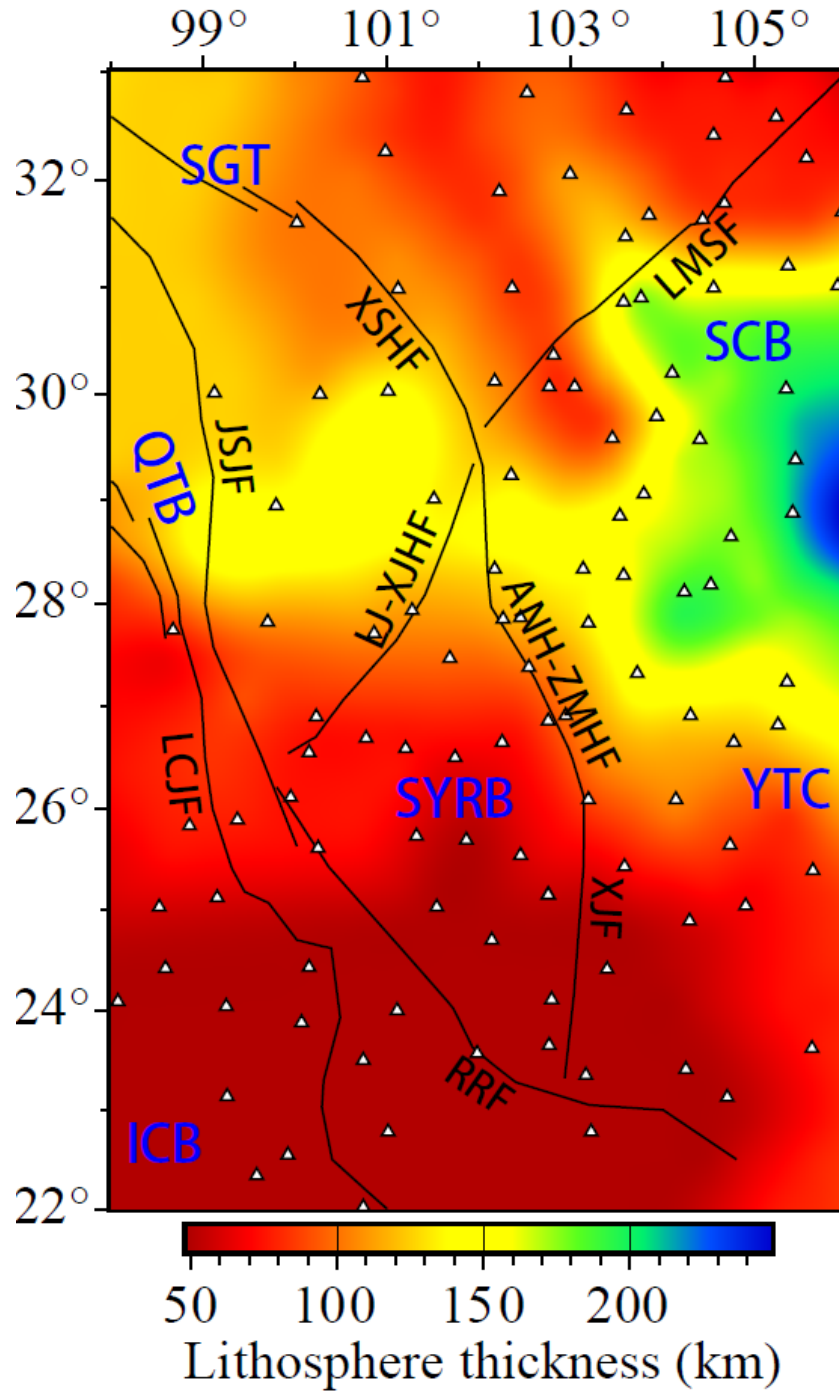

86   **Figure 1**. Map of the tectonic environment of southeastern margin of the Tibetan Plateau with

87   seismic stations (green-filled triangles) and epicenters (red open circles) of earthquakes of

88   magnitude 5 and above from 2000 to 2022. The blue triangle marks the station WXT for which

89   SKS waveforms, splitting intensities and sensitivity kernels are shown in Figures 4, 5 and 7,

90   respectively. Major active faults are shown by thick black lines with abbreviated names in black,

91   including LMSF: Longmenshan Fault; XSHF: Xianshuihe Fault; JSJF: Jinshajiang Fault; LCJF:

92   Lancangjiang Fault; LJ-XJHF: Lijiang-Xiaojinhe Fault; ANH-ZMHF: Anninghe-Zemuhe Fault;

93   XJF: Xiaojiang Fault; and RRF: Red River Fault. Major active tectonic blocks are indicated by

94   abbreviated texts in blue, including SGT: Songpan-Ganzi Terrane; SCB: Sichuan Basin; QTB:

95   Qiangtang Block; SYRB: Sichuan-Yunnan Rhombic Block; YTC: Yangtze Craton; and ICB:

96   Indo-China Block. EHS stands for the Eastern Himalaya Syntax. Blue arrows show the GPS

97   velocities with respect to the Eurasian Plate (Wang & Shen, 2020). Background color shows the

98   topography. The black box in the inset map indicates the location of the main figure.

99   Over the past two decades, and in particular after the 12 May 2008 Wenchuan Mw7.9

100   earthquake on the LMSF, a large number of seismic stations have been deployed in the

101   southeastern margin of the Tibetan Plateau. Waveforms recorded by the growing number of

102   broadband stations have provided crucial data for studying the structure and dynamics of the crust

103   and upper mantle beneath the region, such as the variation in crustal thickness (Wang et al., 2017;

104   Xu et al., 2020), the widespread low-velocity anomalies in mid-lower crust revealed by receiver

105   function analysis (Hu et al., 2005; Xu et al., 2007; Zhang et al., 2009; Wang et al., 2010), Lg-wave

106   high-attenuation zones (Zhao et al., 2013; Wei & Zhao, 2019), joint inversion of receiver function

107   and surface wave dispersion (Liu et al., 2014), and body- and surface-wave tomographies (Huang et

108   al., 2002; Wang et al., 2003; Huang et al., 2009; Li et al., 2009; Wei & Zhao, 2022; Yang et al., 2019).

109   Across the LMSF, the drastic change in elevation from ~5–6 km in the west to a few hundred

110   meters in the east suggests large variation in the lithospheric thickness. Figure 2 shows the

111   LITHO1.0 model (Pasyanos et al., 2014) in the study region, where the lithosphere has a thickness

112   of less than 100 km in the northern and southern parts but ~150 km in mid latitudes. The thickest

113   lithosphere in the study region is more than 200 km beneath the SCB.

Figure 2. Lithosphere thickness in model LITHO1.0 (Pasyanos et al., 2014). Names of major faults and tectonic blocks are the same as in Figure 1.

Distribution of azimuthal anisotropy is an important proxy for deformation. There have been numerous studies devoted to the crustal anisotropy beneath the southeastern Tibetan Plateau

119   utilizing different methods, such as the Pms splitting (Sun et al., 2012; Cai et al., 2016; Han et al.,

120   2020), anisotropic tomography of P and Pn waves (Lei et al., 2014; Huang et al., 2018), surface

121   wave anisotropic tomography (Yang et al., 2010; Yao et al., 2010; Legendre et al., 2015; Zhang et

122   al., 2023), and the splitting of shear waves (Shi et al., 2012). In the upper crust, the fast axis directions

123   are mainly parallel to the strike of active faults (e.g., Yao et al., 2010; Shi et al., 2012; Huang et al.,

124   2018), whereas the anisotropic pattern in the lower crust is different. Huang et al. (2018) showed

125   that the fast velocity direction deviates from the strikes of active faults significantly using P-wave

126   anisotropic tomography. Han et al. (2020) used the Markov-chain Monte Carlo inversion of receiver

127   functions to isolate the effect of potential dipping interfaces. Their results showed that the fast axis

128   directions in the lower crust are in good agreement with the topography contours, implying that the

129   gravitational potential may be the driving force for the crustal deformation in southeastern Tibet.

130   The XKS-wave splitting is routinely used to probe the anisotropic structure in the upper mantle

131   (Long & Becker, 2010). Flesch et al. (2005) conducted joint analysis of GPS, surface geology and

132   shear-wave splitting measurements to argue for a vertically coherent deformation in the crust and

133   upper mantle in the Tibetan Plateau but a decoupling beneath Yunnan Province in southwestern

134   China. Lev et al. (2006) also supported the decoupling beneath Yunnan using shear-wave splitting

135   observations, but they were not able to constrain the level of coupling beneath the Tibetan Plateau.

136   Based on a joint analysis using more shear-wave splitting measurements and GPS observations,

137   Wang et al. (2008) argued for the crust-mantle coupling in the Tibetan Plateau and the surrounding

138   regions.

139   Substantial efforts have been made to develop a theoretical framework as well as practical

140   strategies for the inversion of 3D distribution of anisotropy. A fullwave approach has been developed

141   for the measurement of shear-wave splitting intensities and interpretation in terms of shear-wave

142   azimuthal anisotropy parameters (Chevrot, 2000; Favier & Chevrot, 2003; Chevrot, 2006; Sieminski

143   et al., 2008; Monteiller & Chevrot, 2011; Lin et al., 2014a), which has been applied to anisotropy

144   tomographies for southern California (Monteiller & Chevrot, 2011; Lin et al., 2014b), the High

145   Lava Plain (Mondal & Long, 2020), and the southeastern Tibetan Plateau (Huang & Chevrot,

146   2021). The depth variations of anisotropy obtained by these studies have shed new lights in

147   understanding the sources of anisotropy and the associated mantle dynamics.

148   In this study, we conduct a fullwave multiscale anisotropy tomography for the southeastern

149   margin of the Tibet Plateau. We collect seismic records at regional permanent broadband

150   stations from globally distributed earthquakes and obtain high-quality measurements of SKS

151   splitting intensities. We then invert the splitting intensities using a wavelet-based parameterization

152   of the 3D model to achieve a multi-scale resolution to the anisotropic structure. We also provide

153   an interpretation of our anisotropic model for the southeastern margin of the Tibet Plateau in

154   terms of regional geodynamics.

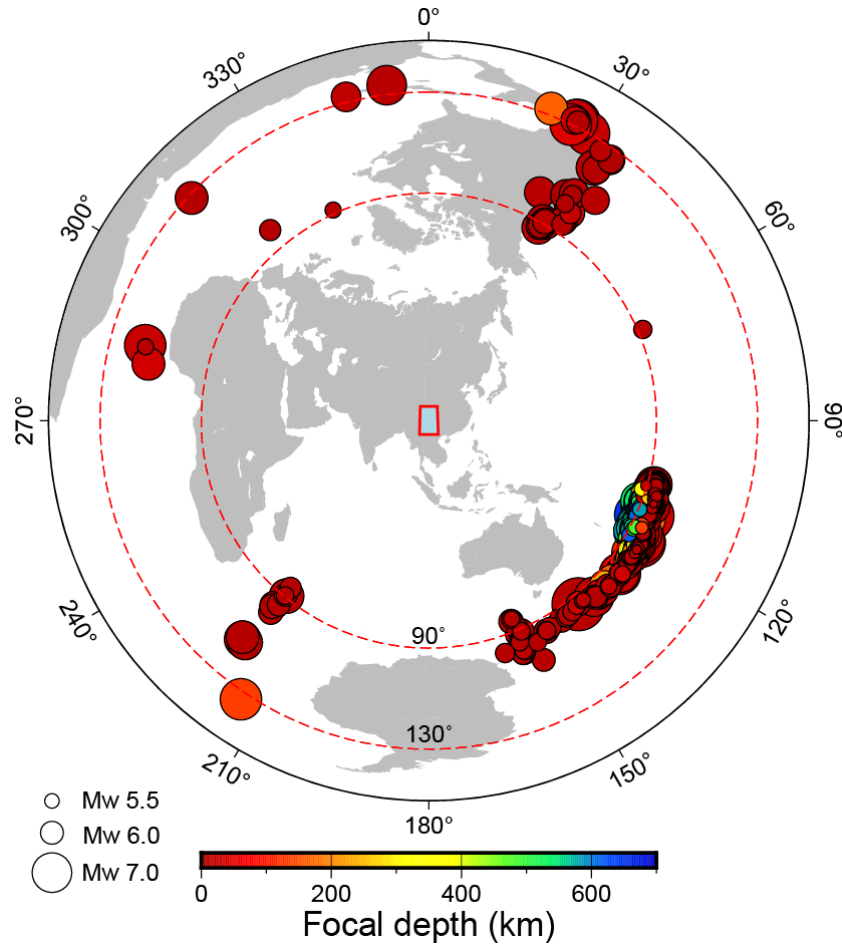155   **2 Data and Methods**

156   **2.1 Waveform records**

157   We collect waveforms recorded by 111 permanent broadband stations (green triangles in Figure 1)

158   deployed in the study region. To guarantee a wide range of azimuthal distribution, we select events

159   of magnitude Mw ≥ 5.5 from 2009 to 2020, located in the epicentral distance range of 90°–130°.

160   After quality control of the waveforms and removal of outliers of the data (see Section 2.2), a total

161   of 470 events are used in the subsequent inversions. Figure 3 displays the event distribution.

162   **2.2 Splitting intensity measurements**

163   Shear wave splitting measurement is nowadays a routine procedure in the study of seismic

164   anisotropy. Several previous studies have documented the measured SKS splitting parameters (fast

165   directions and delay times) at stations in our study region (e.g., Chang et al., 2015; Yang et al.,

166   2018; Liu et al., 2020; Huang & Chevrot, 2021; Li et al., 2021). In this study, we invert for the

167   3D anisotropy structure using the splitting intensity (SI) measurements obtained by computing the

168   zero-lag cross-correlation between the transverse-component record and the time derivative of the

169   radial-component record (Chevrot, 2000).

170

171   **Figure 3**. Distribution of 470 teleseismic events used for SKS splitting intensity inversion in this

172   study. Events of magnitudes Mw5.5 and greater in the epicentral distance range of 90°–130° during

173   2009–2020 are selected. The red box in the center indicates the study area.

174   For a given station, the SI of the SKS wave from the *i*-th event is defined as

$$S_i = -2 \frac{\int_{t_{i1}}^{t_{i2}} \dot{u}_i^R(t) u_i^T(t) dt}{\int_{t_{i1}}^{t_{i2}} [\dot{u}_i^R(t)]^2 dt}, \tag{1}$$

175

176   where $[t_{i1}, t_{i2}]$ is the time window for the SKS wave, and $u_i^R(t)$ and $u_i^T(t)$ are the radial and

177   transverse-component records, respectively, from the *i*-th event. A dot above a variable indicates

178   derivative with respect to time. The conventional SKS splitting parameters at the given station,

179   namely the fast-direction azimuth θ and delay time Δt, are related to the SIs measured at the station

180   from all events through a sinusoidal curve fitting (Chevrot, 2000; Lin et al., 2014a):

$$S_i = \Delta t \sin 2(\theta - \theta_i^b), \tag{2}$$

182   where θ_i^b is the back azimuth of the *i*-th event.
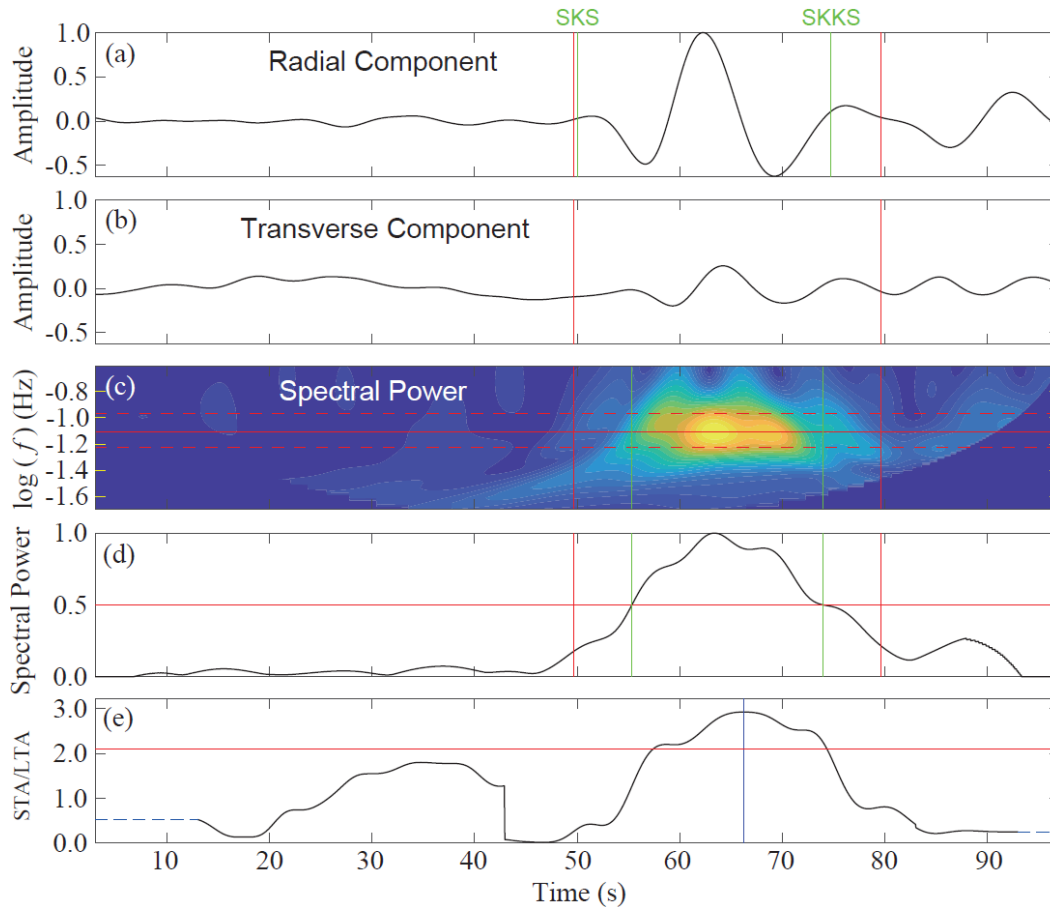
183   In this study, we obtain the SI measurements of SKS waves with the help of SplitRacer (Link

184   et al., 2022), an efficient and automatic toolbox developed for the measurement and quality control

185   of XKS splittings. An example of the SplitRacer processing is shown in Figure 4. We use SplitRacer

186   to determine the SKS time window automatically, followed by a manual check on the quality of the

187   SKS signals. Then, we calculate the SIs using Eq. (1). The period band we use in this study is 8–

188   50 s considering the dominant periods of the SKS signals as well as minimizing the interference

189   with neighboring phases. As shown in Figure 4, the spectral powers of the radial- and transverse-

190   component records are calculated by the short-time Fourier transform (Quatieri, 2006) and summed.

191   Then, the dominant frequency band of the SKS waveform can be identified (between the red dashed

192   horizontal lines in Figure 4c). At each time, the powers within the dominant frequency band are

193   summed (Figure 4d), which defines the SKS window by the two crossing points at 50% of the peak

194   level (vertical green lines in Figure 4d). The final SKS window is given by either expanding or

195   shrinking the 50% energy window to a fixed 30-s window (red vertical lines). After completing

196   the quality check using SplitRacer, we obtain a total of 12,457 SKS wave SI measurements.

197   Following Chevrot (2000), we estimate the uncertainty of each SI measurement using the

198   following equation

$$\sigma_i = \sqrt{\frac{1}{N_i} \left\{ \sum_{j=1}^{N_i} [u_i^T(t_j)]^2 - \frac{S_i^2}{4} \sum_{j=1}^{N_i} [\dot{u}_i^R(t_j)]^2 \right\}}, \tag{3}$$

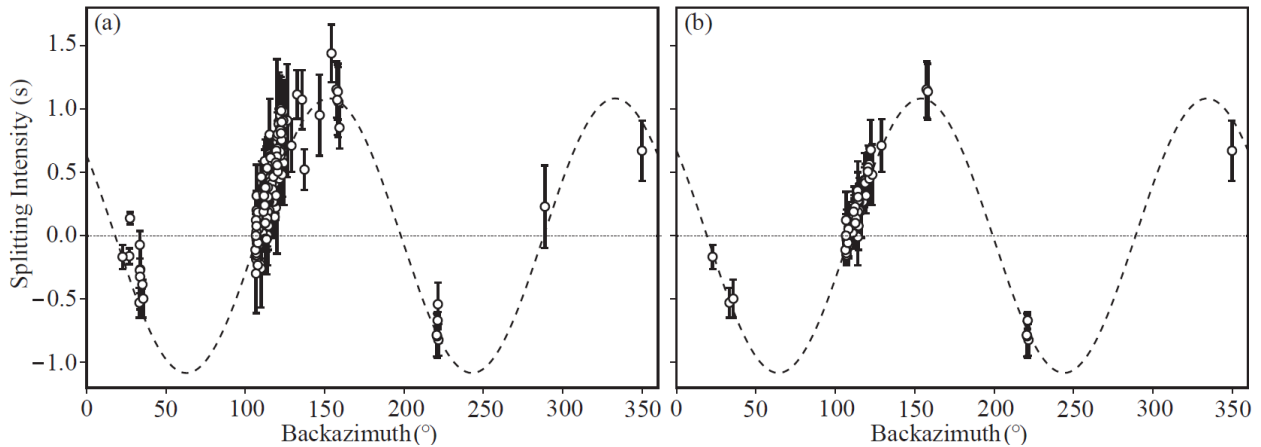where S_i is the i-th SI measurement, and N_i is the number of time samples used for the window to obtain the measurement.

Figure 4. Example of SKS window selection using SplitRacer. (a) and (b) show normalized radial and transverse records, respectively, around the SKS arrival at station WXT (blue triangle in Figure 1) from the 24 June 2019 earthquake in New Zealand with a back azimuth of 122°. The green lines mark the theoretical SKS and SKKS arrival times of seismic phases corresponding to the event of interest. Red vertical lines mark the start and end time of the final window containing the SKS waveform. (c) Summed spectral power of the spectrogram of the radial and transverse records in (a) and (b). The red horizontal line marks the frequency of maximum spectral power, and the red dashed lines show the frequency bounds of more than 80% of the maximum. The green vertical lines mark the time window in which the summed spectral power is more than 50% of the

212 maximum. (d) Summed spectral power over all frequencies. The green vertical lines mark the time

213 window in which the summed spectral energy is more than 50% of the maximum. (e) STA/LTA

214 ratio of the radial-component record used as quality check. The blue vertical line denotes the time

215 when the STA/LTA ratio reaches its peak within the window determined in (d). The red horizontal

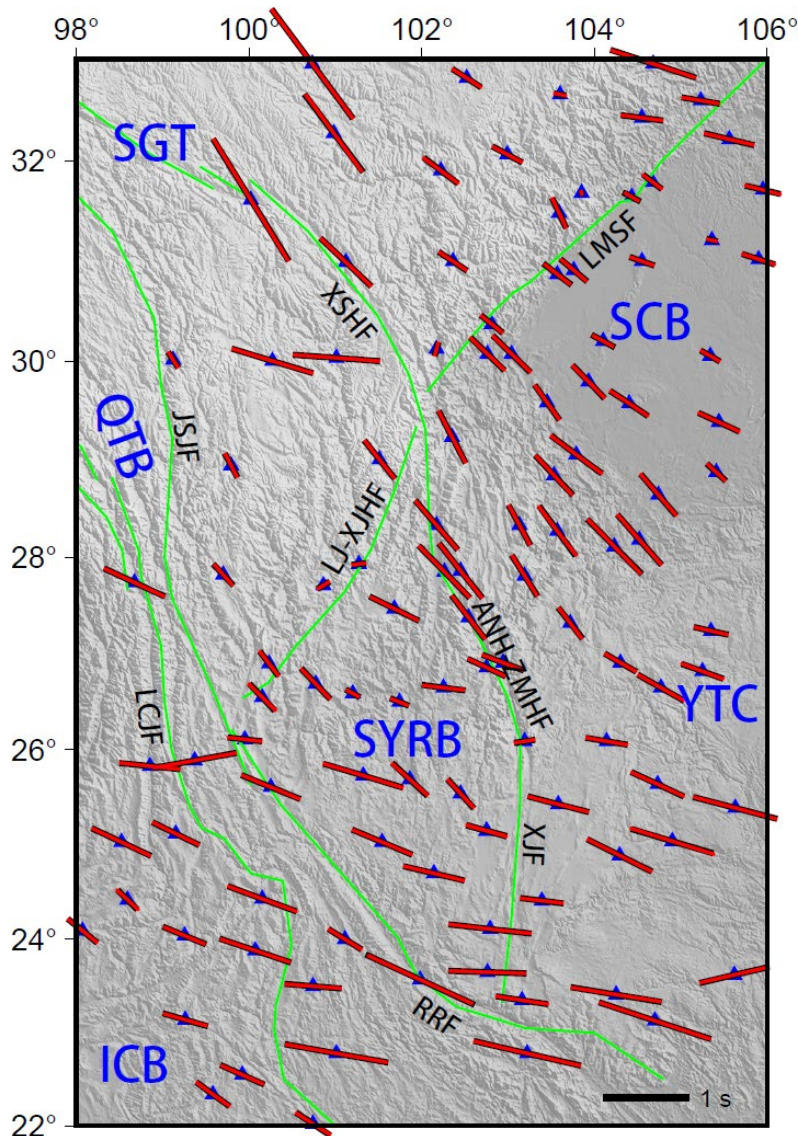216 line is the acceptance threshold of 2.1 (Link et al., 2022).

217 We further clean our dataset of outliers based on two criteria: (1) At a given station, SI

218 measurements with uncertainties σ_i larger than 1.5 times the average uncertainty $\bar{\sigma}$ for that station,

219 i.e. $\sigma_i > 1.5\bar{\sigma}$, are removed; (2) all SI measurements at a given station are fit by a sinusoidal curve,

220 and measurements that deviate from the sinusoidal curves by more than $2\sigma_i$ are also removed.

221 After removing the outliers, we retain a total of 5,216 high-quality SI measurements as our final

222 dataset for subsequent anisotropy inversion. The standard deviation of the final dataset (the

223 average of uncertainties of all retained data) is 0.074 s. Figure 5 shows the effect on the distribution

224 of SI measurements before and after applying the above two criteria for station WXT, which

225 reduces the number of SI data from 184 to 61.

226

Figure 5. Variations of measured SI with event back azimuth for station WXT (blue triangle in

Figure 1) before (a) and after (b) removal of SI outliers. The vertical error bars show two standard

deviations ($2\sigma_i$) of individual measurements. The dashed lines represent the sinusoidal curves that

best fit the measurements. According to Eq. (2), the conventional SKS splitting parameters for this

station are: $\Delta t = 1.08$ s and $\theta = 109.14°$.

232 Based on Eq. (2), we can obtain the conventional fast-direction azimuth θ and delay time Δt

233 at each station using all the SI measurements, and they are displayed in Figure 6. The spatial

234   distribution of θ has a similar pattern as seen in previous studies, i.e. a generally NW-SE oriented

235   fast axis and a nearly uniform EW alignment of the fast-axis directions south of ~26°N latitude.

236

237   **Figure 6**. Black line segments show the conventional SKS fast-direction azimuths and delay times

238   at all station obtained from the SI measurements according to Eq. (2). Red line segments are fast-

239   direction azimuths and delay times derived from Eq. (2) based on the model-predicted SIs obtained

240   by integrating the sensitivity kernels (see Figure 7) with the anisotropy model in Figure 12

241   according to Eq. (4). Names of major faults and tectonic blocks are the same as in Figure 1.

242   **2.3 Multiscale inversion for 3D anisotropic structure**

243   We implement the full-wave multiscale anisotropy tomography framework developed by Lin et al.
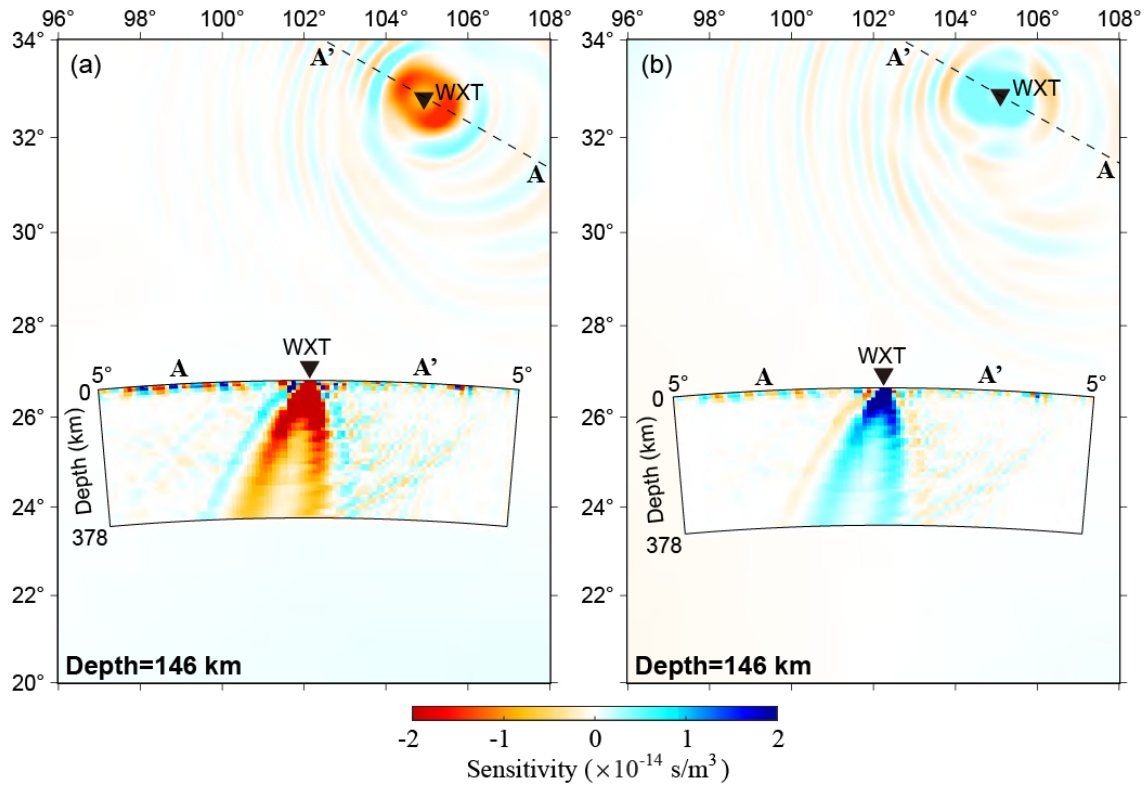
244   (2014b). Here we briefly describe our methodology. Interested readers may consult Lin et al.

245   (2014b) for a full description of the method.

246   Becker et al. (2006) point out that upper-mantle anisotropy is to first-order hexagonal and the

247   hexagonal parameters ε (describing P-wave anisotropy), γ (describing S-wave anisotropy) and δ

248   (an extra parameter describing the shape of P- and S-wave slowness surfaces) are strongly

249   correlated. Furthermore, Zhao & Chevrot (2011) demonstrated that the sensitivity of the SI of

250   an SKS wave is mostly sensitive to γ, and is about 10 times larger than that to the isotropic

251   heterogeneity. This allows us to considerably simplify the modeling of upper mantle anisotropy in

252   two aspects: (1) it is sufficient to use 1D reference model; and (2) the anisotropy can be described by

253   only two parameters: the strength of anisotropy γ and the azimuth ϕ_f of the symmetry axis of

254   anisotropy. We assume that the symmetry axis is horizontal since the sub-vertically propagating

255   SKS waves are insensitive to the dip angle of the symmetry axis of anisotropy (Mondal & Long,

256   2019). Note that the anisotropy strength γ and azimuth ϕ_f are spatially varying, and the

257   dependence of the SI on ϕ_f is nonlinear. As documented in Favier & Chevrot (2003), we can

258   introduce two independent parameters, $\gamma_c = \gamma \cos(2\phi_f)$ and $\gamma_s = \gamma \sin(2\phi_f)$ to enable a linear

259   relationship with the SI measurement

$$S = \iiint \left[K_{\gamma_c}^S(\boldsymbol{r})\gamma_c(\boldsymbol{r}) + K_{\gamma_s}^S(\boldsymbol{r})\gamma_s(\boldsymbol{r}) \right] d\boldsymbol{r}, \qquad (4)$$

261   where $K_{\gamma_c}^S$ and $K_{\gamma_s}^S$ are the Fréchet sensitivity kernels of the splitting intensity S to γ_c and γ_s,

262   respectively. After obtaining γ_c and γ_s from a linear inversion, we can obtain the more familiar

263   anisotropy parameters by utilizing the relations: $\phi_f(\boldsymbol{r}) = 0.5 \tan^{-1}[\gamma_s(\boldsymbol{r})/\gamma_c(\boldsymbol{r})]$ and $\gamma(\boldsymbol{r}) =$

264    $\sqrt{[\gamma_c(\boldsymbol{r})]^2 + [\gamma_s(\boldsymbol{r})]^2}$. In this study, we use PREM (Dziewonski & Anderson, 1981) as the

265   reference model and compute the sensitivity kernels using the normal mode summation algorithm

266   developed by Zhao & Chevrot (2011). Examples of the Fréchet kernels for γ_c and γ_s are shown in

267   Figure 7. Chevrot (2006) first noted the similarity between the definition of the SI in Eq. (1) and

268   that of the traveltime delay (e.g. Dahlen et al., 2000; Zhao et al., 2000), which implies that the sensitivity

269   kernels of the SI to anisotropy parameters exhibit the distinct banana-doughnut shapes typically seen in

270   the sensitivities of the finite-frequency traveltimes to isotropic velocities, as shown in Figure 7.

271

Figure 7. Examples of the sensitivity kernels of the SI to shear wave anisotropy parameters γ_c (a)

273   and γ_s (b) shown in mapviews for the 146-km depth and in profiles (insets) along source-receiver

274   path AA' for station WXT (blue triangle in Figure 1). The SKS wave is from the 24 June 2019

275   event in New Zealand with a back azimuth of 122º, and the waveforms are shown in Figure 4.

276   As in Lin et al. (2014b), we adopt a wavelet-based model parameterization (Chiao & Kuo,

277   2001) to obtain multi-scale resolutions in both sparsely- and densely-sampled regions of data

278   coverage. The inverse problem can be expressed as:

$$(\mathbf{GW^{-1}})(\mathbf{Wm}) = \mathbf{d}, \qquad (5)$$

280   where $\mathbf{G}$ is Gram matrix containing the Fréchet kernels, $\mathbf{W}$ is the 3D wavelet transformation matrix,
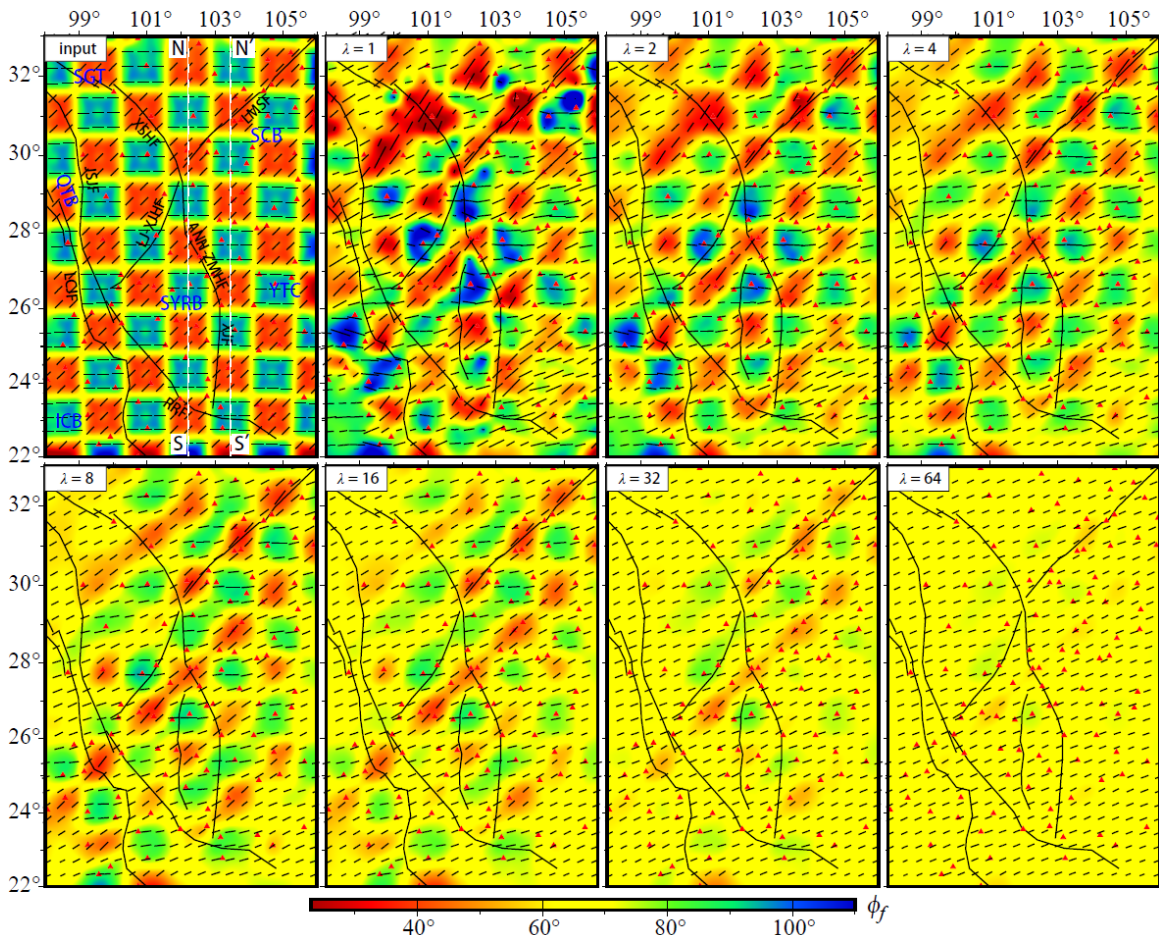
281 **m** is the vector comprising the model parameters at spatial nodes, and **d** is the data vector of the

282 SI measurements. In this study, we first parameterize the model by a 3D mesh with 33×33 nodes

283 horizontally and 17 nodes vertically, and apply the operator $(\mathbf{W}^{-1})^T$ on each row of **G**. A damped

284 least-squares solution to the inverse problem in Eq. (5) is solved by the LSQR algorithm (Paige &

285 Saunders, 1982), with the damping factor λ selected empirically by a series of inversion

286 experiments (see Section 2.4), and the final model can be obtained by an inverse wavelet transform.

287 Readers may refer to Hung et al. (2011) for implementation details of the multi-scale

288 parameterization. The wavelet approach achieves a finer spatial resolution in regions of better data

289 coverage and coarser resolution in less well-sampled regions, thus resolving the structure with an

290 objective and data-driven multi-scale resolution.

291 **2.4 Resolution tests**

292 Careful selection of the damping factor λ and objectively evaluating the resolution for a given

293 dataset in an inversion problem is paramount to interpreting the inversion results. Thus, it is important

294 to characterize how reliable our anisotropic models are, and to restrict our interpretations to robust

295 features that are well-resolved and required by the observations.

296   We present three sets of resolution tests to illustrate the selection of the optimal damping

297 factor and the resulting resolution of our SI dataset. Given the input model in a resolution test, the

298 SI is predicted for each SKS path in our final dataset by integrating the products of 3D sensitivity

299 kernels with the distributions of γ_c and γ_s in the input model according to Eq. (4). A Gaussian

300 noise with the same standard deviation as our final inversion dataset (0.074 s) is added to the SI

301 predictions. We first perform a series of tests using checkerboards of two different sizes (1º x 1º

302 and 1.5º x 1.5º) with horizontally alternating azimuthal angles of fast axes $\phi_f = 90°$ and $\phi_f = 45°$

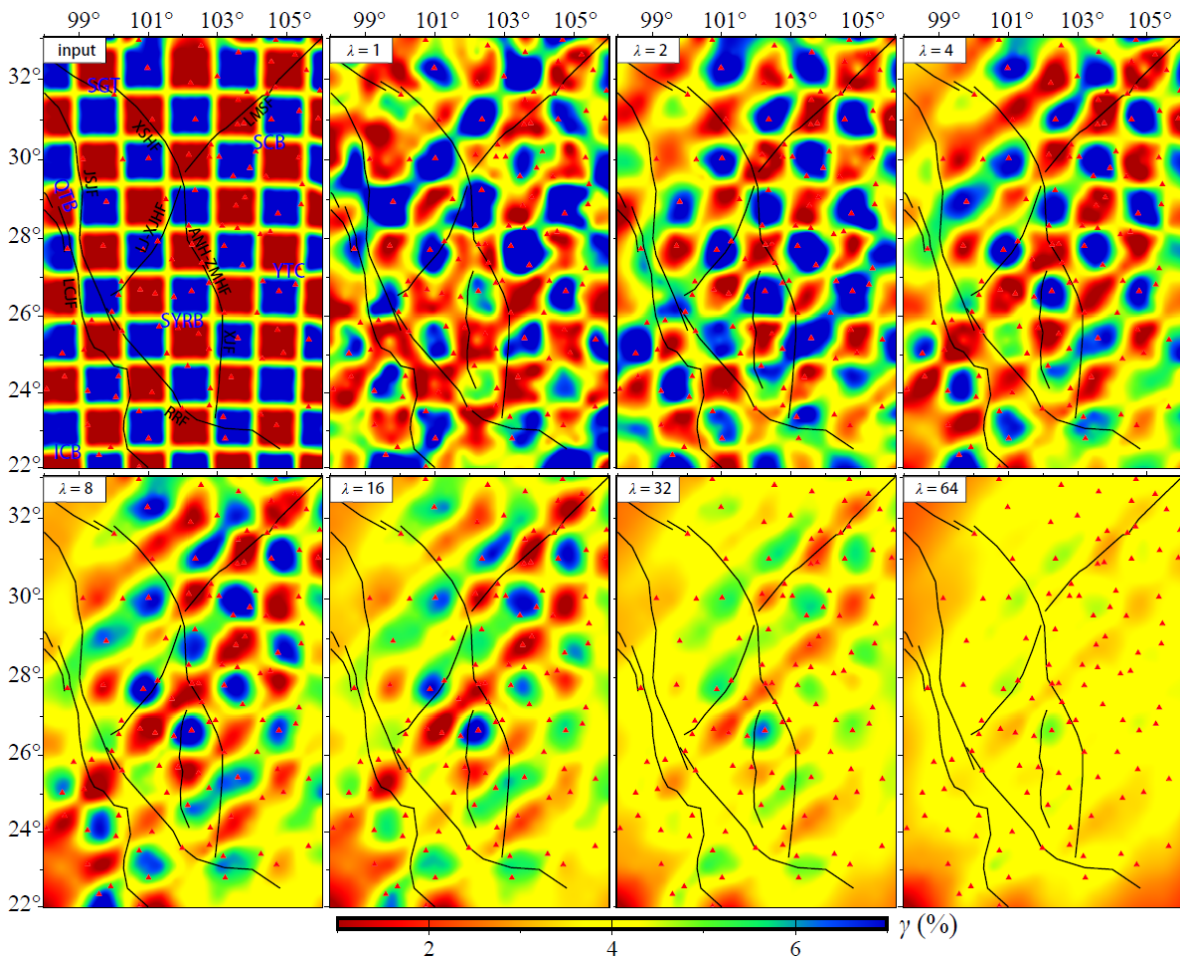303 but a fixed anisotropy strength $\gamma = 4\%$. Figure 8 shows the input and recovered models for

304   different values of the damping factor λ at a depth of 55 km for the 1° x 1° checkerboard test. The

305   effect of damping factor on the anisotropy pattern in the inversion result is obvious. The recovery

306   results suggest an optimal damping factor of $\lambda = 4$, and the checkerboard pattern is well-resolved

307   in most parts of the study area except in the northwest and southeast corners where stations are

308   more sparse. Results for recovered models at different depths as well as for 1.5° x 1.5°

309   checkerboards are presented in Figures S1 and S3 in Supporting Information.

Figure 8. Resolution tests for the azimuth of symmetry axis using 1° x 1° checkerboard. (Top-left)
The input model has horizontally alternating azimuthal angles of fast axes $\phi_f = 90°$ and $\phi_f = 45°$
shown by both the color and the directions of the line segments, and a fixed anisotropy strength
$\gamma = 4\%$ represented by the lengths of the line segments. The two white dashed lines show the
locations of profiles NS and N'S' in Figure 11. The other panels show the recovered models at a
depth of 55 km for different damping factors λ. We choose $\lambda = 4$ as the optimal value for the

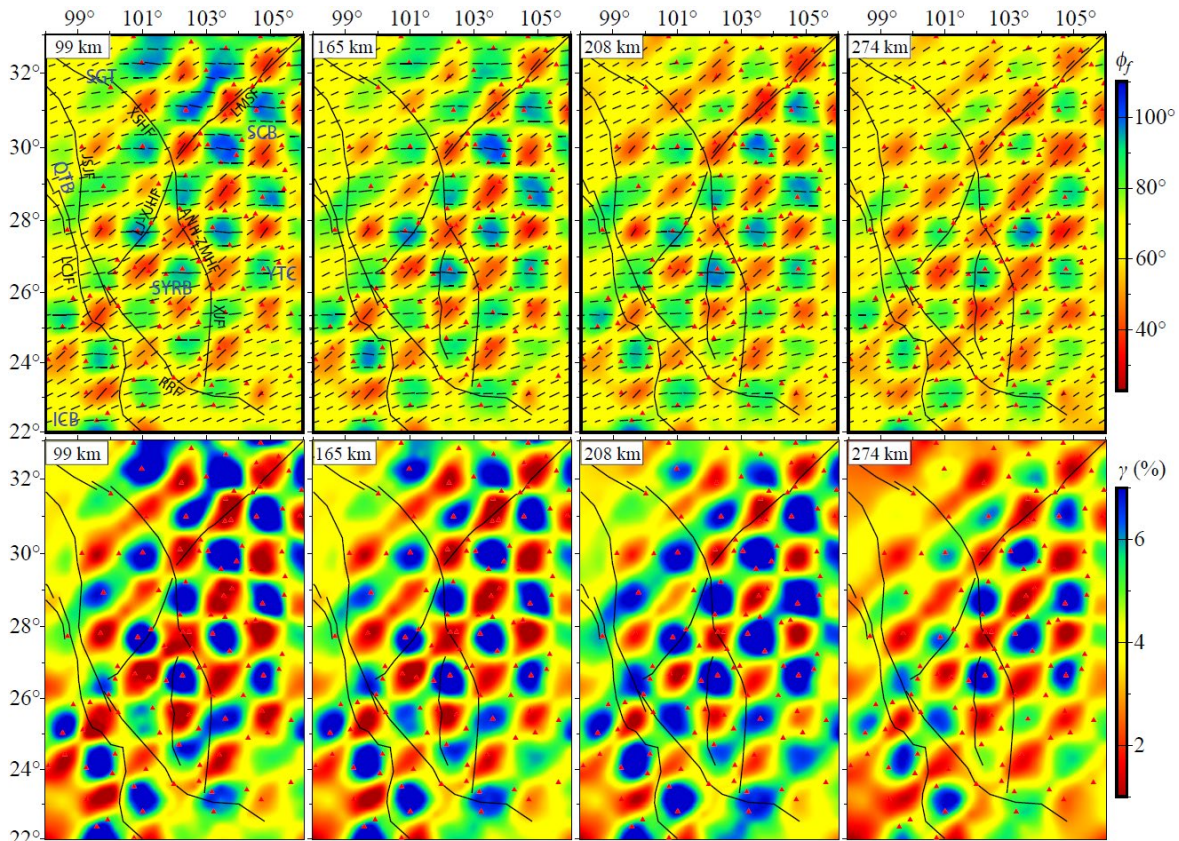317   damping factor (top-right panel). Red triangles show locations of stations used.

318   In the second set of tests, we use input checkerboard models with a fixed azimuthal angle of

319   symmetry axis $\phi_f = 22.5°$ but alternating perturbations of anisotropy strength of $\delta\gamma = \pm3\%$

320   relative to a background anisotropy strength of $\gamma = 4\%$. Figure 9 shows the recovery results at the

321   depth of 55 km using different damping factors for the 1° x 1° input checkerboard model. Results

322   for recovered models at different depths as well as for 1.5° x 1.5° checkerboards are presented in

323   Figures S2 and S4 in Supporting Information.

324

Figure 9. Resolution test using 1° x 1° checkerboard. (Top-left) The input model has horizontally

alternating anisotropy strengths shown by the colors representing perturbations of $\delta\gamma = \pm3\%$

relative to a background anisotropy strength of $\gamma = 4\%$ and a fixed azimuthal angle of symmetry

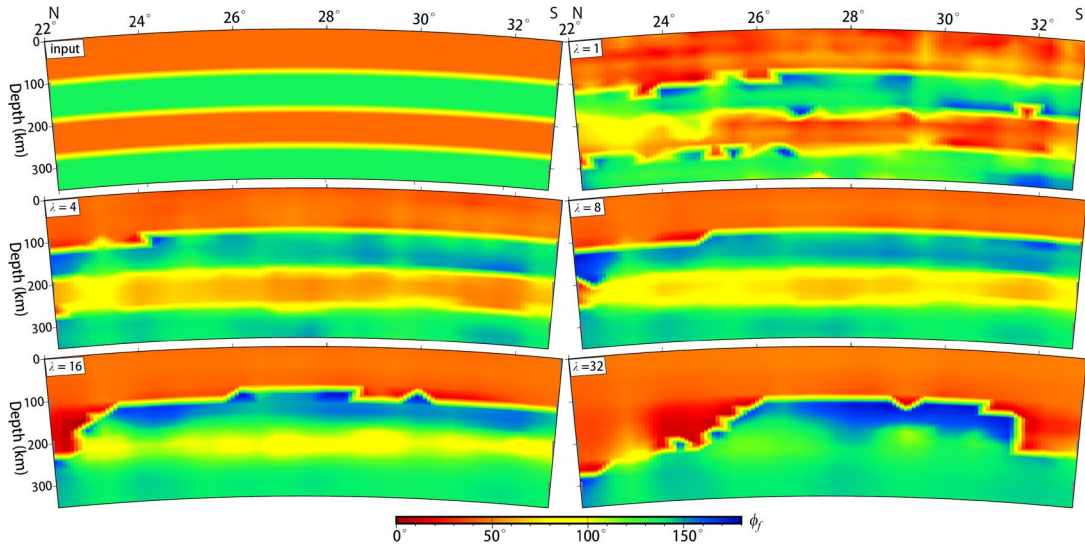axis $\phi_f = 22.5°$. The other panels show the recovered models at a depth of 55 km for different

329   damping factors λ. We choose $\lambda = 4$ as the optimal value for the damping factor (top-right panel).

330   Red triangles show locations of stations used.

331   The tests in Figures 8 and 9 both show that the damping factor of $\lambda = 4$ yields the best

332   resolved checkerboard pattern. For convenience, resolution test results at different depths for

333   damping factor $\lambda = 4$ are collected and displayed in Figure 10.

334

335   **Figure 10**. Resolution test using 1° x 1° checkerboard with damping factor $\lambda = 4$. (Upper panels)

336   Recovered model at the depths of 99 km, 165 km, 208 km and 274 km for an input model having

337   horizontally alternating azimuthal angles of fast axes $\phi_f = 90°$ and $\phi_f = 45°$ with a fixed

338   anisotropy strength $\gamma = 4\%$. The input model and the recovered model at 55-km depth are shown

339   in Figure 8. (Lower panels) Recovered model at the depths of 99 km, 165 km, 208 km and 274 km

340   for an input model with horizontally alternating anisotropy strengths of $\gamma = 1\%$ and $\gamma = 7\%$ with

341   a fixed azimuthal angle of symmetry axis $\phi_f = 22.5°$. The input model and the recovered model

342   at 55-km depth are shown in Figure 9. Red triangles show locations of stations used.

343   The third set of tests is intended to probe the depth resolution of our SI dataset with full-

344   waveform anisotropy tomography. We use input models with a fixed anisotropy strength of $\gamma =$

345   4% but several layers of alternating azimuthal angles of symmetry axes. Figure 11 shows the

346   recovery results for a 4-layer input model along a north-south vertical cross-section (cross-section

347   NS in the top-left panel of Figure 8) for different damping factors.

348

349   **Figure 11**. Resolution tests for an input model with 4 layers of alternating azimuthal angles of

350   symmetry axes $\phi_f = 45°$ and $\phi_f = 135°$ but a fixed anisotropy strength of $\gamma = 4\%$. Shown here

351   are the input model (top-left panel) and recovered models for different damping factors λ along

352   the north-south cross-section NS through the middle of the study region (see top-left panel in

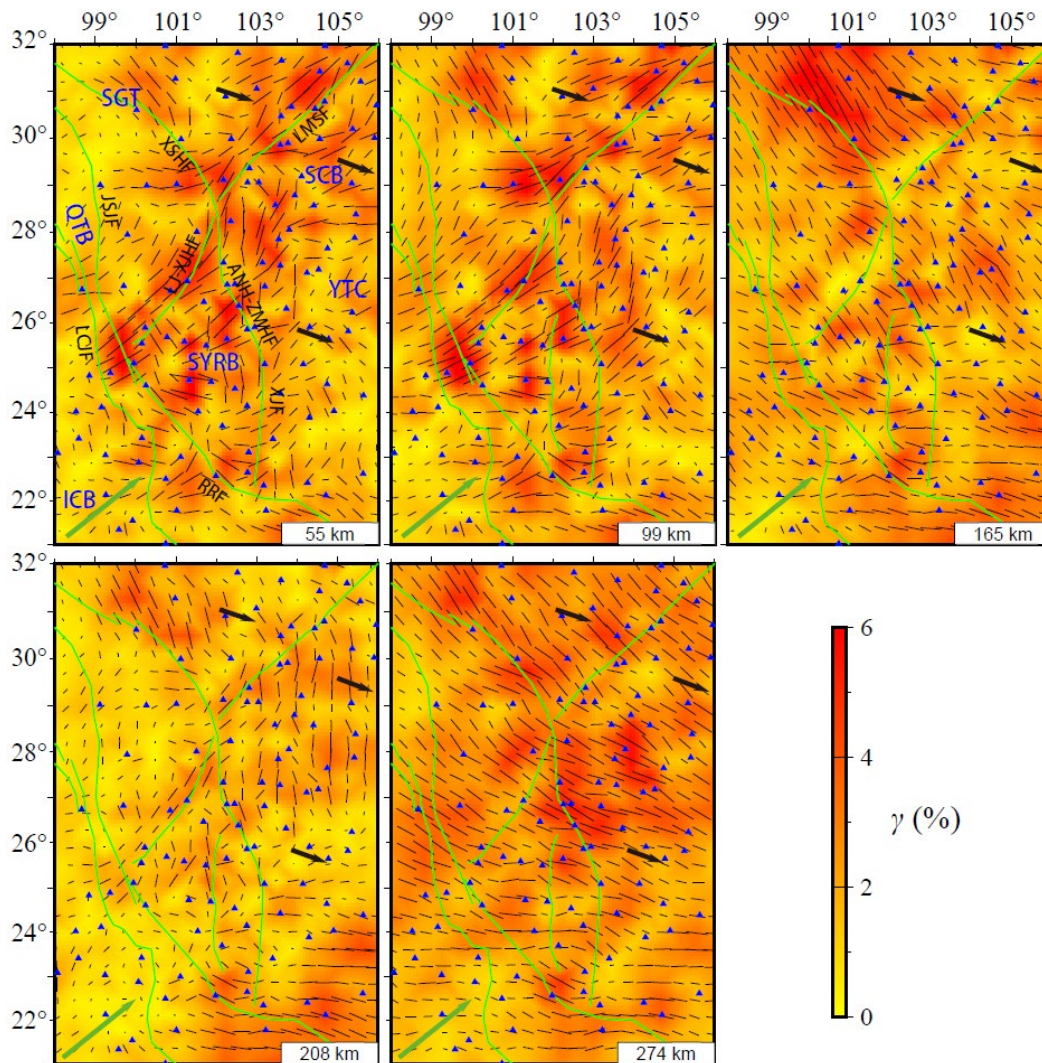353   Figure 8). The optimal damping is $\lambda = 4$ (middle-left panel).

354   Recovered models along another profile as well as for a 2-layer input model are presented in

355   Supporting Information (Figures S5-S8). These results also suggest an optimal damping factor of

356    $\lambda = 4$ in most parts of the study area. Based on all the resolution test results, we determine $\lambda = 4$

357   to be the optimal damping factor for the SI data inversions in this study.

358   The above resolution tests demonstrate that with the available distributions of seismic stations

359   and teleseismic earthquakes, our SKS wave SI dataset can resolve reasonably well the shear-wave

360   azimuthal anisotropy with a horizontal dimension of 1º x 1º and a vertical thickness of ~100 km in

361 the main part of the study region. Near the western border and in the SE corner, the resolution is

362 poor due to larger station spacing and fewer crossing SKS ray paths.

363 **3 Result**

364 As stated in Section 2.2, our final dataset contains 5,216 SI measurements at 111 permanent seismic

365 stations from 470 events, which are used to invert for the 3D azimuthal anisotropy structure of the

366 study region. Figure 12 displays our inverted model at five representative depths.

367

368 **Figure 12**. Three-dimensional anisotropic model for southeast margin of the Tibetan Plateau at 55

369 km, 99 km, 165 km, 208 km and 274 km depths. The anisotropy strength and the azimuth of the

370 fast axes are shown by the background color and the black line segments, respectively. The lengths

371 of the line segments are proportional to the anisotropy strength. The black and green arrows denote

372   the absolute plate motion (APM) of the Eurasian and Indian plates, respectively, according to the

373   model NNR-MORVEL56 (Argus et al., 2011). Names of major faults and tectonic blocks are the

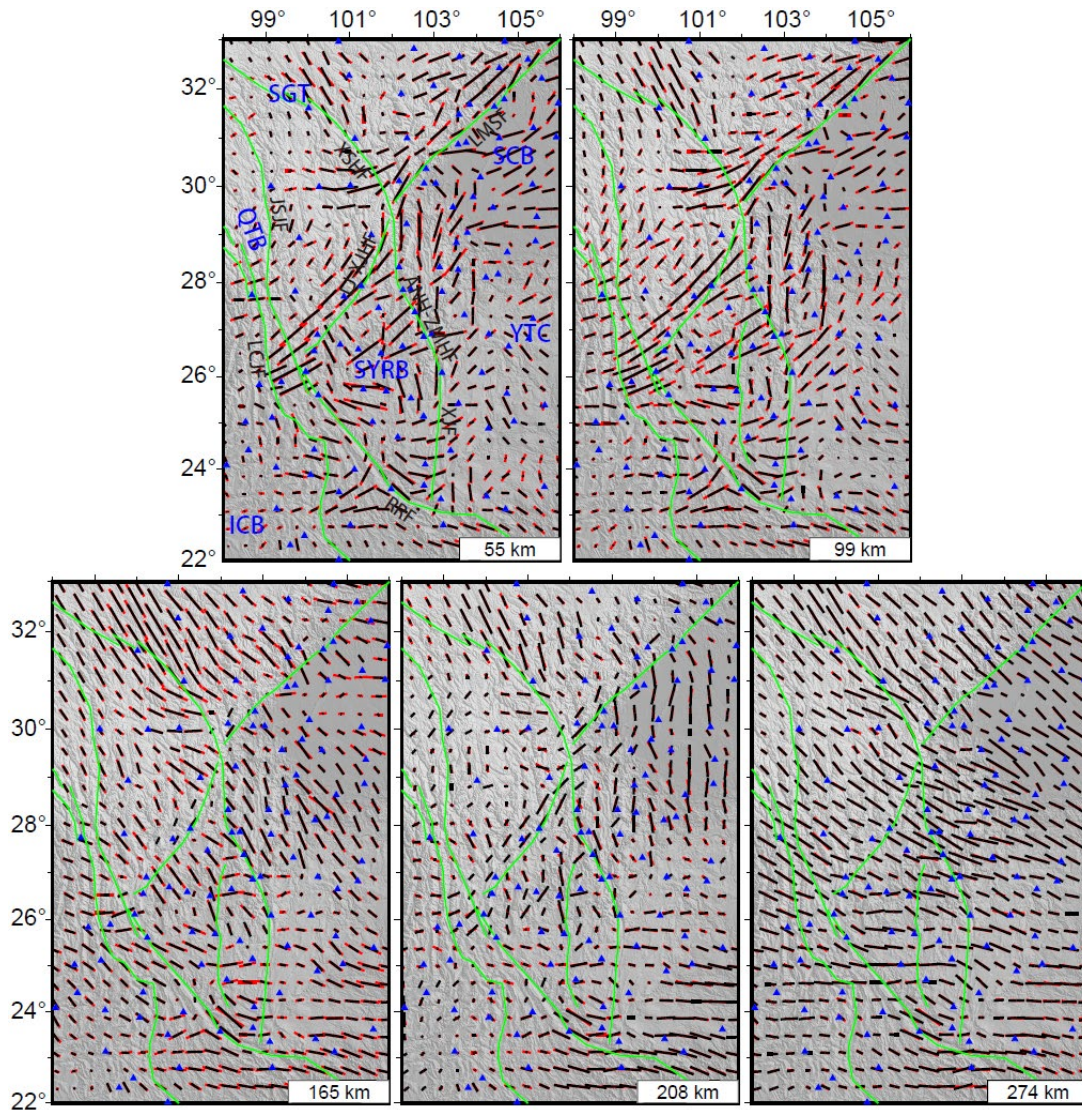374   same as in Figure 1. Blue triangles show locations of stations used.

375   As a first check of the inversion result, we calculate the model-predicted conventional SKS

376   splitting time Δt and fast-direction azimuth θ by integrating the anisotropy model (Figure 12) with

377   sensitivity kernels (Figure 7) according to Eq. (4) and compare with observations. The comparison

378   in Figure 6 shows excellent agreement between the model-predicted splitting parameters with

379   observations at all stations.

380   We also carry out a recovery test for our inversion result, in which we use the model in Figure

381   12 as the input model and calculate the synthetic SI data, then invert them using the same model

382   discretization and damping factor as in the inversion of the real data. The comparison in Figure 13

383   shows that the output model strongly resembles the input model at all depths. The synthetic inversion

384   successfully reproduces all the major features of the input model.

385   **4 Discussion**

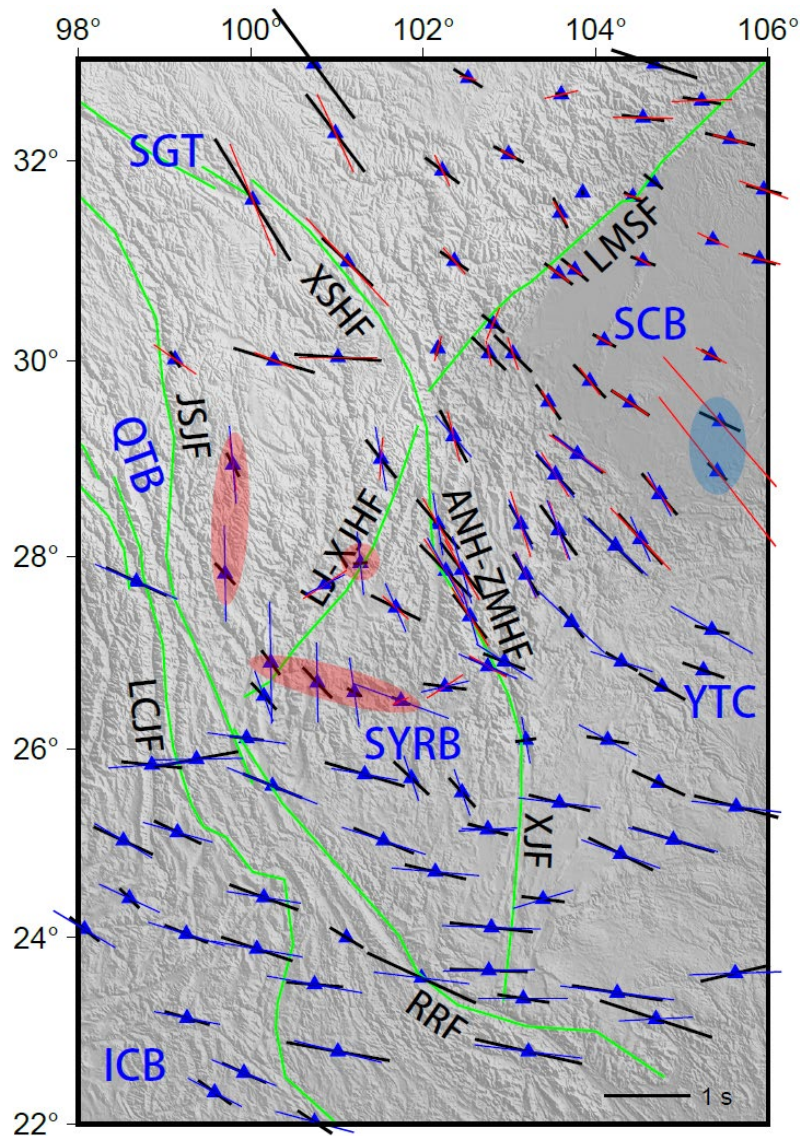386   **4.1 Comparison with previous results**

387   SKS splitting observation has been widely used to investigate the upper mantle anisotropy in the

388   southeastern margin of the Tibetan Plateau (e.g., Lev et al., 2006; Flesch et al., 2005; Wang et al., 2008;

389   Shi et al., 2012; Chang et al., 2015; Yang et al., 2018; Liu et al., 2020; Huang & Chevrot, 2021; Li et

390   al., 2021), with many overlapping seismic stations and teleseismic events. Here, we compare our

391   tomography result at common stations with those of Chang et al. (2015) and Liu et al. (2020) whose

392   SKS splitting measurements are available at the Shear Wave Splitting Product Query website

393   (http://ds.iris.edu/spud/swsmeasurement). In Figure 14, the SKS splitting parameters (splitting times

394   and fast-direction azimuths) predicted by our model in Figure 12 are compared with those from the

395   above two studies.

Figure 13. Result of the recovery test. The recovered and input anisotropic models are compared at five depths marked at the bottom-right corner in each panel. Black and red line segments denote the directions of fast axes in the input and recovery models, respectively, and their lengths indicates the anisotropy strength. Names of major faults and tectonic blocks are the same as in Figure 1. Blue triangles show locations of stations used.

Figure 14 shows that the fast axes determined from our tomographic results are in good agreement with previous studies at most stations. Major differences occur at two stations in the southern tip of the SCB (highlighted by the blue ellipse in Figure 14), where anomalously large splitting times can be seen in the results of Liu et al. (2020), shown by the red line segments. There are also discrepancies in both

406 delay time and fast-axis azimuth at a few stations (highlighted by the red ellipses in Figure 14) in the

407 SYRB where Chang et al. (2015) reported large splitting times and nearly NS fast axes, whereas our

408 model predicts moderate-to-small splitting times and more EW orientation of fast axes. Note that a

409 strictly quantitative comparison of different studies is difficult due to differences in earthquake and

410 window selections, data processing and frequency bands used in the measurement of SKS splitting

411 parameters.

412

413 **Figure 14**. Comparison of SKS splitting times and fast axis directions predicted by our anisotropy

414 model (Figure 12) with previous studies. Black line segments are results from the present study, whereas

415 blue and red line segments show results from Chang et al. (2015) and Liu et al. (2020), respectively.

416 Blue and red ellipses highlight stations where there are large discrepancies in splitting parameters

417 between this study and Liu et al. (2020) and Chang et al. (2015), respectively. Names of major faults

418 and tectonic blocks are the same as in Figure 1.

4.2 Overall variation of shear wave anisotropy

420 In the shear-wave anisotropy model displayed in Figure 12, we can see that the overall

421 anisotropy strength γ can reach 6% in the lithosphere and asthenosphere under the southeastern

422 margin of the Tibetan Plateau. Both the strength and fast-axis directions of anisotropy show strong

423 lateral and vertical variations. Within the lithosphere (depths of 55 km and 99 km), the anisotropy

424 is stronger in the transition zone between the Tibetan Plateau and YTC (along the LJ-XJHF and

425 LMSF) than other regions, whereas at greater depths in the asthenosphere (e.g. 274 km), the entire

426 region exhibits strong anisotropy with a largely NW-SE orientation of fast axis parallel to the

427 direction of the APM (black arrows in Figure 12), which turns to more E-W direction south of

428 26ºN. At intermediate depths (165 km and 208 km), the anisotropy is highly variable, both in terms

429 of strength and the direction of symmetry axis. Therefore, in the southeastern margin of the

430 Tibetan Plateau, our model shows an apparent decoupling in the overall deformations

431 between the lithosphere and asthenosphere, consistent with previous studies (e.g. Flesch

432 et al., 2005).

433 Previous studies have reported two major features in the SKS splitting pattern in the southeastern

434 margin of the Tibetan Plateau: an overall NW-SE direction of the fast axis and an alignment of the fast

435 axis in nearly EW direction south of ~26ºN latitude (e. g., Lev et al., 2006; Wang et al., 2008; Chang

436 et al., 2015; Huang & Chevrot, 2021), as shown in Figures 6 and 14. Our model suggests that this

437 relatively simple splitting pattern observed at the surface may be a manifestation of vertically averaged

438 complex variation of anisotropy over lithospheric and asthenospheric depths. For instance, along the

439   LMSF, the fast axes in the lithospheric depth (e.g. 55 km and 99 km) are mainly oriented NE-SW with

440   relatively high anisotropy strength, but change to NW-SE in the asthenosphere. As a result, we observe

441   relatively small SKS splitting times (< 0.5 s) with a fast-axis direction of NW-SE at the surface. On the

442   other hand, the moderate SKS splitting times (1 s or less) and the alignments of nearly EW orientation

443   of symmetry axes observed at the surface are resulted from a discordant anisotropy in the lithosphere

444   and a nearly uniform EW-oriented anisotropy in the asthenosphere.

445   **4.3 The Songpan-Ganzi Terrane**

446   The SGT is the central portion of the Tibetan Plateau and has been elevated by the collision

447   between the Indian and Eurasian plates. In its eastern part the eastward expansion of the terrane

448   has been blocked by the SCB of the YTC. In our study region, the SGT occupies an area of

449   inverted-triangle shape in the north bounded by the JSJF in the southwest and LMSF and LJ-XJHF

450   in the southeast (Li et al., 2021). Our model shows two distinct types of anisotropy. In the area far

451   away from the LMSF, the anisotropy is moderate to strong (3–6%) with NW-SE oriented fast axes

452   in both lithosphere and asthenosphere, parallel to the regional APM direction (black arrows in

453   Figure 12) and asthenospheric flow, suggesting a vertical coupling of deformation there and in

454   agreement with Flesch et al. (2005). The NW-SE orientation of anisotropy in the SGT is

455   consistent with previous tomography results from Rayleigh waves (Bao et al., 2020; Legendre et al.,

456   2015) and Pn waves (Lei et al., 2014). However, in the area near the LMSF, the fast axis of

457   anisotropy in the lithosphere (e.g. 55 km and 99 km depths) becomes NE-SW, parallel to the

458   proposed lithospheric material flow as a result of the resistance of the SCB to the eastward

459   expansion of the Tibetan Plateau at LMSF. Near the LMSF, the lithospheric material of the SGT

460   appears to come apart at ~102° longitude, going in the opposite NE and SW directions. In the

461   asthenosphere, the fast axis of anisotropy returns to NW-SE, consistent with the regional APM

462 direction. The relatively sharp turn of the fast axis of the lithospheric anisotropy from SE-NW to

463 NE-SW in the southern tip of SGT is a clear evidence for the redirection of the lithospheric flow

464 from eastward to southward in the southeastern margin of the Tibetan Plateau.

465 **4.4 The Yangtze Craton**

466 The YTC is a Precambrian continental block which was accreted to the North China Craton in the

467 Triassic. Our study region covers the western margin of the YTC, namely the SCB and SYRB, and

468 the model in Figure 12 shows that the anisotropy in the region varies significantly both horizontally

469 and vertically, as a result of the complex geodynamic evolution of the YTC involving multiple

470 rounds of lithospheric reactivation, such as the Permian-Triassic Emeishan flood basalt eruption

471 (e.g. Xu et al., 2001), as well as interactions with surrounding tectonic blocks. In our anisotropy

472 model, the SCB exhibits a moderate anisotropy with a NE-SW orientation near the LMSF at shallow

473 depths (e.g. 55 km and 99 km), presumably the effect of dominant shearing in the vicinity of the

474 LMSF by the moving SGT lithosphere in NE and SW directions. Further east, EW compression

475 gradually takes over NE-SW shear at shallow depths, and the fast axis of anisotropy turns to more

476 EW (e.g. 55 km, 99 km and 165 km). This turn of anisotropy from NE-SW to more EW away from

477 the LMSF has also been observed in surface-wave studies (e.g. Zhang et al., 2023). At greater

478 depth in the lithosphere (208 km in Figure 12), the anisotropy under the SCB becomes nearly NS,

479 which is consistent with a frozen anisotropy in the lithosphere generated by the mantle flow in the

480 Cenozoic (Li et al., 2021) without being modified by the SGT-SCB block interaction at shallower

481 depths. At asthenospheric depth (274 km), the anisotropy is largely aligned with the regional APM.

482   The anisotropy under the SYRB appears to be continuous across the ANH-ZMHF and XJF,

483 suggesting that both fault systems are crustal boundaries where the SYRB is escaping in the

484 southeast direction. In the lithosphere (55 km and 99 km under SYRB and above 208 km depth

485 east of ANH-ZMHF between the SCB and 26ºN), the anisotropy has a complex pattern of

486 relatively small-scale horizontal variations of fast-axis orientation, perhaps a result of multiple

487 phases of lithospheric reactivations that have modified the previously frozen anisotropy. In the

488 asthenosphere (> 100 km depth in SYRB and > 200 km between the SCB and 26ºN), the anisotropy

489 largely follows the direction of the regional APM or mantle flow. In the 208-km depth plot of the

490 model in Figure 12, the azimuthal anisotropy south of the SCB is very weak, which may indicate

491 a more complex local mantle flow pattern due to the regionally predominant NW-SE mantle flow

492 being disturbed by the root of the YTC lithosphere. South of 26ºN, the anisotropy under the YTC

493 is returns to largely parallel to the direction of APM.

494 **4.5 Anisotropy south of 26ºN latitude**

495 All SKS splitting studies in the southeastern margin of the Tibetan Plateau have shown the that the

496 SKS splitting south of 26ºN latitude appears to be consistently oriented in the EW direction. Our

497 model suggests that this apparently simple pattern is resulted predominantly from strong EW

498 oriented azimuthal anisotropy generated by the EW asthenosphere flow due to the eastward

499 subduction of the Indian Plate under Myanmar (e.g. Yang et al., 2022), and regional variation of

500 lithospheric and asthenospheric contributions to anisotropy leads small but discernable differences

501 in SKS splitting observations. For example, under the SYRB, the anisotropy in the lithosphere

502 between 24ºN and 26ºN is relatively strong (55 km and 99 km in Figure 12) with different

503 orientations of fast axes. The integration of lithospheric and asthenospheric anisotropy results in

504 horizontally variable SKS splitting delay times and fast-axis directions observed at the surface, as

505 shown by the stations in SYRB in Figures 6 and 14. In the rest of the study region south of 26ºN,

506 the asthenospheric contribution dominates, and the surface SKS splitting parameters exhibit

507 relatively uniform EW fast axes.

508 **5 Conclusions**

509 In this study, we have carried out a fullwave multiscale tomography to obtain the 3D model for

510 the shear-wave anisotropy in the southeastern margin of the Tibetan Plateau. A total of 5,216 high-

511 quality SKS splitting intensities are obtained from the broadband records of 470 teleseismic events

512 at 111 permanent stations after a series of quality control measures. In conjunction with the 3D

513 sensitivity kernels and a wavelet-based parameterization, this dataset is inverted to achieve a data-

514 driven multi-scale resolution to anisotropy structure in the upper mantle.

515 The vertical variation of the anisotropy in our result indicates that the lithospheric and

516 asthenospheric deformations are decoupled in the southeastern margin of the Tibetan Plateau. On

517 the other hand, the anisotropy appears to be vertically consistent under the Songpan-Ganzi Terrane,

518 suggesting a coupling of the deformations in the lithosphere and asthenosphere in the interior of

519 the Tibetan Plateau.

520 The strength of anisotropy in our model is spatially variable and can reach 6%, with strongest

521 anisotropy in the asthenosphere due to large-scale and relatively steady mantle flow, and in the

522 lithosphere along the Longmenshan Fault and Lijiang-Xiaojinhe Fault, presumably due to large

523 shearing effect generated by the relative movement between the Songpan-Ganzi Terrane and the

524 Yangtze Craton.

525 The azimuth of the fast axis of anisotropy in the asthenosphere largely follows the direction of

526 regional absolute plate motion or mantle flow, i.e. mostly SE beneath the Songpan-Ganzi Terrane and

527 the Yangtze Craton and nearly east-west south of 26ºN latitude. In the lithosphere, however, the fast

528 axis is highly variable. In the Sichuan Basin, the frozen anisotropy dominates in the deep lithosphere;

529 whereas at shallower depths, the anisotropy is modified by the interaction with the Songpan-Ganzi

530 Terrane into SW in the vicinity of the Longmenshan Fault and nearly EW further east. In the Sichuan-

531   Yunnan Rhombic Block and east of the Anninghe-Zemuhe Fault, the azimuth of the fast axis of

532   anisotropy exhibits complex spatial pattern due to multiple phases of lithospheric reactivation. The

533   vertical integration of the contributions from complex lithospheric anisotropy and relatively uniform

534   asthenospheric anisotropy gives rise to the seemingly simple pattern of conventional SKS splitting

535   parameters observed at the surface. Our 3D model of azimuthal anisotropy provides important new

536   insights into the lithospheric and asthenospheric dynamics in the southeastern margin of the

537   Tibetan Plateau.

538

539

544

545

Data Availability Statement

547   The processed SKS waveforms and their corresponding splitting intensities as well as the final

548   inverted anisotropic model can be accessed at https://doi.org/10.5281/zenodo.8232748. Most of

549   the figures are generated using the Generic Mapping Tools (Wessel et al., 2019,

550   https://www.generic-mapping-tools.org).

551

552

553

References

Argus, D. F., Gordon, R. G., & DeMets, C. (2011). Geologically current motion of 56 plates relative to the no-net-rotation reference frame. *Geochemistry, Geophysics, Geosystems*, *12*(11). doi: 10.1029/2011GC003751

Bao, X., Song, X., Eaton, D. W., Xu, Y., & Chen, H. (2020). Episodic lithospheric deformation in eastern Tibet inferred from seismic anisotropy. *Geophysical Research Letters*, 47(3). doi: 10.1029/2019gl085721

Becker, T. W., Chevrot, S., Schulte-Pelkum, V., & Blackman, D. K. (2006). Statistical properties of seismic anisotropy predicted by upper mantle geodynamic models. *Journal of Geophysical Research: Solid Earth*, 111(B8). doi: 10.1029/2005JB004095

Cai, Y., Wu, J., Fang, L., Wang, W., & Yi, S. (2016). Crustal anisotropy and deformation of the southeastern margin of the Tibetan Plateau revealed by Pms splitting. *Journal of Asian Earth Sciences*, 121, 120–126. doi: 10.1016/j.jseaes.2016.02.005

Chang, L.-J., Ding, Z.-F., & Wang, C.-Y. (2015). Upper mantle anisotropy beneath the southern segment of north-south tectonic belt, China. *Chinese Journal of Geophysics (in Chinese)*, 58(11), 4052–4067. doi: 10.6038/cjg20151114

Chevrot, S. (2000). Multichannel analysis of shear wave splitting. *Journal of Geophysical Research: Solid Earth*, 105(B9), 21579–21590. doi: 10.1029/2000JB900199

Chevrot, S. (2006). Finite-frequency vectorial tomography: a new method for high-resolution imaging of upper mantle anisotropy. *Geophysical Journal International*, 165(2), 641–657. doi: 10.1111/j.1365-246X.2006.02982.x

Chiao, L. Y., & Kuo, B. Y. (2001). Multiscale seismic tomography. *Geophysical Journal International*, 145(2), 517-527. doi: 10.1046/j.0956-540x.2001.01403.x

Dahlen, F., Hung, S.-H., & Nolet, G. (2000). Fréchet kernels for finite-frequency travel- times— I. Theory. *Geophysical Journal International*, 141(1), 157-174. doi: 10.1046/j.1365-246X.2000.00070.x

Dziewonski, A. M., & Anderson, D. L. (1981). Preliminary reference Earth model, *Physics of the Earth and Planetary Interior,* 25**,** 297–356.

Favier, N., & Chevrot, S. (2003). Sensitivity kernels for shear wave splitting in transverse isotropic media. *Geophysical Journal International*, 153(1), 213–228. doi: 10.1046/j.1365-246X.2003.01894.x

585 Flesch, L. M., Holt, W. E., Silver, P. G., Stephenson, M., Wang, C.-Y., & Chan, W. W. (2005).
586   Constraining the extent of crust–mantle coupling in central Asia using GPS, geologic, and
587   shear wave splitting data. *Earth and Planetary Science Letters*, 238(1-2), 248-268. doi:
588   10.1016/j.epsl.2005.06.023

589 Han, C., Xu, M., Huang, Z., Wang, L., Xu, M., Mi, N., Yu, D., Guo, T., Wang, H., Hao, S., Tia,
590   M., & Bi, Y. (2020). Layered crustal anisotropy and deformation in the SE Tibetan Plateau
591   revealed by Markov- Chain-Monte-Carlo inversion of receiver functions. *Physics of the Earth*
592   *and Planetary Interiors*, 306 , 106522. doi: 10.1016/j.pepi.2020.106522

593 Hu, J., Su, Y., Zhu, X., & Chen, Y. (2005). S-wave velocity and Poisson's ratio structure of crust
594   in Yunnan and its implication. *Science in China Series D: Earth Sciences*, 48(2), 210–218.
595   doi: 10.1360/03yd0062

596 Huang, J., Zhao, D., & Zheng, S. (2002). Lithospheric structure and its relationship to seismic and
597   volcanic activity in southwest China. *Journal of Geophysical Research: Solid Earth*,
598   107(B10), ESE–13. doi: 10.1029/2000JB000137

599 Huang, P., Gao, Y., & Xue, B. (2022). Advances in the deep tectonics and seismic anisotropy of
600   the Lijiang-Xiaojinhe fault zone in the Sichuan-Yunnan block, southwestern China.
601   *Earthquake Research Advances*, 2(1), 100116. doi: 10.1016/j.eqrea.2022.100116

602 Huang, R., Wang, Z., Pei, S., & Wang, Y. (2009). Crustal ductile flow and its contribution to
603   tectonic stress in Southwest China. *Tectonophysics*, 473(3-4), 476–489. doi: 10.1016/
604   j.tecto.2009.04.001

605 Huang, Z., & Chevrot, S. (2021). Mantle dynamics in the SE Tibetan Plateau revealed by
606   teleseismic shear-wave splitting analysis. *Physics of the Earth and Planetary Interiors*, 313,
607   106687. doi: 10.1016/j.pepi.2021.106687

608 Huang, Z., Wang, L., Xu, M., & Zhao, D. (2018). P wave anisotropic tomography of the SE
609   Tibetan Plateau: Evidence for the crustal and upper-mantle deformations. *Journal of*
610   *Geophysical Research: Solid Earth*, 123(10), 8957–8978. doi: 10.1029/2018JB016048

611 Huang, Z., Zhao, D., & Wang, L. (2015). P wave tomography and anisotropy beneath Southeast
612   Asia: Insight into mantle dynamics. *Journal of Geophysical Research: Solid Earth*, 120(7),
613   5154–5174. doi: 10.1002/2015JB012098

614 Hung, S. H., Chen, W. P., & Chiao, L. Y. (2011). A data-adaptive, multiscale approach of finite-
615   frequency, traveltime tomography with special reference to P and S wave data from central

616   Tibet. *Journal of Geophysical Research: Solid Earth*, 116. doi: 10.1029/2010JB008190

617 Kind, R., Yuan, X., Saul, J., Nelson, D., Sobolev, S., Mechie, J., Zhao, W., Kosarev, G., Ni, J.,

618   Achauer, U., & Jiang, M. (2002). Seismic images of crust and upper mantle beneath Tibet:

619   Evidence for Eurasian plate subduction. *Science*, 298(5596), 1219–1221. doi:

620   10.1126/science.1078115

621 Legendre, C. P., Deschamps, F., Zhao, L., & Chen, Q.-F. (2015). Rayleigh-wave dispersion reveals

622   crust-mantle decoupling beneath eastern Tibet. *Scientific Reports*, 5(1), 1–7. doi:

623   10.1038/srep16644

624 Lei, J., Li, Y., Xie, F., Teng, J., Zhang, G., Sun, C., & Zha, X. (2014). Pn anisotropic tomography

625   and dynamics under eastern Tibetan Plateau. *Journal of Geophysical Research: Solid Earth*,

626   119(3), 2174–2198. doi: 10.1002/2013JB010847

627 Lev, E., Long, M. D., & van der Hilst, R. D. (2006). Seismic anisotropy in Eastern Tibet from

628   shear wave splitting reveals changes in lithospheric deformation. *Earth and Planetary*

629   *Science Letters*, 251(3-4), 293-304. doi: 10.1016/j.epsl.2006.09.018

630 Li, H., Su, W., Wang, C.-Y., & Huang, Z. (2009). Ambient noise Rayleigh wave tomography in

631   western Sichuan and eastern Tibet. *Earth and Planetary Science Letters*, 282(1-4), 201–211.

632   doi: 10.1016/j.epsl.2009.03.021

633 Li, W., Chen, Y., Liang, X., & Xu, Y.-G. (2021). Lateral seismic anisotropy variations record

634   interaction between Tibetan mantle flow and plume-strengthened Yangtze Craton. *Journal of*

635   *Geophysical Research: Solid Earth*, 126, e2020JB020841.

636   https://doi.org/10.1029/2020JB020841

637 Lin, Y.-P., Zhao, L., & Hung, S.-H. (2014a). Full-wave effects on shear wave splitting,

638   *Geophysical Research Letters*, 41(3), 799–804. doi: 10.1002/2013GL058742

639 Lin, Y.-P., Zhao, L., & Hung, S.-H. (2014b). Full-wave multiscale anisotropy tomography in

640   Southern California. *Geophysical Research Letters*, 41(24), 8809–8817. doi: 10.1002/

641   2014GL061855

642 Link, F., Reiss, M. C., & Rümpker, G. (2022). An automatized XKS-splitting procedure for large

643   data sets: Extension package for SplitRacer and application to the USArray. *Computers &*

644   *Geosciences*, 158, 104961. doi: 10.1016/j.cageo.2021.104961

645 Liu, J., Wu, J., Wang, W., Fang, L., & Chang, K. (2020). Seismic anisotropy beneath the eastern

646   margin of the Tibetan Plateau from SKS splitting observations. *Tectonophysics*, 785, 228430.

647   doi: 10.1016/j.tecto.2020.228430

648 Liu, Q. Y., van Der Hilst, R. D., Li, Y., Yao, H. J., Chen, J. H., Guo, B., Qi, S. H., Wang, J., Huang,

649   H., & Li, S. C. (2014). Eastward expansion of the Tibetan Plateau by crustal flow and strain

650   partitioning across faults. *Nature Geoscience*, 7(5), 361–365. doi: 10.1038/NGEO2130

651 Long, M. D., & Becker, T. W. (2010). Mantle dynamics and seismic anisotropy. *Earth and*

652   *Planetary Science Letters,* 297(3-4), 341–354.

653 Mondal, P., & Long, M. D. (2019). A model space search approach to finite-frequency SKS

654   splitting intensity tomography in a reduced parameter space. *Geophysical Journal*

655   *International*, 217, 238-256. doi: 10.1093/gji/ggz016

656 Mondal, P., & Long, M. D. (2020). Strong seismic anisotropy in the deep upper mantle beneath

657   the Cascadia backarc: Constraints from probabilistic finite-frequency SKS splitting intensity

658   tomography. *Earth and Planetary Science Letters*, 539, 116172. doi:

659   10.1016/j.epsl.2020.116172

660 Monteiller, V., & Chevrot, S. (2011). High-resolution imaging of the deep anisotropic structure of

661   the San Andreas Fault system beneath southern California. *Geophysical Journal*

662   *International*, 186(2), 418-446. doi: 10.1111/j.1365-246X.2011.05082.x

663 Paige, C. C., & Saunders, M. A. (1982). LSQR–an algorithm for sparse linear-equations and sparse

664   least-squares. *ACM Transactions on Mathematical Software*, 8(1), 43–71.

665 Pasyanos, M. E., Masters, T. G., Laske, G., & Ma, Z. (2014). LITHO1. 0: An updated crust and

666   lithospheric model of the Earth. *Journal of Geophysical Research: Solid Earth*, 119(3), 2153–

667   2173. doi: 10.1002/2013JB010626

668 Quatieri, T. F. (2006). *Discrete-time Speech Signal Processing: Principles and Practice*. Pearson

669   Education India.

670 Royden, L. H., Burchfiel, B. C., & van der Hilst, R. D. (2008). The geological evolution of the

671   Tibetan Plateau. *Science*, 321(5892), 1054–1058. doi: 10.1126/science.1155371

672 Shen, Z.-K., Lü, J., Wang, M., & Bürgmann, R. (2005). Contemporary crustal deformation around

673   the southeast borderland of the Tibetan Plateau. *Journal of Geophysical Research: Solid*

674   *Earth*, 110(B11). doi: 10.1029/2004JB003421

675 Shi, Y., Gao, Y., Su, Y., & Wang, Q. (2012). Shear-wave splitting beneath Yunnan area of

676   Southwest China. *Earthquake Science*, 25(1), 25–34. doi: 10.1007/s11589-012-0828-4

677 Sieminski, A., Paulssen, H., Trampert, J., & Tromp, J. (2008). Finite-frequency SKS splitting:

measurement and sensitivity kernels. *Bulletin of the Seismological Society of America*, 98(4), 1797–1810. doi: 10.1785/0120070297

Sun, Y., Niu, F., Liu, H., Chen, Y., & Liu, J. (2012). Crustal structure and deformation of the SE Tibetan plateau revealed by receiver function data. *Earth and Planetary Science Letters*, 349, 186-197. doi: 10.1016/j.epsl.2012.07.007

Wang, C.-Y., Chan, W. W., & Mooney, W. D. (2003). Three-dimensional velocity structure of crust and upper mantle in southwestern China and its tectonic implications. *Journal of Geophysical Research: Solid Earth*, *108*(B9). doi: 10.1029/2002JB001973

Wang, C.-Y., Flesch, L. M., Silver, P. G., Chang, L.-J., & Chan, W. W. (2008). Evidence for mechanically coupled lithosphere in central Asia and resulting implications. *Geology*, 36(5), 363–366. doi: 10.1130/G24450A.1

Wang, C.-Y., Lou, H., Silver, P. G., Zhu, L., & Chang, L. (2010). Crustal structure variation along 30°N in the eastern Tibetan Plateau and its tectonic implications. *Earth and Planetary Science Letters*, 289(3-4), 367–376. doi: 10.1016/j.epsl.2009.11.026

Wang, M., & Shen, Z.-K. (2020). Present-day crustal deformation of continental China derived from GPS and its tectonic implications. *Journal of Geophysical Research: Solid Earth*, 125(2), e2019JB018774. doi: 10.1029/2019JB018774

Wang, W., Wu, J., Fang, L., Lai, G., & Cai, Y. (2017). Crustal thickness and Poisson's ratio in southwest China based on data from dense seismic arrays. *Journal of Geophysical Research: Solid Earth*, 122(9), 7219–7235. doi: 10.1002/2017JB013978

Wei, W., Xu, J., Zhao, D., & Shi, Y. (2012). East Asia mantle tomography: New insight into plate subduction and intraplate volcanism. *Journal of Asian Earth Sciences*, 60, 88–103. doi: 10.1016/j.jseaes.2012.08.001

Wei, Z., & Zhao, L. (2019). Lg-Q model and its implication on high-frequency ground motion for earthquakes in the Sichuan and Yunnan region. *Earth and Planetary Physics*, 3(6), 526–536. doi: 10.26464/epp2019054

Wei, Z., & Zhao, L. (2022). P-wave velocity structure of the lower crust and uppermost mantle beneath the Sichuan-Yunnan (China) region. *Seismological Research Letters*, 93(4). doi: 10.1785/0220210357

Wessel, P., Luis, J., Uieda, L., Scharroo, R., Wobbe, F., Smith, W. H., & Tian, D. (2019). The generic mapping tools version 6. *Geochemistry, Geophysics, Geosystems*, 20(11), 5556–5564.

709   doi: 10.1029/2019GC008515

710 Xu, L., Rondenay, S., & van der Hilst, R. D. (2007). Structure of the crust beneath the southeastern

711   Tibetan Plateau from teleseismic receiver functions. *Physics of the Earth and Planetary*

712   *Interiors*, 165(3-4), 176–193. doi: 10.1016/j.pepi.2007.09.002

713 Xu, M., Huang, Z., Wang, L., Xu, M., Zhang, Y., Mi, N., Yu, D., & Yuan, X. (2020). Sharp lateral

714   Moho variations across the SE Tibetan margin and their implications for plateau growth.

715   *Journal of Geophysical Research: Solid Earth*, 125(5), e2019JB018117. doi:

716   10.1029/2019JB018117

717 Xu, Y., Chung, S.-L., Jahn, B.-m., & Wu, G. (2001). Petrologic and geochemical constraints on

718   the petrogenesis of Permian–Triassic Emeishan flood basalts in southwestern China. *Lithos*,

719   58, 145–168.

720 Yang, S., Liang, X., Jiang, M., Chen, L., He, Y., Mon, C. T., Hou, G., Thant, M., Sein, K., & Wan,

721   B. (2022). Slab remnants beneath the Myanmar terrane evidencing double subduction of the

722   Neo-Tethyan Ocean. *Science Advances*, 8(34), eabo1027. doi: 10.1126/sciadv.abo1027

723 Yang, Y., Liang, C., Fang, L., Su, J., & Hua, Q. (2018). A comprehensive analysis on the stress

724   field and seismic anisotropy in eastern Tibet. *Tectonics*, 37(6), 1648–1657. doi:

725   10.1029/2018TC005011

726 Yang, Y., Yao, H., Wu, H., Zhang, P., & Wang, M. (2019). A new crustal shear-velocity model in

727   Southwest China from joint seismological inversion and its implications for regional crustal

728   dynamics. *Geophysical Journal International*, 220, 1379–1393.

729   https://doi.org/10.1093/gji/ggz514

730 Yang, Y., Zheng, Y., Chen, J., Zhou, S., Celyan, S., Sandvol, E., Tilmann, F., Priestley, K., Hearn,

731   T. M., Ni, J. F., Brown, L. D., & Ritzwoller, M. H. (2010). Rayleigh wave phase velocity

732   maps of Tibet and the surrounding regions from ambient seismic noise tomography.

733   *Geochemistry, Geophysics, Geosystems*, 11(8). doi:10.1029/2010GC003119

734 Yao, H. J., van der Hilst, R. D., & Montagner, J. P. (2010). Heterogeneity and anisotropy of the

735   lithosphere of SE Tibet from surface wave array tomography. *Journal of Geophysical*

736   *Research: Solid Earth*, 115. doi: 10.1029/2009JB007142

737 Yin, A., & Harrison, T. M. (2000). Geologic evolution of the Himalayan-Tibetan orogen. *Annual*

738   *Review of Earth and Planetary Sciences*, 28(1), 211–280.

739 Zhang, F., Wu, Q., Li, Y., Zhang, R., Sun, L., Pan, J., & Ding, Z. (2018). Seismic tomography of

eastern Tibet: Implications for the Tibetan Plateau growth. *Tectonics*, 37(9), 2833–2847. doi: 10.1029/2018TC004977

Zhang, G. W., Guo, A. L., Wang, Y. J., Li, S. Z., Dong, Y. P., Liu, S. F., He, D. F., Cheng, S. Y., Lu, R. K., & Yao, A. P. (2013). Tectonics of South China Continent and its implications. *Science China Earth Sciences*, 56, 1804–1828. doi: 10.1007/s11430-013-4679-1

Zhang, P., Deng, Q., Zhang, G., Ma, J., Gan, W., Min, W., Mao, F., & Wang, Q. (2003). Active tectonic blocks and strong earthquakes in the continent of China. *Science China Earth Sciences*, 46(2), 13–24. doi: 10.1360/03dz0002

Zhang, P.-Z. (2013). A review on active tectonics and deep crustal processes of the western Sichuan region, eastern margin of the Tibetan Plateau. *Tectonophysics*, 584, 7–22. doi: 10.1016/j.tecto.2012.02.021

Zhang, Z., Wang, Y., Chen, Y., Houseman, G. A., Tian, X., Wang, E., & Teng, J. (2009). Crustal structure across Longmenshan fault belt from passive source seismic profiling. *Geophysical Research Letters*, 36(17). doi: 10.1029/2009GL039580

Zhang, Z., Yao, H., & Yang, Y. (2020). Shear wave velocity structure of the crust and upper mantle in Southeastern Tibet and its geodynamic implications. *Science China Earth Sciences*, 63, 1278–1293. https://doi.org/10.1007/s11430-020-9625-3

Zhang, Z., Feng, J., & Yao, H. (2023). 3-D azimuthal anisotropy structure reveals different deformation modes of the crust and upper mantle in the southeastern Tibetan Plateau. *Frontiers in Earth Science*, 11, 1095609. doi: 10.3389/feart.2023.1095609

Zhao, G., Unsworth, M. J., Zhan, Y., Wang, L., Chen, X., Jones, A. G., Tang, J., Xiao, Q., Wang, J., Cai, J., Li, T., Wang, Y., & Zhang, J. (2012). Crustal structure and rheology of the Longmenshan and Wenchuan Mw 7.9 earthquake epicentral area from magnetotelluric data. *Geology*, 40(12), 1139–1142. doi: 10.1130/ G33703.1

Zhao, L., & Chevrot, S. (2011). An efficient and flexible approach to the calculation of three-dimensional full-wave fréchet kernels for seismic tomography—II. Numerical results. *Geophysical Journal International*, 185(2), 939–954. doi: 10.1111/j.1365-246X.2011.04984.x

Zhao, L., Jordan, T. H., & Chapman, C. H. (2000). Three-dimensional Fréchet differential kernels for seismic delay times, *Geophysical Journal International*, 141(3), 558–576. doi: 10.1046/j.1365-246x.2000.00085.x

771   Zhao, L. F., Xie, X. B., He, J. K., Tian, X., & Yao, Z. X. (2013). Crustal flow pattern beneath the

772   Tibetan Plateau constrained by regional Lg-wave Q tomography. *Earth and Planetary*

773   *Science Letters*, 383, 113–122. doi: 10.1016/j.epsl.2013.09.038.

1   **Upper-mantle anisotropy in the southeastern margin of the Tibetan Plateau revealed by fullwave**

2   **SKS splitting intensity tomography**

3   Yi Lin[1,2], Li Zhao[1,3]

4   [1] School of Earth and Space Sciences, Peking University, Beijing 100871, China.

5   [2] Key Laboratory of Earth Exploration and Information Techniques of the China Ministry of

6   Education, Chengdu University of Technology, Chengdu 610059, China.

7   [3] Hebei Hongshan National Geophysical Observatory, Peking University, Beijing 100871, China.

8

9

10   Corresponding author: L. Zhao (lizhaopku@pku.edu.cn)

11

12

13   **Key Points:**

14   • A 3D shear-wave anisotropy model for the SE margin of the Tibetan Plateau is obtained

15   by fullwave SKS splitting intensity tomography

16   • Anisotropy distribution shows a decoupling of the deformations in the lithosphere and

17   asthenosphere

18   • Lithospheric anisotropy has a complex pattern, whereas asthenospheric anisotropy

19   follows the APM

20

21 **Abstract**

22 The southeastern margin of the Tibetan Plateau has experienced complex deformation since the

23 Cenozoic, resulting in a high level of seismicity and seismic hazard. Knowledge about the seismic

24 anisotropy provides important insight into the deformation mechanism and the regional

25 seismotectonics beneath this tectonically active region. In this study, we conduct a fullwave multi-

26 scale tomography to investigate the seismic anisotropy in the southeastern margin of the Tibetan

27 Plateau. Broadband records from 470 teleseismic events at 111 permanent stations in the region are

28 used to obtain 5,216 high-quality SKS splitting intensity measurements, which are then inverted in

29 conjunction with 3D sensitivity kernels to obtain the anisotropic model for the region with a multi-

30 scale resolution. Resolution tests show that our dataset recovers anisotropy anomalies reasonably well

31 on the scale of 1º x 1º horizontally and ~100 km vertically. Our result suggests that in the southeastern

32 margin of the Tibetan Plateau the deformations in the lithosphere and asthenosphere are decoupled. The

33 anisotropy in the lithosphere varies both laterally and vertically as a result of the dynamic interactions

34 of neighboring blocks as well as lithospheric reactivation. The anisotropy in the asthenosphere largely

35 follows the direction of regional absolute plate motion, i.e. southeastward under the Songpan-Ganzi

36 Terrane and the Yangtze Craton and nearly east-west south of 26ºN latitude. The SKS splitting

37 observed at the surface can be interpreted as the vertical integration of the contributions from

38 lithosphere and asthenosphere.

39 **Keywords:** seismic anisotropy; splitting intensity; finite-frequency; fullwave tomography;

40 southeastern Tibetan Plateau

41

42 **Plain Language Summary**

43 The southeastern margin of the Tibetan Plateau has experienced significant deformation since the

44   Cenozoic due to the collision with the Indian Plate in the south and interactions with the Yangtze

45   Craton in the east. Knowledge about the upper mantle seismic anisotropy helps us understand the

46   reginoal deformation and dynamic evolution. In this study, we conduct a fullwave multi-scale

47   anisotropy tomography for the southeastern margin of the Tibetan Plateau using 5,216 high-quality

48   SKS splitting intensity measurements obtained from the broadband records of 470 teleseismic events

49   at 111 stations. Our result shows a decoupling between the lithosphere and asthenosphere deformations

50   in the southeastern margin of the Tibetan Plateau. The anisotropy in the lithosphere varies both laterally

51   and vertically as a result of the dynamic interactions of neighboring blocks as well as lithospheric

52   reactivation. The anisotropy in the asthenosphere is largely parallel to the regional absolute plate motion,

53   and the SKS splitting observed at the surface is the result of vertical integration of the contributions
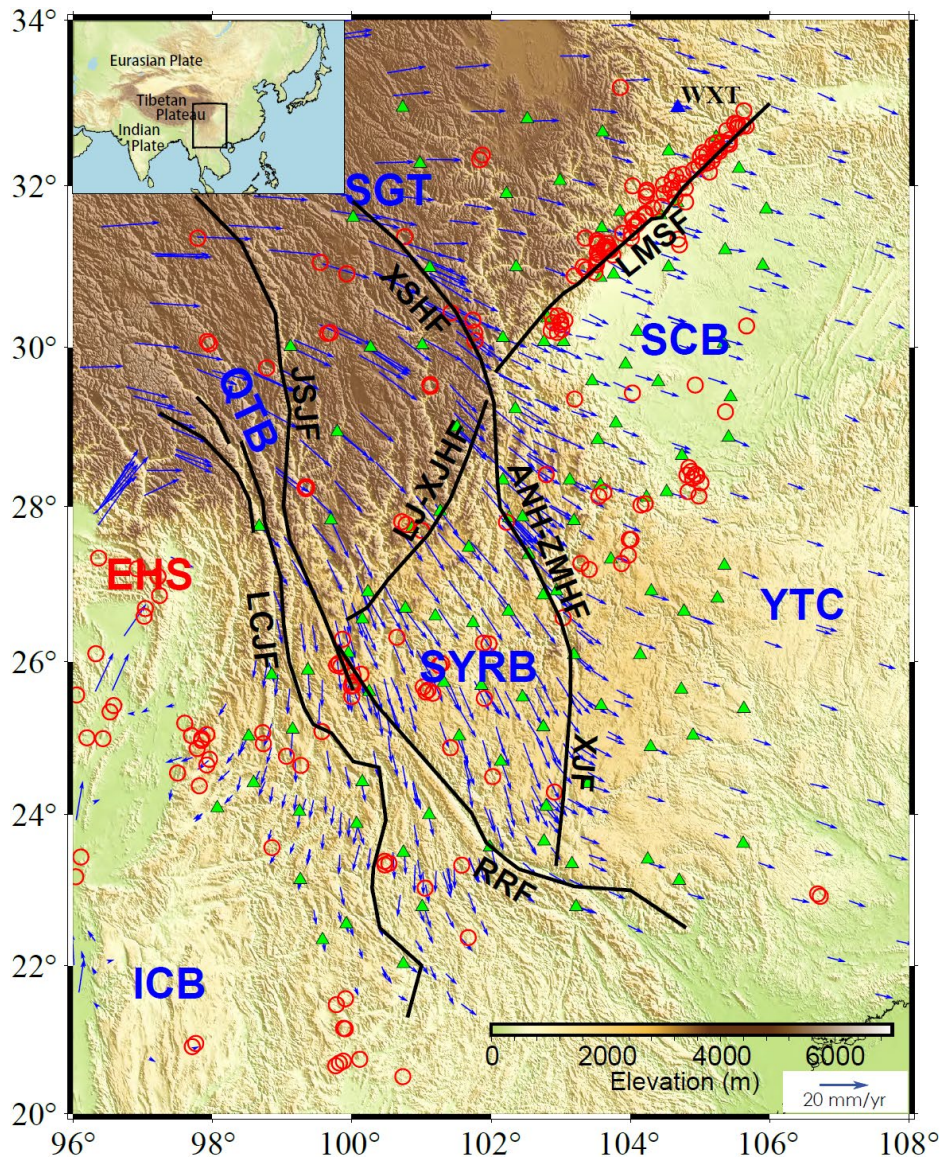
54   from lithosphere and asthenosphere.

55

56 **1 Introduction**

57 The ongoing Indian-Eurasian continental collision since 50 Ma has resulted in the greatest plateau

58 on Earth and deformed large parts of central and east Asia (Yin & Harrison, 2000; Kind et al.,

59 2002). Despite decades of study, questions remain over the dynamics of the lithospheric

60 deformation and asthenosphere flow beneath the Tibetan Plateau and the surrounding regions

61 (Royden et al., 2008).

62 The region in the southeastern margin of the Tibetan Plateau involves many active tectonic

63 blocks (Figure 1), including the Songpan-Ganzi Terrane (SGT), the Sichuan Basin (SCB), the

64 Sichuan-Yunnan Rhombic Block (SYRB), the Indo-China Block (ICB), the Qiangtang Block

65 (QTB), and the Yangtze Craton (YTC). The SGT is part of central Tibetan Plateau. Its eastern part

66 is separated from the SCB and SYRB by the Longmenshan Fault (LMSF) and Lijiang-Xiaojinhe Fault

67 (LJ-XJHF), respectively, and bounded in the south by the Jinshajiang Fault (JSJF) from the QTB. The

68 convergence between the Indian and Eurasian plates caused the SGT to expand eastward against

69 the SCB during the Cenozoic (Yin & Harrison, 2000). GPS observations show eastward crustal

70 motion of the eastern SGT with the crustal strain rate decreasing abruptly from ~20 mm/year

71 (relative to the YTC reference frame) in the interior SGT to ~3–4 mm/year or less in the vicinity of

72 central and southern segments of the LMSF, indicating that the eastward expansion of the SGT is

73 apparently resisted by the SCB (Shen et al., 2005; Zhang, 2013). Low-velocity zones and high-

74 conductivity bodies in the mid-lower crust under the SGT revealed by geophysical studies (Zhao

75 et al., 2012; Bao et al., 2020) suggest the existence of mid-lower crustal flow. However, these

76 geophysical anomalies exhibit strong lateral heterogeneity in eastern Tibet, implying a complex

77 internal deformation process. The SCB and SYRB are both parts of the YTC (Zhang et al., 2013;

78 Li et al., 2021). The former forms the rigid and stable northwestern margin of the YTC, while the

79 crust of the latter is extruding southeastward along the Anninghe-Zemuhe Fault (ANH-ZMHF) and

80 Xiaojiang Fault (XJF) in the east and the Red River Fault (RRF) in the southwest (Zhang et al., 2003).

81 The Lancangjiang Fault (LCJF) separates the narrow QTB in the east and the ICB in the west.

82 Crustal movements are predominantly characterized by a clockwise rotation around the Eastern

83 Himalayan Syntaxis (EHS), transforming the movement of the plateau material from eastward

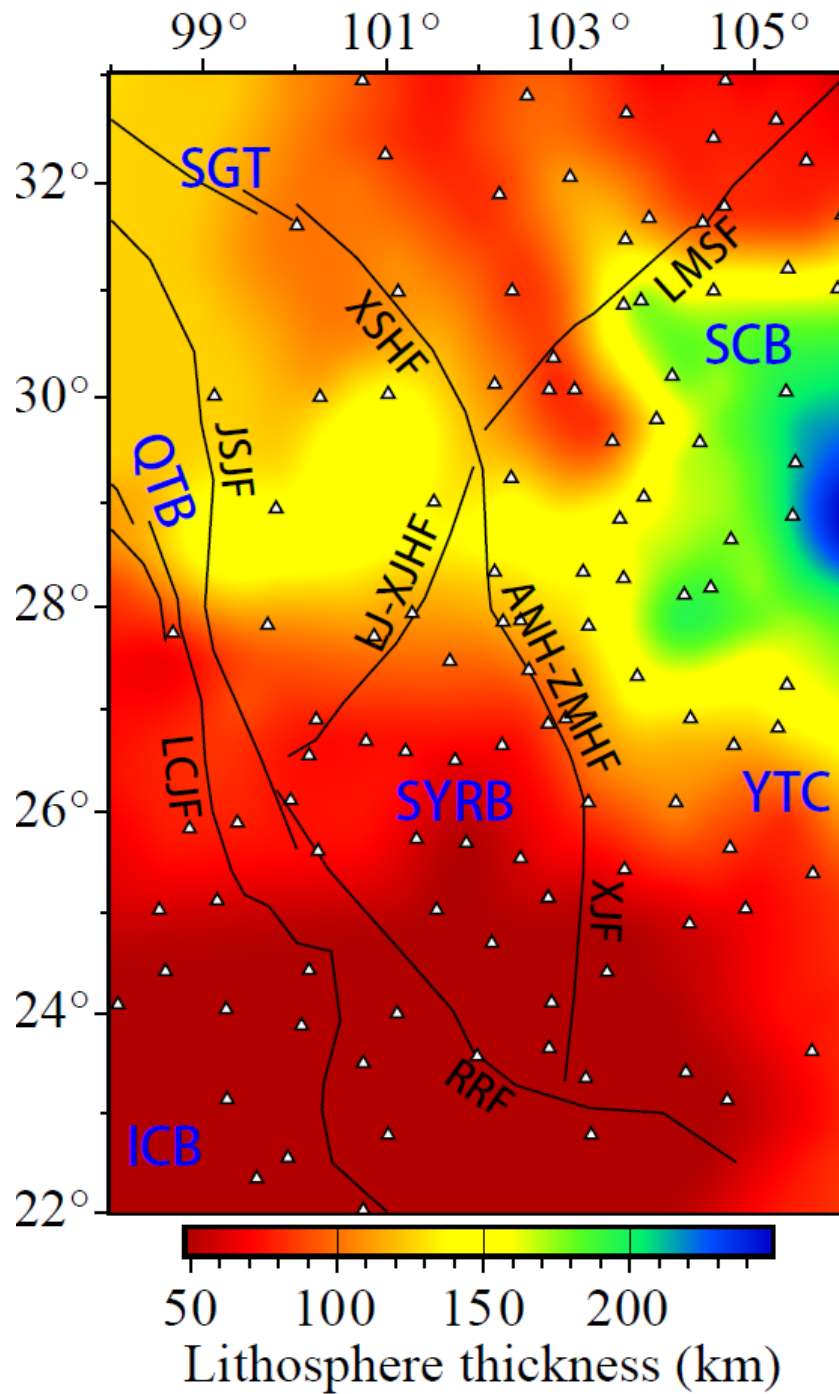84 north of the syntaxis to southeastward and southward further south (Wang & Shen, 2020).

85

86 **Figure 1**. Map of the tectonic environment of southeastern margin of the Tibetan Plateau with

87 seismic stations (green-filled triangles) and epicenters (red open circles) of earthquakes of

88 magnitude 5 and above from 2000 to 2022. The blue triangle marks the station WXT for which

89 SKS waveforms, splitting intensities and sensitivity kernels are shown in Figures 4, 5 and 7,

90 respectively. Major active faults are shown by thick black lines with abbreviated names in black,

91 including LMSF: Longmenshan Fault; XSHF: Xianshuihe Fault; JSJF: Jinshajiang Fault; LCJF:

92 Lancangjiang Fault; LJ-XJHF: Lijiang-Xiaojinhe Fault; ANH-ZMHF: Anninghe-Zemuhe Fault;

93 XJF: Xiaojiang Fault; and RRF: Red River Fault. Major active tectonic blocks are indicated by

94 abbreviated texts in blue, including SGT: Songpan-Ganzi Terrane; SCB: Sichuan Basin; QTB:

95 Qiangtang Block; SYRB: Sichuan-Yunnan Rhombic Block; YTC: Yangtze Craton; and ICB:

96 Indo-China Block. EHS stands for the Eastern Himalaya Syntax. Blue arrows show the GPS

97 velocities with respect to the Eurasian Plate (Wang & Shen, 2020). Background color shows the

98 topography. The black box in the inset map indicates the location of the main figure.

99   Over the past two decades, and in particular after the 12 May 2008 Wenchuan Mw7.9

100 earthquake on the LMSF, a large number of seismic stations have been deployed in the

101 southeastern margin of the Tibetan Plateau. Waveforms recorded by the growing number of

102 broadband stations have provided crucial data for studying the structure and dynamics of the crust

103 and upper mantle beneath the region, such as the variation in crustal thickness (Wang et al., 2017;

104 Xu et al., 2020), the widespread low-velocity anomalies in mid-lower crust revealed by receiver

105 function analysis (Hu et al., 2005; Xu et al., 2007; Zhang et al., 2009; Wang et al., 2010), Lg-wave

106 high-attenuation zones (Zhao et al., 2013; Wei & Zhao, 2019), joint inversion of receiver function

107 and surface wave dispersion (Liu et al., 2014), and body- and surface-wave tomographies (Huang et

108 al., 2002; Wang et al., 2003; Huang et al., 2009; Li et al., 2009; Wei & Zhao, 2022; Yang et al., 2019).

109   Across the LMSF, the drastic change in elevation from ~5–6 km in the west to a few hundred

110 meters in the east suggests large variation in the lithospheric thickness. Figure 2 shows the

111 LITHO1.0 model (Pasyanos et al., 2014) in the study region, where the lithosphere has a thickness

112 of less than 100 km in the northern and southern parts but ~150 km in mid latitudes. The thickest

113 lithosphere in the study region is more than 200 km beneath the SCB.

Figure 2. Lithosphere thickness in model LITHO1.0 (Pasyanos et al., 2014). Names of major faults and tectonic blocks are the same as in Figure 1.

Distribution of azimuthal anisotropy is an important proxy for deformation. There have been numerous studies devoted to the crustal anisotropy beneath the southeastern Tibetan Plateau

119   utilizing different methods, such as the Pms splitting (Sun et al., 2012; Cai et al., 2016; Han et al.,

120   2020), anisotropic tomography of P and Pn waves (Lei et al., 2014; Huang et al., 2018), surface

121   wave anisotropic tomography (Yang et al., 2010; Yao et al., 2010; Legendre et al., 2015; Zhang et

122   al., 2023), and the splitting of shear waves (Shi et al., 2012). In the upper crust, the fast axis directions

123   are mainly parallel to the strike of active faults (e.g., Yao et al., 2010; Shi et al., 2012; Huang et al.,

124   2018), whereas the anisotropic pattern in the lower crust is different. Huang et al. (2018) showed

125   that the fast velocity direction deviates from the strikes of active faults significantly using P-wave

126   anisotropic tomography. Han et al. (2020) used the Markov-chain Monte Carlo inversion of receiver

127   functions to isolate the effect of potential dipping interfaces. Their results showed that the fast axis

128   directions in the lower crust are in good agreement with the topography contours, implying that the

129   gravitational potential may be the driving force for the crustal deformation in southeastern Tibet.

130   The XKS-wave splitting is routinely used to probe the anisotropic structure in the upper mantle

131   (Long & Becker, 2010). Flesch et al. (2005) conducted joint analysis of GPS, surface geology and

132   shear-wave splitting measurements to argue for a vertically coherent deformation in the crust and

133   upper mantle in the Tibetan Plateau but a decoupling beneath Yunnan Province in southwestern

134   China. Lev et al. (2006) also supported the decoupling beneath Yunnan using shear-wave splitting

135   observations, but they were not able to constrain the level of coupling beneath the Tibetan Plateau.

136   Based on a joint analysis using more shear-wave splitting measurements and GPS observations,

137   Wang et al. (2008) argued for the crust-mantle coupling in the Tibetan Plateau and the surrounding

138   regions.

139   Substantial efforts have been made to develop a theoretical framework as well as practical

140   strategies for the inversion of 3D distribution of anisotropy. A fullwave approach has been developed

141   for the measurement of shear-wave splitting intensities and interpretation in terms of shear-wave

142 azimuthal anisotropy parameters (Chevrot, 2000; Favier & Chevrot, 2003; Chevrot, 2006; Sieminski

143 et al., 2008; Monteiller & Chevrot, 2011; Lin et al., 2014a), which has been applied to anisotropy

144 tomographies for southern California (Monteiller & Chevrot, 2011; Lin et al., 2014b), the High

145 Lava Plain (Mondal & Long, 2020), and the southeastern Tibetan Plateau (Huang & Chevrot,

146 2021). The depth variations of anisotropy obtained by these studies have shed new lights in

147 understanding the sources of anisotropy and the associated mantle dynamics.

148   In this study, we conduct a fullwave multiscale anisotropy tomography for the southeastern

149 margin of the Tibet Plateau. We collect seismic records at regional permanent broadband

150 stations from globally distributed earthquakes and obtain high-quality measurements of SKS

151 splitting intensities. We then invert the splitting intensities using a wavelet-based parameterization

152 of the 3D model to achieve a multi-scale resolution to the anisotropic structure. We also provide

153 an interpretation of our anisotropic model for the southeastern margin of the Tibet Plateau in

154 terms of regional geodynamics.
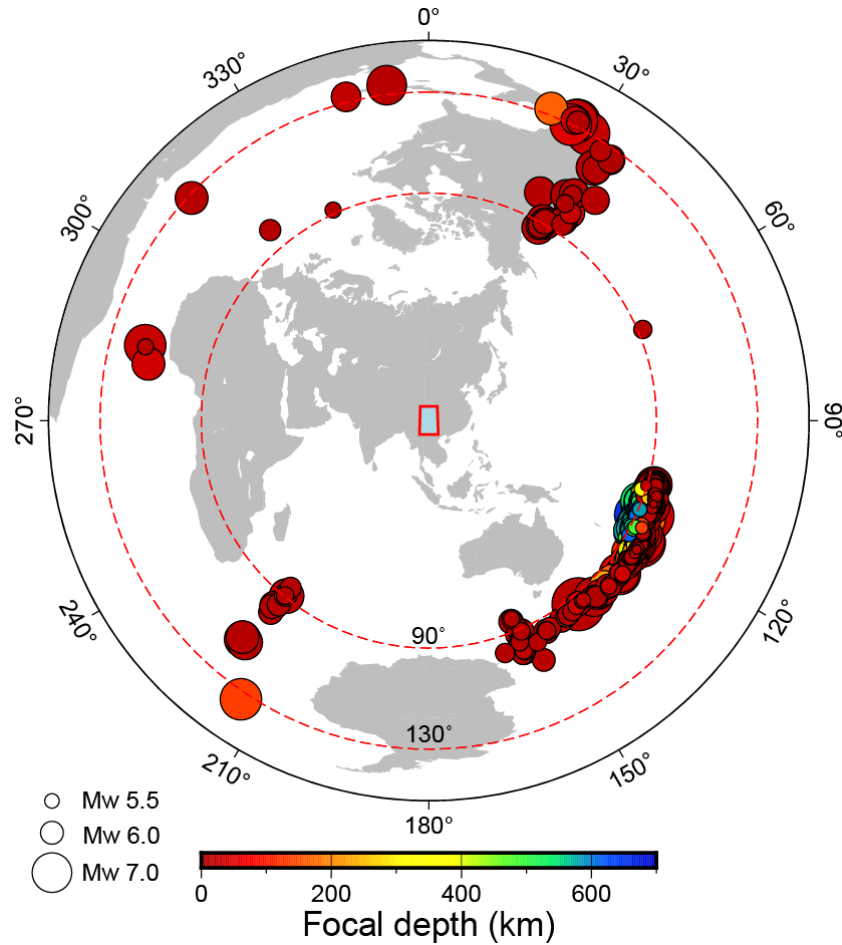
155 **2 Data and Methods**

156 **2.1 Waveform records**

157 We collect waveforms recorded by 111 permanent broadband stations (green triangles in Figure 1)

158 deployed in the study region. To guarantee a wide range of azimuthal distribution, we select events

159 of magnitude Mw ≥ 5.5 from 2009 to 2020, located in the epicentral distance range of 90°–130°.

160 After quality control of the waveforms and removal of outliers of the data (see Section 2.2), a total

161 of 470 events are used in the subsequent inversions. Figure 3 displays the event distribution.

162 **2.2 Splitting intensity measurements**

163 Shear wave splitting measurement is nowadays a routine procedure in the study of seismic

164 anisotropy. Several previous studies have documented the measured SKS splitting parameters (fast

165   directions and delay times) at stations in our study region (e.g., Chang et al., 2015; Yang et al.,

166   2018; Liu et al., 2020; Huang & Chevrot, 2021; Li et al., 2021). In this study, we invert for the

167   3D anisotropy structure using the splitting intensity (SI) measurements obtained by computing the

168   zero-lag cross-correlation between the transverse-component record and the time derivative of the

169   radial-component record (Chevrot, 2000).

170

171   **Figure 3**. Distribution of 470 teleseismic events used for SKS splitting intensity inversion in this

172   study. Events of magnitudes Mw5.5 and greater in the epicentral distance range of 90°–130° during

173   2009–2020 are selected. The red box in the center indicates the study area.

174   For a given station, the SI of the SKS wave from the *i*-th event is defined as

$$S_i = -2 \frac{\int_{t_{i1}}^{t_{i2}} \dot{u}_i^R(t) u_i^T(t) dt}{\int_{t_{i1}}^{t_{i2}} [\dot{u}_i^R(t)]^2 dt}, \tag{1}$$

175

176   where $[t_{i1}, t_{i2}]$ is the time window for the SKS wave, and $u_i^R(t)$ and $u_i^T(t)$ are the radial and

177   transverse-component records, respectively, from the *i*-th event. A dot above a variable indicates

178   derivative with respect to time. The conventional SKS splitting parameters at the given station,

179   namely the fast-direction azimuth θ and delay time Δt, are related to the SIs measured at the station

180   from all events through a sinusoidal curve fitting (Chevrot, 2000; Lin et al., 2014a):

$$S_i = \Delta t \sin 2(\theta - \theta_i^b), \tag{2}$$

182   where θ_i^b is the back azimuth of the *i*-th event.
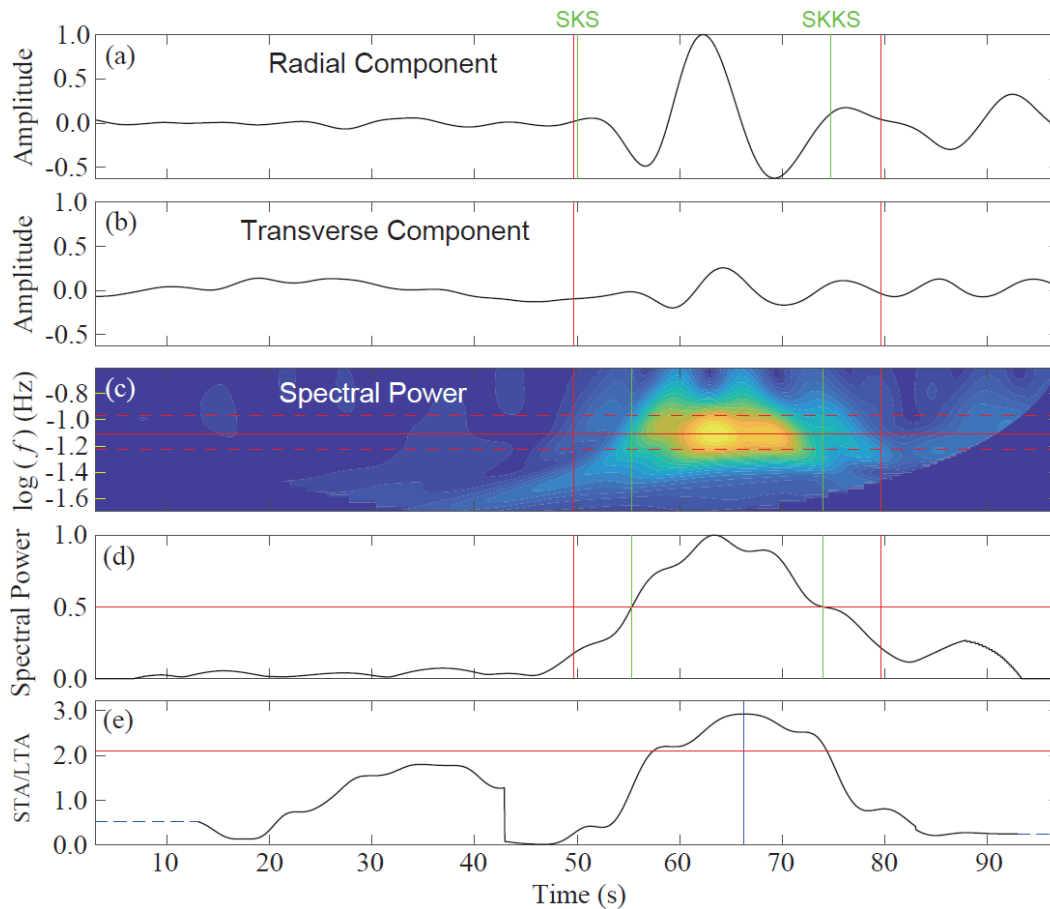
183   In this study, we obtain the SI measurements of SKS waves with the help of SplitRacer (Link

184   et al., 2022), an efficient and automatic toolbox developed for the measurement and quality control

185   of XKS splittings. An example of the SplitRacer processing is shown in Figure 4. We use SplitRacer

186   to determine the SKS time window automatically, followed by a manual check on the quality of the

187   SKS signals. Then, we calculate the SIs using Eq. (1). The period band we use in this study is 8–

188   50 s considering the dominant periods of the SKS signals as well as minimizing the interference

189   with neighboring phases. As shown in Figure 4, the spectral powers of the radial- and transverse-

190   component records are calculated by the short-time Fourier transform (Quatieri, 2006) and summed.

191   Then, the dominant frequency band of the SKS waveform can be identified (between the red dashed

192   horizontal lines in Figure 4c). At each time, the powers within the dominant frequency band are

193   summed (Figure 4d), which defines the SKS window by the two crossing points at 50% of the peak

194   level (vertical green lines in Figure 4d). The final SKS window is given by either expanding or

195   shrinking the 50% energy window to a fixed 30-s window (red vertical lines). After completing

196   the quality check using SplitRacer, we obtain a total of 12,457 SKS wave SI measurements.

197   Following Chevrot (2000), we estimate the uncertainty of each SI measurement using the

198   following equation

$$\sigma_i = \sqrt{\frac{1}{N_i}\left\{\sum_{j=1}^{N_i}[u_i^T(t_j)]^2 - \frac{S_i^2}{4}\sum_{j=1}^{N_i}[\dot{u}_i^R(t_j)]^2\right\}},$$

(3)

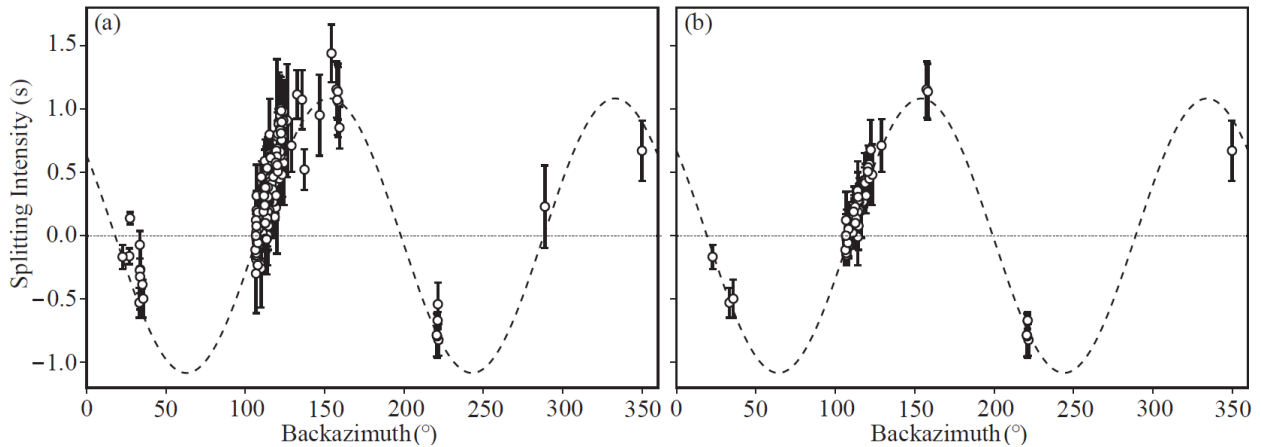where S_i is the i-th SI measurement, and N_i is the number of time samples used for the window to obtain the measurement.

Figure 4. Example of SKS window selection using SplitRacer. (a) and (b) show normalized radial and transverse records, respectively, around the SKS arrival at station WXT (blue triangle in Figure 1) from the 24 June 2019 earthquake in New Zealand with a back azimuth of 122°. The green lines mark the theoretical SKS and SKKS arrival times of seismic phases corresponding to the event of interest. Red vertical lines mark the start and end time of the final window containing the SKS waveform. (c) Summed spectral power of the spectrogram of the radial and transverse records in (a) and (b). The red horizontal line marks the frequency of maximum spectral power, and the red dashed lines show the frequency bounds of more than 80% of the maximum. The green vertical lines mark the time window in which the summed spectral power is more than 50% of the

212 maximum. (d) Summed spectral power over all frequencies. The green vertical lines mark the time

213 window in which the summed spectral energy is more than 50% of the maximum. (e) STA/LTA

214 ratio of the radial-component record used as quality check. The blue vertical line denotes the time

215 when the STA/LTA ratio reaches its peak within the window determined in (d). The red horizontal

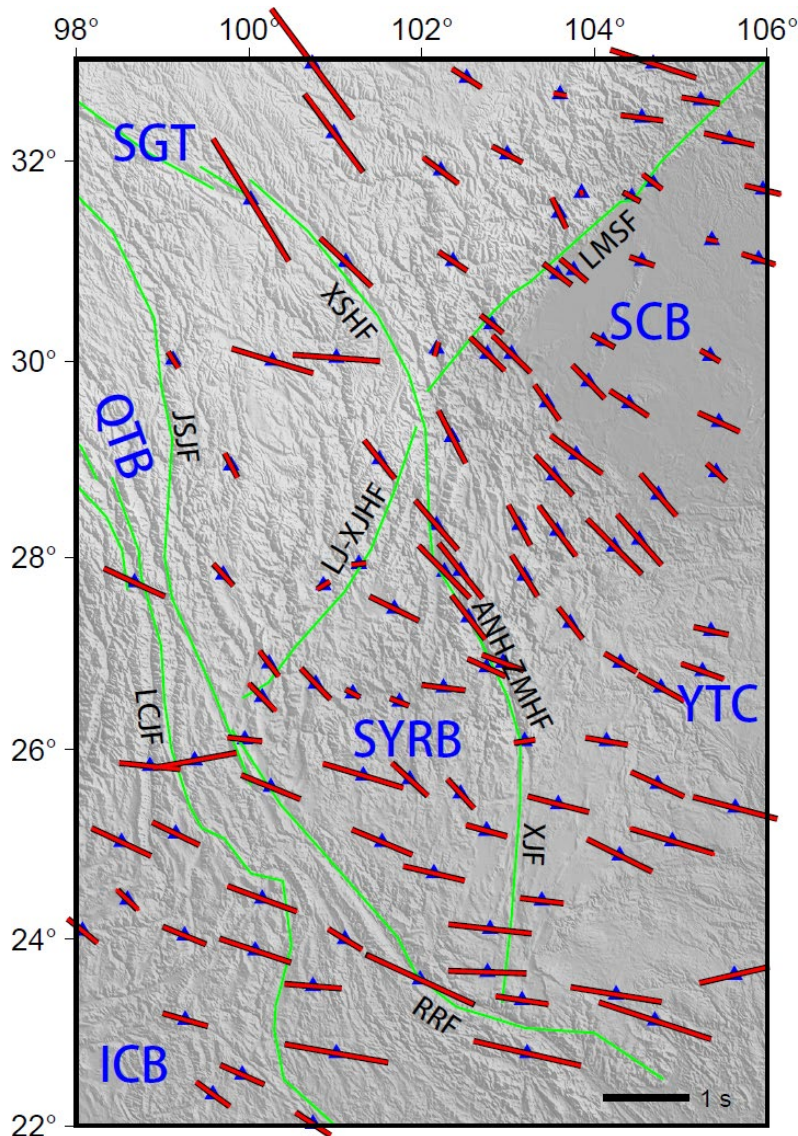216 line is the acceptance threshold of 2.1 (Link et al., 2022).

217   We further clean our dataset of outliers based on two criteria: (1) At a given station, SI

218 measurements with uncertainties σ_i larger than 1.5 times the average uncertainty $\bar{\sigma}$ for that station,

219 i.e. $\sigma_i > 1.5\bar{\sigma}$, are removed; (2) all SI measurements at a given station are fit by a sinusoidal curve,

220 and measurements that deviate from the sinusoidal curves by more than $2\sigma_i$ are also removed.

221 After removing the outliers, we retain a total of 5,216 high-quality SI measurements as our final

222 dataset for subsequent anisotropy inversion. The standard deviation of the final dataset (the

223 average of uncertainties of all retained data) is 0.074 s. Figure 5 shows the effect on the distribution

224 of SI measurements before and after applying the above two criteria for station WXT, which

225 reduces the number of SI data from 184 to 61.

226

227 **Figure 5**. Variations of measured SI with event back azimuth for station WXT (blue triangle in

228 Figure 1) before (a) and after (b) removal of SI outliers. The vertical error bars show two standard

229 deviations ($2\sigma_i$) of individual measurements. The dashed lines represent the sinusoidal curves that

230 best fit the measurements. According to Eq. (2), the conventional SKS splitting parameters for this

231 station are: $\Delta t = 1.08$ s and $\theta = 109.14°$.

232   Based on Eq. (2), we can obtain the conventional fast-direction azimuth θ and delay time Δt

233 at each station using all the SI measurements, and they are displayed in Figure 6. The spatial

234   distribution of θ has a similar pattern as seen in previous studies, i.e. a generally NW-SE oriented

235   fast axis and a nearly uniform EW alignment of the fast-axis directions south of ~26ºN latitude.

236

Figure 6. Black line segments show the conventional SKS fast-direction azimuths and delay times
at all station obtained from the SI measurements according to Eq. (2). Red line segments are fast-
direction azimuths and delay times derived from Eq. (2) based on the model-predicted SIs obtained
by integrating the sensitivity kernels (see Figure 7) with the anisotropy model in Figure 12
according to Eq. (4). Names of major faults and tectonic blocks are the same as in Figure 1.

2.3 Multiscale inversion for 3D anisotropic structure

We implement the full-wave multiscale anisotropy tomography framework developed by Lin et al.
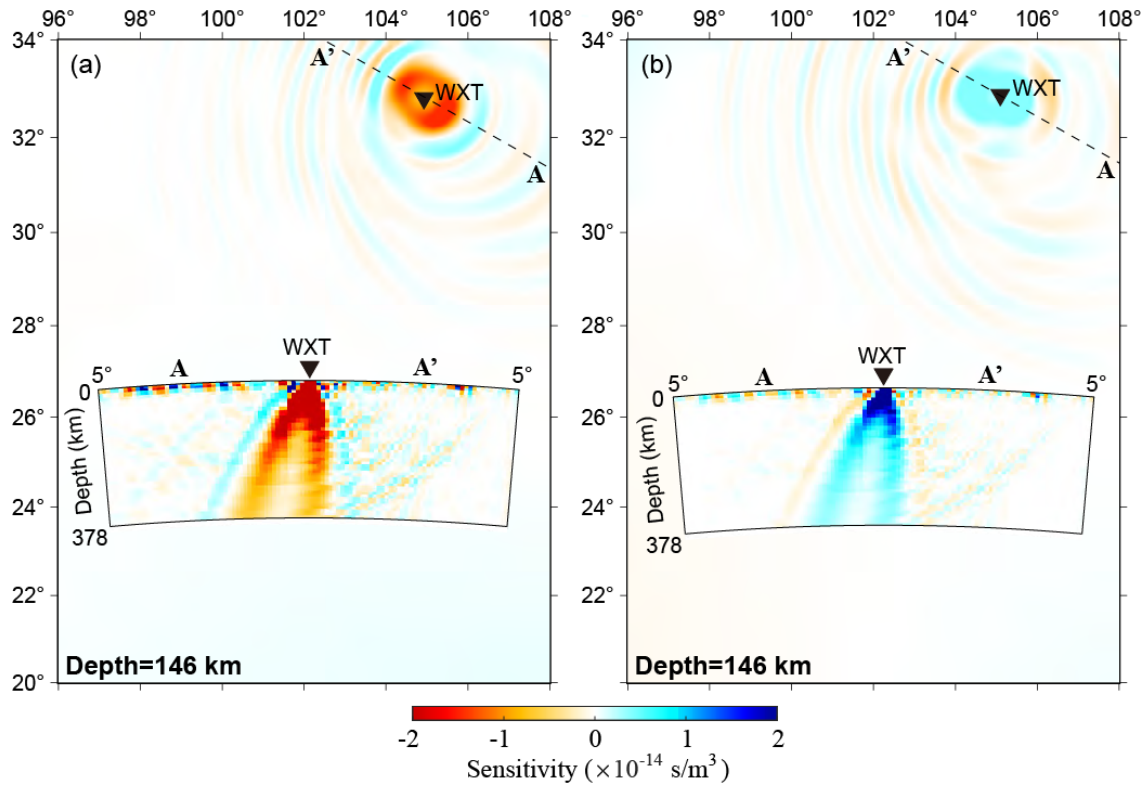
244   (2014b). Here we briefly describe our methodology. Interested readers may consult Lin et al.

245   (2014b) for a full description of the method.

246   Becker et al. (2006) point out that upper-mantle anisotropy is to first-order hexagonal and the

247   hexagonal parameters ε (describing P-wave anisotropy), γ (describing S-wave anisotropy) and δ

248   (an extra parameter describing the shape of P- and S-wave slowness surfaces) are strongly

249   correlated. Furthermore, Zhao & Chevrot (2011) demonstrated that the sensitivity of the SI of

250   an SKS wave is mostly sensitive to γ, and is about 10 times larger than that to the isotropic

251   heterogeneity. This allows us to considerably simplify the modeling of upper mantle anisotropy in

252   two aspects: (1) it is sufficient to use 1D reference model; and (2) the anisotropy can be described by

253   only two parameters: the strength of anisotropy γ and the azimuth ϕ_f of the symmetry axis of

254   anisotropy. We assume that the symmetry axis is horizontal since the sub-vertically propagating

255   SKS waves are insensitive to the dip angle of the symmetry axis of anisotropy (Mondal & Long,

256   2019). Note that the anisotropy strength γ and azimuth ϕ_f are spatially varying, and the

257   dependence of the SI on ϕ_f is nonlinear. As documented in Favier & Chevrot (2003), we can

258   introduce two independent parameters, $\gamma_c = \gamma \cos(2\phi_f)$ and $\gamma_s = \gamma \sin(2\phi_f)$ to enable a linear

259   relationship with the SI measurement

$$S = \iiint \left[K_{\gamma_c}^S(\boldsymbol{r})\gamma_c(\boldsymbol{r}) + K_{\gamma_s}^S(\boldsymbol{r})\gamma_s(\boldsymbol{r}) \right] d\boldsymbol{r}, \tag{4}$$

261   where $K_{\gamma_c}^S$ and $K_{\gamma_s}^S$ are the Fréchet sensitivity kernels of the splitting intensity S to γ_c and γ_s,

262   respectively. After obtaining γ_c and γ_s from a linear inversion, we can obtain the more familiar

263   anisotropy parameters by utilizing the relations: $\phi_f(\boldsymbol{r}) = 0.5\tan^{-1}[\gamma_s(\boldsymbol{r})/\gamma_c(\boldsymbol{r})]$ and $\gamma(\boldsymbol{r}) =$

264     $\sqrt{[\gamma_c(\boldsymbol{r})]^2 + [\gamma_s(\boldsymbol{r})]^2}$. In this study, we use PREM (Dziewonski & Anderson, 1981) as the

265   reference model and compute the sensitivity kernels using the normal mode summation algorithm

266   developed by Zhao & Chevrot (2011). Examples of the Fréchet kernels for γ_c and γ_s are shown in

267   Figure 7. Chevrot (2006) first noted the similarity between the definition of the SI in Eq. (1) and

268   that of the traveltime delay (e.g. Dahlen et al., 2000; Zhao et al., 2000), which implies that the sensitivity

269   kernels of the SI to anisotropy parameters exhibit the distinct banana-doughnut shapes typically seen in

270   the sensitivities of the finite-frequency traveltimes to isotropic velocities, as shown in Figure 7.

271

Figure 7. Examples of the sensitivity kernels of the SI to shear wave anisotropy parameters γ_c (a)

273   and γ_s (b) shown in mapviews for the 146-km depth and in profiles (insets) along source-receiver

274   path AA' for station WXT (blue triangle in Figure 1). The SKS wave is from the 24 June 2019

275   event in New Zealand with a back azimuth of 122°, and the waveforms are shown in Figure 4.

276   As in Lin et al. (2014b), we adopt a wavelet-based model parameterization (Chiao & Kuo,

277   2001) to obtain multi-scale resolutions in both sparsely- and densely-sampled regions of data

278   coverage. The inverse problem can be expressed as:

$$(\mathbf{GW}^{-1})(\mathbf{Wm}) = \mathbf{d}, \tag{5}$$

280   where **G** is Gram matrix containing the Fréchet kernels, **W** is the 3D wavelet transformation matrix,

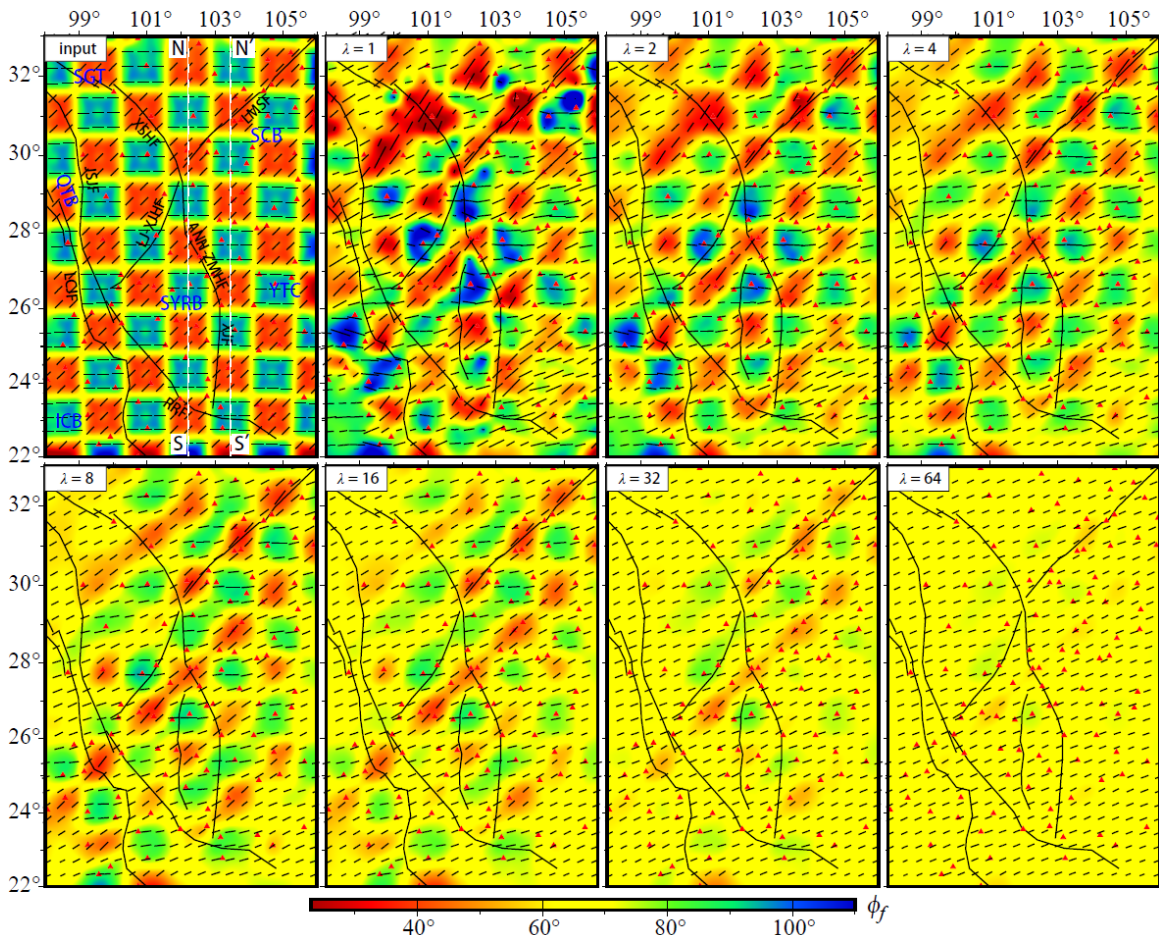281   **m** is the vector comprising the model parameters at spatial nodes, and **d** is the data vector of the

282   SI measurements. In this study, we first parameterize the model by a 3D mesh with 33×33 nodes

283   horizontally and 17 nodes vertically, and apply the operator $(\mathbf{W}^{-1})^T$ on each row of $\mathbf{G}$. A damped

284   least-squares solution to the inverse problem in Eq. (5) is solved by the LSQR algorithm (Paige &

285   Saunders, 1982), with the damping factor λ selected empirically by a series of inversion

286   experiments (see Section 2.4), and the final model can be obtained by an inverse wavelet transform.

287   Readers may refer to Hung et al. (2011) for implementation details of the multi-scale

288   parameterization. The wavelet approach achieves a finer spatial resolution in regions of better data

289   coverage and coarser resolution in less well-sampled regions, thus resolving the structure with an

290   objective and data-driven multi-scale resolution.

291   **2.4 Resolution tests**

292   Careful selection of the damping factor λ and objectively evaluating the resolution for a given

293   dataset in an inversion problem is paramount to interpreting the inversion results. Thus, it is important

294   to characterize how reliable our anisotropic models are, and to restrict our interpretations to robust

295   features that are well-resolved and required by the observations.

296   We present three sets of resolution tests to illustrate the selection of the optimal damping

297   factor and the resulting resolution of our SI dataset. Given the input model in a resolution test, the

298   SI is predicted for each SKS path in our final dataset by integrating the products of 3D sensitivity

299   kernels with the distributions of γ_c and γ_s in the input model according to Eq. (4). A Gaussian

300   noise with the same standard deviation as our final inversion dataset (0.074 s) is added to the SI

301   predictions. We first perform a series of tests using checkerboards of two different sizes (1º x 1º

302   and 1.5º x 1.5º) with horizontally alternating azimuthal angles of fast axes $\phi_f = 90^\circ$ and $\phi_f = 45^\circ$

303   but a fixed anisotropy strength $\gamma = 4\%$. Figure 8 shows the input and recovered models for
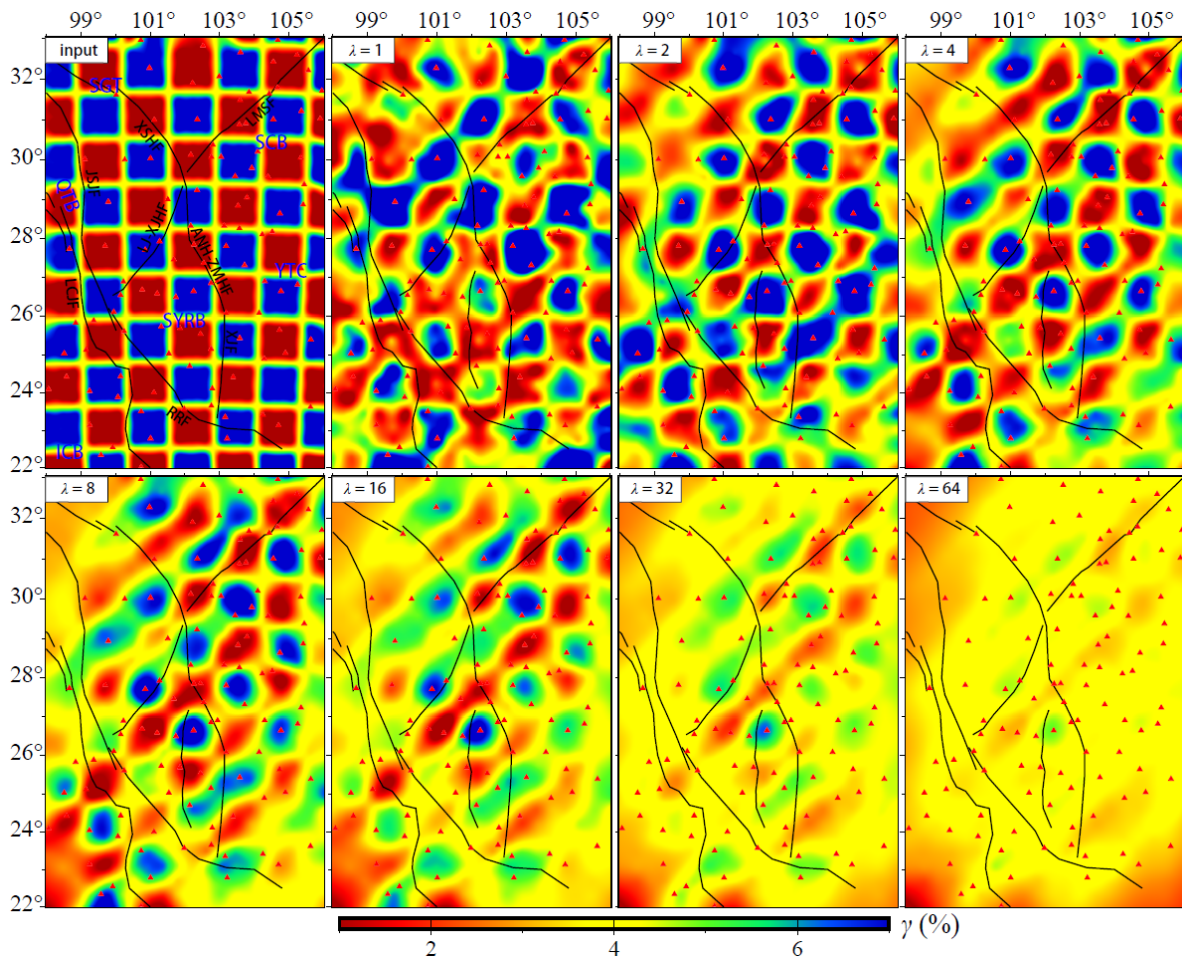
304   different values of the damping factor λ at a depth of 55 km for the 1° x 1° checkerboard test. The

305   effect of damping factor on the anisotropy pattern in the inversion result is obvious. The recovery

306   results suggest an optimal damping factor of $\lambda = 4$, and the checkerboard pattern is well-resolved

307   in most parts of the study area except in the northwest and southeast corners where stations are

308   more sparse. Results for recovered models at different depths as well as for 1.5° x 1.5°

309   checkerboards are presented in Figures S1 and S3 in Supporting Information.

310

311   **Figure 8**. Resolution tests for the azimuth of symmetry axis using 1° x 1° checkerboard. (Top-left)

312   The input model has horizontally alternating azimuthal angles of fast axes $\phi_f = 90°$ and $\phi_f = 45°$

313   shown by both the color and the directions of the line segments, and a fixed anisotropy strength

314    $\gamma = 4\%$ represented by the lengths of the line segments. The two white dashed lines show the

315   locations of profiles NS and N'S' in Figure 11. The other panels show the recovered models at a

316   depth of 55 km for different damping factors λ. We choose $\lambda = 4$ as the optimal value for the

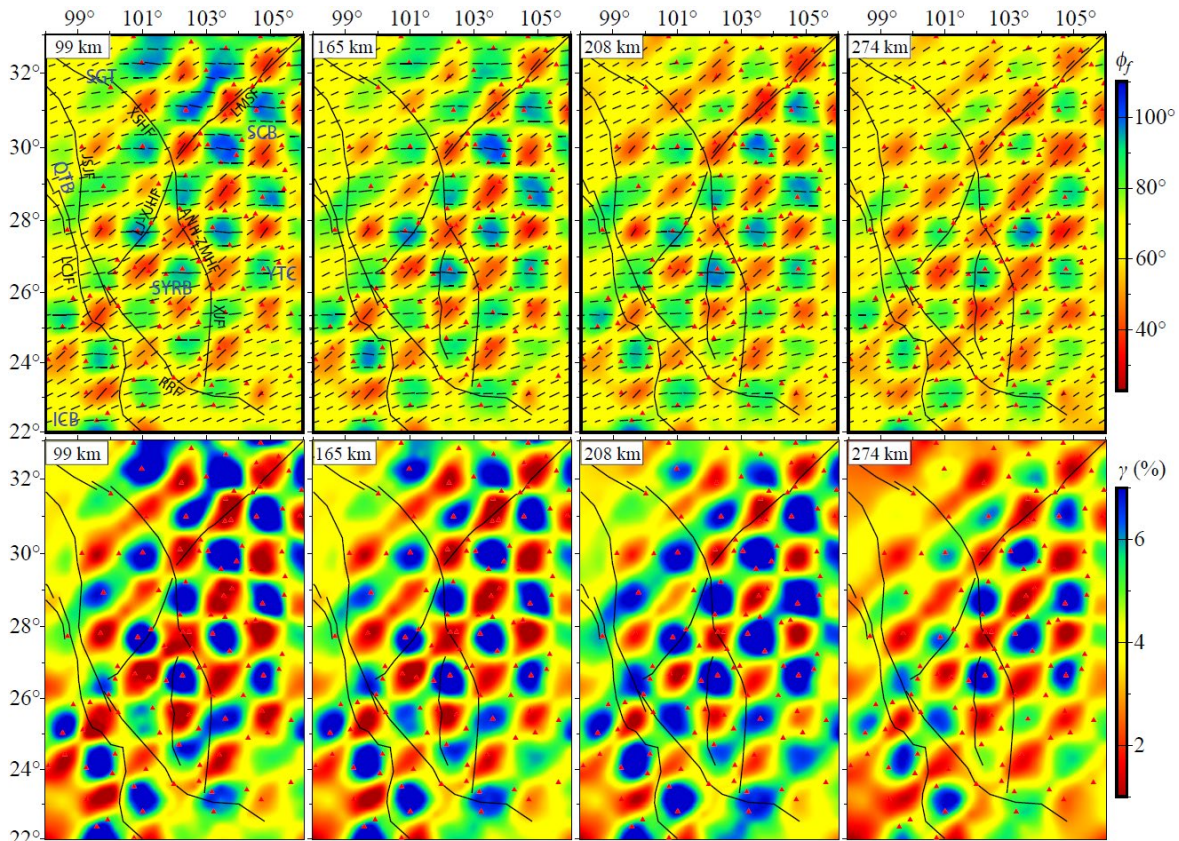317   damping factor (top-right panel). Red triangles show locations of stations used.

318   In the second set of tests, we use input checkerboard models with a fixed azimuthal angle of

319   symmetry axis $\phi_f = 22.5°$ but alternating perturbations of anisotropy strength of $\delta\gamma = \pm 3\%$

320   relative to a background anisotropy strength of $\gamma = 4\%$. Figure 9 shows the recovery results at the

321   depth of 55 km using different damping factors for the 1° x 1° input checkerboard model. Results

322   for recovered models at different depths as well as for 1.5° x 1.5° checkerboards are presented in

323   Figures S2 and S4 in Supporting Information.

324

325   **Figure 9**. Resolution test using 1° x 1° checkerboard. (Top-left) The input model has horizontally

326   alternating anisotropy strengths shown by the colors representing perturbations of $\delta\gamma = \pm 3\%$

327   relative to a background anisotropy strength of $\gamma = 4\%$ and a fixed azimuthal angle of symmetry

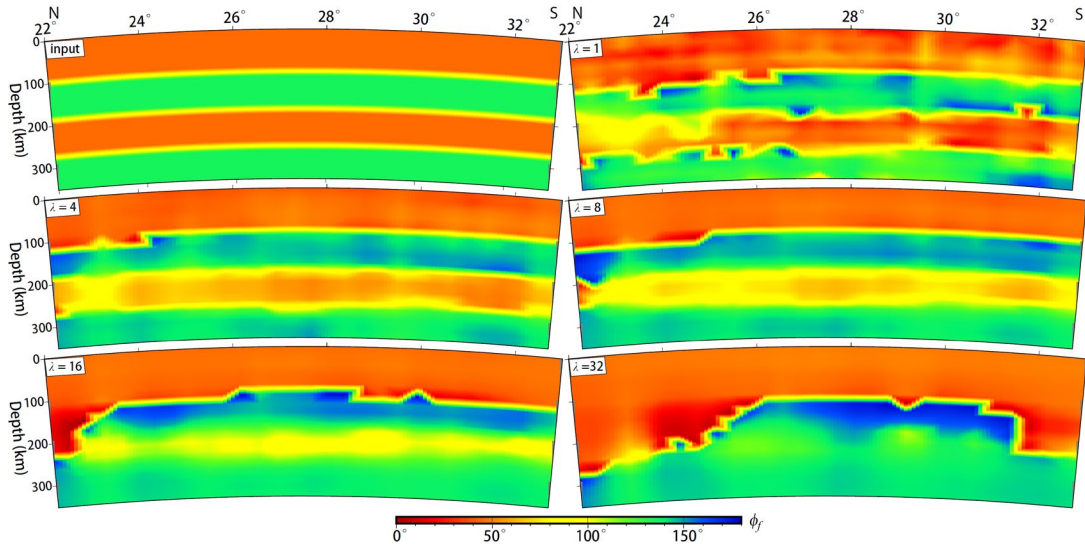328   axis $\phi_f = 22.5°$. The other panels show the recovered models at a depth of 55 km for different

329   damping factors λ. We choose $\lambda = 4$ as the optimal value for the damping factor (top-right panel).

330   Red triangles show locations of stations used.

331   The tests in Figures 8 and 9 both show that the damping factor of $\lambda = 4$ yields the best

332   resolved checkerboard pattern. For convenience, resolution test results at different depths for

333   damping factor $\lambda = 4$ are collected and displayed in Figure 10.

334

335   **Figure 10**. Resolution test using 1º x 1º checkerboard with damping factor $\lambda = 4$. (Upper panels)

336   Recovered model at the depths of 99 km, 165 km, 208 km and 274 km for an input model having

337   horizontally alternating azimuthal angles of fast axes $\phi_f = 90°$ and $\phi_f = 45°$ with a fixed

338   anisotropy strength $\gamma = 4\%$. The input model and the recovered model at 55-km depth are shown

339   in Figure 8. (Lower panels) Recovered model at the depths of 99 km, 165 km, 208 km and 274 km

340   for an input model with horizontally alternating anisotropy strengths of $\gamma = 1\%$ and $\gamma = 7\%$ with

341   a fixed azimuthal angle of symmetry axis $\phi_f = 22.5°$. The input model and the recovered model

342   at 55-km depth are shown in Figure 9. Red triangles show locations of stations used.

343   The third set of tests is intended to probe the depth resolution of our SI dataset with full-

344   waveform anisotropy tomography. We use input models with a fixed anisotropy strength of $\gamma =$

345   4% but several layers of alternating azimuthal angles of symmetry axes. Figure 11 shows the

346   recovery results for a 4-layer input model along a north-south vertical cross-section (cross-section

347   NS in the top-left panel of Figure 8) for different damping factors.

348

349   **Figure 11**. Resolution tests for an input model with 4 layers of alternating azimuthal angles of

350   symmetry axes $\phi_f = 45°$ and $\phi_f = 135°$ but a fixed anisotropy strength of $\gamma = 4\%$. Shown here

351   are the input model (top-left panel) and recovered models for different damping factors λ along

352   the north-south cross-section NS through the middle of the study region (see top-left panel in

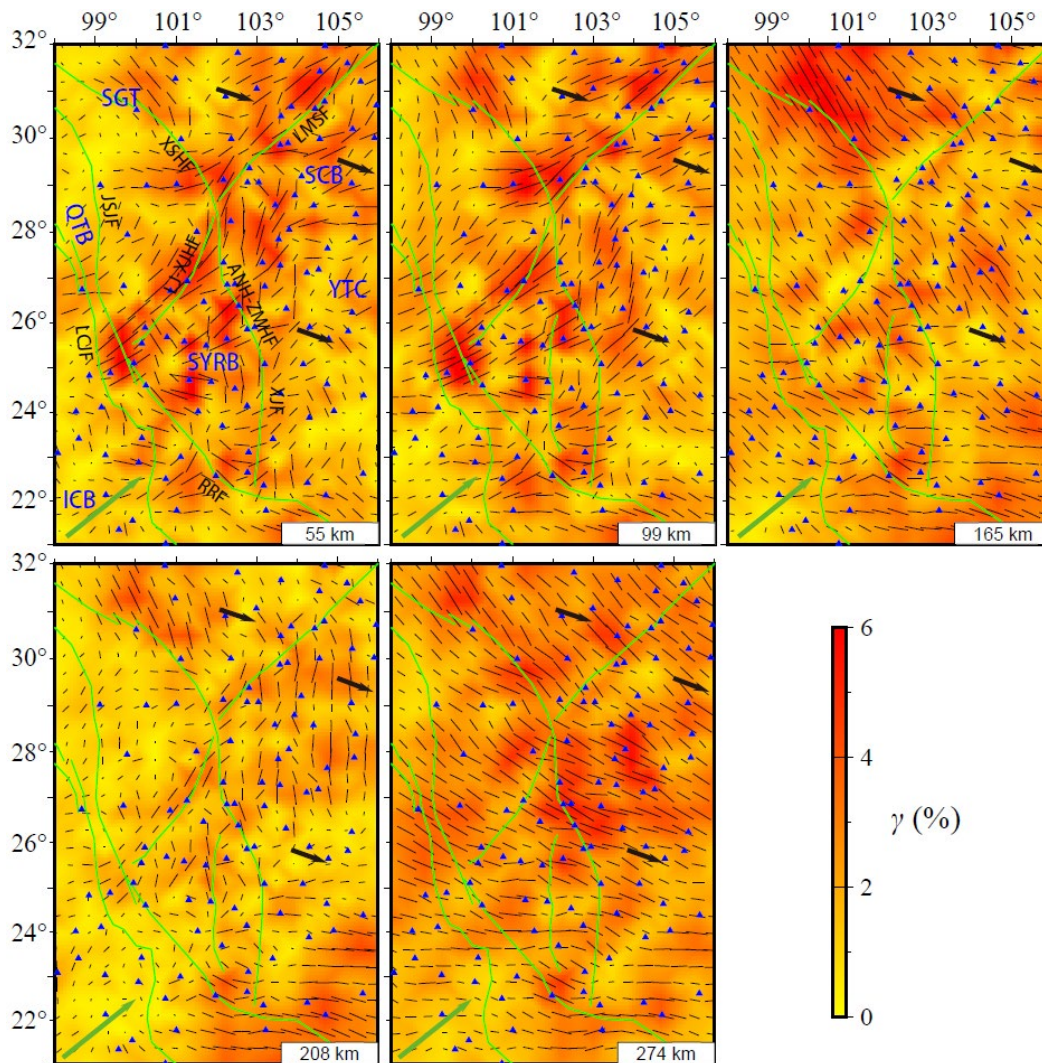353   Figure 8). The optimal damping is $\lambda = 4$ (middle-left panel).

354   Recovered models along another profile as well as for a 2-layer input model are presented in

355   Supporting Information (Figures S5-S8). These results also suggest an optimal damping factor of

356    $\lambda = 4$ in most parts of the study area. Based on all the resolution test results, we determine $\lambda = 4$

357   to be the optimal damping factor for the SI data inversions in this study.

358   The above resolution tests demonstrate that with the available distributions of seismic stations

359   and teleseismic earthquakes, our SKS wave SI dataset can resolve reasonably well the shear-wave

360   azimuthal anisotropy with a horizontal dimension of 1º x 1º and a vertical thickness of ~100 km in

361   the main part of the study region. Near the western border and in the SE corner, the resolution is

362   poor due to larger station spacing and fewer crossing SKS ray paths.

363   **3 Result**

364   As stated in Section 2.2, our final dataset contains 5,216 SI measurements at 111 permanent seismic

365   stations from 470 events, which are used to invert for the 3D azimuthal anisotropy structure of the

366   study region. Figure 12 displays our inverted model at five representative depths.

367

368   **Figure 12**. Three-dimensional anisotropic model for southeast margin of the Tibetan Plateau at 55

369   km, 99 km, 165 km, 208 km and 274 km depths. The anisotropy strength and the azimuth of the

370   fast axes are shown by the background color and the black line segments, respectively. The lengths

371   of the line segments are proportional to the anisotropy strength. The black and green arrows denote

372   the absolute plate motion (APM) of the Eurasian and Indian plates, respectively, according to the

373   model NNR-MORVEL56 (Argus et al., 2011). Names of major faults and tectonic blocks are the

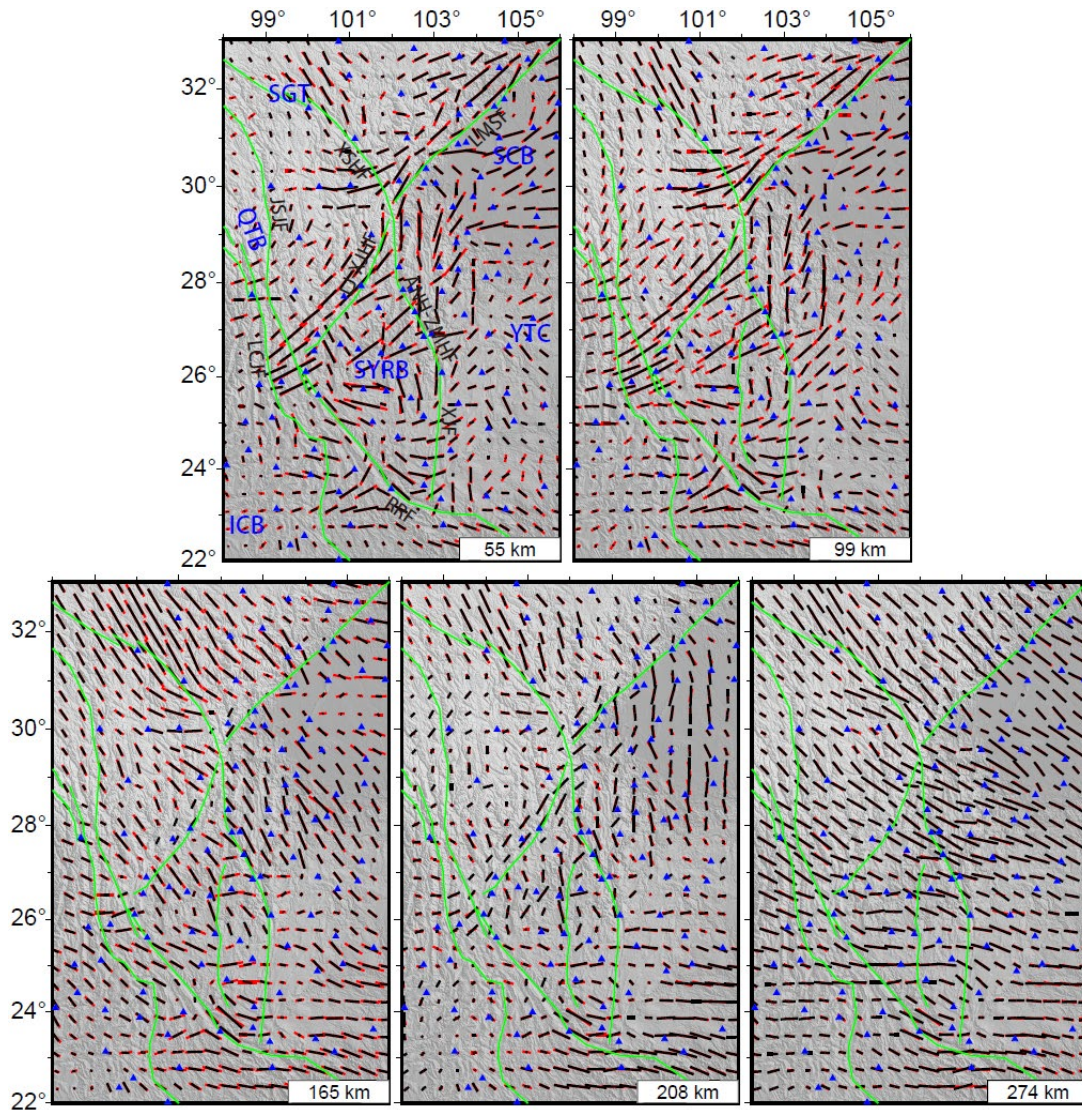374   same as in Figure 1. Blue triangles show locations of stations used.

375   As a first check of the inversion result, we calculate the model-predicted conventional SKS

376   splitting time Δt and fast-direction azimuth θ by integrating the anisotropy model (Figure 12) with

377   sensitivity kernels (Figure 7) according to Eq. (4) and compare with observations. The comparison

378   in Figure 6 shows excellent agreement between the model-predicted splitting parameters with

379   observations at all stations.

380   We also carry out a recovery test for our inversion result, in which we use the model in Figure

381   12 as the input model and calculate the synthetic SI data, then invert them using the same model

382   discretization and damping factor as in the inversion of the real data. The comparison in Figure 13

383   shows that the output model strongly resembles the input model at all depths. The synthetic inversion

384   successfully reproduces all the major features of the input model.

385   **4 Discussion**

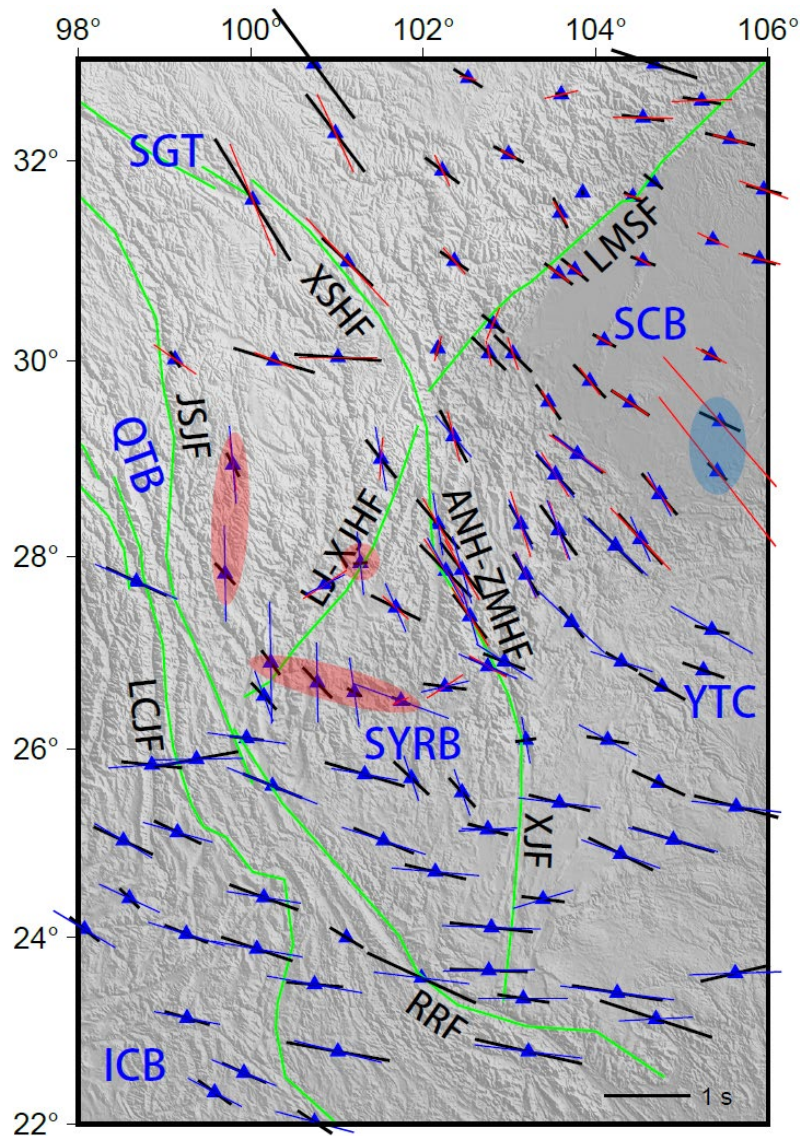386   **4.1 Comparison with previous results**

387   SKS splitting observation has been widely used to investigate the upper mantle anisotropy in the

388   southeastern margin of the Tibetan Plateau (e.g., Lev et al., 2006; Flesch et al., 2005; Wang et al., 2008;

389   Shi et al., 2012; Chang et al., 2015; Yang et al., 2018; Liu et al., 2020; Huang & Chevrot, 2021; Li et

390   al., 2021), with many overlapping seismic stations and teleseismic events. Here, we compare our

391   tomography result at common stations with those of Chang et al. (2015) and Liu et al. (2020) whose

392   SKS splitting measurements are available at the Shear Wave Splitting Product Query website

393   (http://ds.iris.edu/spud/swsmeasurement). In Figure 14, the SKS splitting parameters (splitting times

394   and fast-direction azimuths) predicted by our model in Figure 12 are compared with those from the

395   above two studies.

Figure 13. Result of the recovery test. The recovered and input anisotropic models are compared at five depths marked at the bottom-right corner in each panel. Black and red line segments denote the directions of fast axes in the input and recovery models, respectively, and their lengths indicates the anisotropy strength. Names of major faults and tectonic blocks are the same as in Figure 1. Blue triangles show locations of stations used.

Figure 14 shows that the fast axes determined from our tomographic results are in good agreement with previous studies at most stations. Major differences occur at two stations in the southern tip of the SCB (highlighted by the blue ellipse in Figure 14), where anomalously large splitting times can be seen in the results of Liu et al. (2020), shown by the red line segments. There are also discrepancies in both

406   delay time and fast-axis azimuth at a few stations (highlighted by the red ellipses in Figure 14) in the

407   SYRB where Chang et al. (2015) reported large splitting times and nearly NS fast axes, whereas our

408   model predicts moderate-to-small splitting times and more EW orientation of fast axes. Note that a

409   strictly quantitative comparison of different studies is difficult due to differences in earthquake and

410   window selections, data processing and frequency bands used in the measurement of SKS splitting

411   parameters.

412

413   **Figure 14**. Comparison of SKS splitting times and fast axis directions predicted by our anisotropy

414   model (Figure 12) with previous studies. Black line segments are results from the present study, whereas

415   blue and red line segments show results from Chang et al. (2015) and Liu et al. (2020), respectively.

416   Blue and red ellipses highlight stations where there are large discrepancies in splitting parameters

417   between this study and Liu et al. (2020) and Chang et al. (2015), respectively. Names of major faults

418   and tectonic blocks are the same as in Figure 1.

419   **4.2 Overall variation of shear wave anisotropy**

420   In the shear-wave anisotropy model displayed in Figure 12, we can see that the overall

421   anisotropy strength γ can reach 6% in the lithosphere and asthenosphere under the southeastern

422   margin of the Tibetan Plateau. Both the strength and fast-axis directions of anisotropy show strong

423   lateral and vertical variations. Within the lithosphere (depths of 55 km and 99 km), the anisotropy

424   is stronger in the transition zone between the Tibetan Plateau and YTC (along the LJ-XJHF and

425   LMSF) than other regions, whereas at greater depths in the asthenosphere (e.g. 274 km), the entire

426   region exhibits strong anisotropy with a largely NW-SE orientation of fast axis parallel to the

427   direction of the APM (black arrows in Figure 12), which turns to more E-W direction south of

428   26ºN. At intermediate depths (165 km and 208 km), the anisotropy is highly variable, both in terms

429   of strength and the direction of symmetry axis. Therefore, in the southeastern margin of the

430   Tibetan Plateau, our model shows an apparent decoupling in the overall deformations

431   between the lithosphere and asthenosphere, consistent with previous studies (e.g. Flesch

432   et al., 2005).

433   Previous studies have reported two major features in the SKS splitting pattern in the southeastern

434   margin of the Tibetan Plateau: an overall NW-SE direction of the fast axis and an alignment of the fast

435   axis in nearly EW direction south of ~26ºN latitude (e. g., Lev et al., 2006; Wang et al., 2008; Chang

436   et al., 2015; Huang & Chevrot, 2021), as shown in Figures 6 and 14. Our model suggests that this

437   relatively simple splitting pattern observed at the surface may be a manifestation of vertically averaged

438   complex variation of anisotropy over lithospheric and asthenospheric depths. For instance, along the

439 LMSF, the fast axes in the lithospheric depth (e.g. 55 km and 99 km) are mainly oriented NE-SW with

440 relatively high anisotropy strength, but change to NW-SE in the asthenosphere. As a result, we observe

441 relatively small SKS splitting times (< 0.5 s) with a fast-axis direction of NW-SE at the surface. On the

442 other hand, the moderate SKS splitting times (1 s or less) and the alignments of nearly EW orientation

443 of symmetry axes observed at the surface are resulted from a discordant anisotropy in the lithosphere

444 and a nearly uniform EW-oriented anisotropy in the asthenosphere.

445 **4.3 The Songpan-Ganzi Terrane**

446 The SGT is the central portion of the Tibetan Plateau and has been elevated by the collision

447 between the Indian and Eurasian plates. In its eastern part the eastward expansion of the terrane

448 has been blocked by the SCB of the YTC. In our study region, the SGT occupies an area of

449 inverted-triangle shape in the north bounded by the JSJF in the southwest and LMSF and LJ-XJHF

450 in the southeast (Li et al., 2021). Our model shows two distinct types of anisotropy. In the area far

451 away from the LMSF, the anisotropy is moderate to strong (3–6%) with NW-SE oriented fast axes

452 in both lithosphere and asthenosphere, parallel to the regional APM direction (black arrows in

453 Figure 12) and asthenospheric flow, suggesting a vertical coupling of deformation there and in

454 agreement with Flesch et al. (2005). The NW-SE orientation of anisotropy in the SGT is

455 consistent with previous tomography results from Rayleigh waves (Bao et al., 2020; Legendre et al.,

456 2015) and Pn waves (Lei et al., 2014). However, in the area near the LMSF, the fast axis of

457 anisotropy in the lithosphere (e.g. 55 km and 99 km depths) becomes NE-SW, parallel to the

458 proposed lithospheric material flow as a result of the resistance of the SCB to the eastward

459 expansion of the Tibetan Plateau at LMSF. Near the LMSF, the lithospheric material of the SGT

460 appears to come apart at ~102° longitude, going in the opposite NE and SW directions. In the

461 asthenosphere, the fast axis of anisotropy returns to NW-SE, consistent with the regional APM

462   direction. The relatively sharp turn of the fast axis of the lithospheric anisotropy from SE-NW to

463   NE-SW in the southern tip of SGT is a clear evidence for the redirection of the lithospheric flow

464   from eastward to southward in the southeastern margin of the Tibetan Plateau.

465   **4.4 The Yangtze Craton**

466   The YTC is a Precambrian continental block which was accreted to the North China Craton in the

467   Triassic. Our study region covers the western margin of the YTC, namely the SCB and SYRB, and

468   the model in Figure 12 shows that the anisotropy in the region varies significantly both horizontally

469   and vertically, as a result of the complex geodynamic evolution of the YTC involving multiple

470   rounds of lithospheric reactivation, such as the Permian-Triassic Emeishan flood basalt eruption

471   (e.g. Xu et al., 2001), as well as interactions with surrounding tectonic blocks. In our anisotropy

472   model, the SCB exhibits a moderate anisotropy with a NE-SW orientation near the LMSF at shallow

473   depths (e.g. 55 km and 99 km), presumably the effect of dominant shearing in the vicinity of the

474   LMSF by the moving SGT lithosphere in NE and SW directions. Further east, EW compression

475   gradually takes over NE-SW shear at shallow depths, and the fast axis of anisotropy turns to more

476   EW (e.g. 55 km, 99 km and 165 km). This turn of anisotropy from NE-SW to more EW away from

477   the LMSF has also been observed in surface-wave studies (e.g. Zhang et al., 2023). At greater

478   depth in the lithosphere (208 km in Figure 12), the anisotropy under the SCB becomes nearly NS,

479   which is consistent with a frozen anisotropy in the lithosphere generated by the mantle flow in the

480   Cenozoic (Li et al., 2021) without being modified by the SGT-SCB block interaction at shallower

481   depths. At asthenospheric depth (274 km), the anisotropy is largely aligned with the regional APM.

482   The anisotropy under the SYRB appears to be continuous across the ANH-ZMHF and XJF,

483   suggesting that both fault systems are crustal boundaries where the SYRB is escaping in the

484   southeast direction. In the lithosphere (55 km and 99 km under SYRB and above 208 km depth

485   east of ANH-ZMHF between the SCB and 26ºN), the anisotropy has a complex pattern of

486   relatively small-scale horizontal variations of fast-axis orientation, perhaps a result of multiple

487   phases of lithospheric reactivations that have modified the previously frozen anisotropy. In the

488   asthenosphere (> 100 km depth in SYRB and > 200 km between the SCB and 26ºN), the anisotropy

489   largely follows the direction of the regional APM or mantle flow. In the 208-km depth plot of the

490   model in Figure 12, the azimuthal anisotropy south of the SCB is very weak, which may indicate

491   a more complex local mantle flow pattern due to the regionally predominant NW-SE mantle flow

492   being disturbed by the root of the YTC lithosphere. South of 26ºN, the anisotropy under the YTC

493   is returns to largely parallel to the direction of APM.

494   **4.5 Anisotropy south of 26ºN latitude**

495   All SKS splitting studies in the southeastern margin of the Tibetan Plateau have shown the that the

496   SKS splitting south of 26ºN latitude appears to be consistently oriented in the EW direction. Our

497   model suggests that this apparently simple pattern is resulted predominantly from strong EW

498   oriented azimuthal anisotropy generated by the EW asthenosphere flow due to the eastward

499   subduction of the Indian Plate under Myanmar (e.g. Yang et al., 2022), and regional variation of

500   lithospheric and asthenospheric contributions to anisotropy leads small but discernable differences

501   in SKS splitting observations. For example, under the SYRB, the anisotropy in the lithosphere

502   between 24ºN and 26ºN is relatively strong (55 km and 99 km in Figure 12) with different

503   orientations of fast axes. The integration of lithospheric and asthenospheric anisotropy results in

504   horizontally variable SKS splitting delay times and fast-axis directions observed at the surface, as

505   shown by the stations in SYRB in Figures 6 and 14. In the rest of the study region south of 26ºN,

506   the asthenospheric contribution dominates, and the surface SKS splitting parameters exhibit

507   relatively uniform EW fast axes.

508 **5 Conclusions**

509 In this study, we have carried out a fullwave multiscale tomography to obtain the 3D model for

510 the shear-wave anisotropy in the southeastern margin of the Tibetan Plateau. A total of 5,216 high-

511 quality SKS splitting intensities are obtained from the broadband records of 470 teleseismic events

512 at 111 permanent stations after a series of quality control measures. In conjunction with the 3D

513 sensitivity kernels and a wavelet-based parameterization, this dataset is inverted to achieve a data-

514 driven multi-scale resolution to anisotropy structure in the upper mantle.

515   The vertical variation of the anisotropy in our result indicates that the lithospheric and

516 asthenospheric deformations are decoupled in the southeastern margin of the Tibetan Plateau. On

517 the other hand, the anisotropy appears to be vertically consistent under the Songpan-Ganzi Terrane,

518 suggesting a coupling of the deformations in the lithosphere and asthenosphere in the interior of

519 the Tibetan Plateau.

520   The strength of anisotropy in our model is spatially variable and can reach 6%, with strongest

521 anisotropy in the asthenosphere due to large-scale and relatively steady mantle flow, and in the

522 lithosphere along the Longmenshan Fault and Lijiang-Xiaojinhe Fault, presumably due to large

523 shearing effect generated by the relative movement between the Songpan-Ganzi Terrane and the

524 Yangtze Craton.

525   The azimuth of the fast axis of anisotropy in the asthenosphere largely follows the direction of

526 regional absolute plate motion or mantle flow, i.e. mostly SE beneath the Songpan-Ganzi Terrane and

527 the Yangtze Craton and nearly east-west south of 26ºN latitude. In the lithosphere, however, the fast

528 axis is highly variable. In the Sichuan Basin, the frozen anisotropy dominates in the deep lithosphere;

529 whereas at shallower depths, the anisotropy is modified by the interaction with the Songpan-Ganzi

530 Terrane into SW in the vicinity of the Longmenshan Fault and nearly EW further east. In the Sichuan-

531   Yunnan Rhombic Block and east of the Anninghe-Zemuhe Fault, the azimuth of the fast axis of

532   anisotropy exhibits complex spatial pattern due to multiple phases of lithospheric reactivation. The

533   vertical integration of the contributions from complex lithospheric anisotropy and relatively uniform

534   asthenospheric anisotropy gives rise to the seemingly simple pattern of conventional SKS splitting

535   parameters observed at the surface. Our 3D model of azimuthal anisotropy provides important new

536   insights into the lithospheric and asthenospheric dynamics in the southeastern margin of the

537   Tibetan Plateau.

538

539

544

545

Data Availability Statement

547   The processed SKS waveforms and their corresponding splitting intensities as well as the final

548   inverted anisotropic model can be accessed at https://doi.org/10.5281/zenodo.8232748. Most of

549   the figures are generated using the Generic Mapping Tools (Wessel et al., 2019,

550   https://www.generic-mapping-tools.org).

551

552

553

554 **References**

555 Argus, D. F., Gordon, R. G., & DeMets, C. (2011). Geologically current motion of 56 plates
556   relative to the no-net-rotation reference frame. *Geochemistry, Geophysics, Geosystems*,
557   *12*(11). doi: 10.1029/2011GC003751

558 Bao, X., Song, X., Eaton, D. W., Xu, Y., & Chen, H. (2020). Episodic lithospheric deformation in
559   eastern Tibet inferred from seismic anisotropy. *Geophysical Research Letters*, 47(3). doi:
560   10.1029/2019gl085721

561 Becker, T. W., Chevrot, S., Schulte-Pelkum, V., & Blackman, D. K. (2006). Statistical properties
562   of seismic anisotropy predicted by upper mantle geodynamic models. *Journal of Geophysical*
563   *Research: Solid Earth*, 111(B8). doi: 10.1029/2005JB004095

564 Cai, Y., Wu, J., Fang, L., Wang, W., & Yi, S. (2016). Crustal anisotropy and deformation of the
565   southeastern margin of the Tibetan Plateau revealed by Pms splitting. *Journal of Asian Earth*
566   *Sciences*, 121, 120–126. doi: 10.1016/j.jseaes.2016.02.005

567 Chang, L.-J., Ding, Z.-F., & Wang, C.-Y. (2015). Upper mantle anisotropy beneath the southern
568   segment of north-south tectonic belt, China. *Chinese Journal of Geophysics (in Chinese)*,
569   58(11), 4052–4067. doi: 10.6038/cjg20151114

570 Chevrot, S. (2000). Multichannel analysis of shear wave splitting. *Journal of Geophysical*
571   *Research: Solid Earth*, 105(B9), 21579–21590. doi: 10.1029/2000JB900199

572 Chevrot, S. (2006). Finite-frequency vectorial tomography: a new method for high-resolution
573   imaging of upper mantle anisotropy. *Geophysical Journal International*, 165(2), 641–657.
574   doi: 10.1111/j.1365-246X.2006.02982.x

575 Chiao, L. Y., & Kuo, B. Y. (2001). Multiscale seismic tomography. *Geophysical Journal*
576   *International*, 145(2), 517-527. doi: 10.1046/j.0956-540x.2001.01403.x

577 Dahlen, F., Hung, S.-H., & Nolet, G. (2000). Fréchet kernels for finite-frequency travel- times—
578   I. Theory. *Geophysical Journal International*, 141(1), 157-174. doi: 10.1046/j.1365-
579   246X.2000.00070.x

580 Dziewonski, A. M., & Anderson, D. L. (1981). Preliminary reference Earth model, *Physics of the*
581   *Earth and Planetary Interior,* 25**,** 297–356.

582 Favier, N., & Chevrot, S. (2003). Sensitivity kernels for shear wave splitting in transverse isotropic
583   media. *Geophysical Journal International*, 153(1), 213–228. doi: 10.1046/j.1365-
584   246X.2003.01894.x

585 Flesch, L. M., Holt, W. E., Silver, P. G., Stephenson, M., Wang, C.-Y., & Chan, W. W. (2005).
586   Constraining the extent of crust–mantle coupling in central Asia using GPS, geologic, and
587   shear wave splitting data. *Earth and Planetary Science Letters*, 238(1-2), 248-268. doi:
588   10.1016/j.epsl.2005.06.023

589 Han, C., Xu, M., Huang, Z., Wang, L., Xu, M., Mi, N., Yu, D., Guo, T., Wang, H., Hao, S., Tia,
590   M., & Bi, Y. (2020). Layered crustal anisotropy and deformation in the SE Tibetan Plateau
591   revealed by Markov- Chain-Monte-Carlo inversion of receiver functions. *Physics of the Earth*
592   *and Planetary Interiors*, 306 , 106522. doi: 10.1016/j.pepi.2020.106522

593 Hu, J., Su, Y., Zhu, X., & Chen, Y. (2005). S-wave velocity and Poisson's ratio structure of crust
594   in Yunnan and its implication. *Science in China Series D: Earth Sciences*, 48(2), 210–218.
595   doi: 10.1360/03yd0062

596 Huang, J., Zhao, D., & Zheng, S. (2002). Lithospheric structure and its relationship to seismic and
597   volcanic activity in southwest China. *Journal of Geophysical Research: Solid Earth*,
598   107(B10), ESE–13. doi: 10.1029/2000JB000137

599 Huang, P., Gao, Y., & Xue, B. (2022). Advances in the deep tectonics and seismic anisotropy of
600   the Lijiang-Xiaojinhe fault zone in the Sichuan-Yunnan block, southwestern China.
601   *Earthquake Research Advances*, 2(1), 100116. doi: 10.1016/j.eqrea.2022.100116

602 Huang, R., Wang, Z., Pei, S., & Wang, Y. (2009). Crustal ductile flow and its contribution to
603   tectonic stress in Southwest China. *Tectonophysics*, 473(3-4), 476–489. doi: 10.1016/
604   j.tecto.2009.04.001

605 Huang, Z., & Chevrot, S. (2021). Mantle dynamics in the SE Tibetan Plateau revealed by
606   teleseismic shear-wave splitting analysis. *Physics of the Earth and Planetary Interiors*, 313,
607   106687. doi: 10.1016/j.pepi.2021.106687

608 Huang, Z., Wang, L., Xu, M., & Zhao, D. (2018). P wave anisotropic tomography of the SE
609   Tibetan Plateau: Evidence for the crustal and upper-mantle deformations. *Journal of*
610   *Geophysical Research: Solid Earth*, 123(10), 8957–8978. doi: 10.1029/2018JB016048

611 Huang, Z., Zhao, D., & Wang, L. (2015). P wave tomography and anisotropy beneath Southeast
612   Asia: Insight into mantle dynamics. *Journal of Geophysical Research: Solid Earth*, 120(7),
613   5154–5174. doi: 10.1002/2015JB012098

614 Hung, S. H., Chen, W. P., & Chiao, L. Y. (2011). A data-adaptive, multiscale approach of finite-
615   frequency, traveltime tomography with special reference to P and S wave data from central

616   Tibet. *Journal of Geophysical Research: Solid Earth*, 116. doi: 10.1029/2010JB008190

617   Kind, R., Yuan, X., Saul, J., Nelson, D., Sobolev, S., Mechie, J., Zhao, W., Kosarev, G., Ni, J.,
618   Achauer, U., & Jiang, M. (2002). Seismic images of crust and upper mantle beneath Tibet:
619   Evidence for Eurasian plate subduction. *Science*, 298(5596), 1219–1221. doi:
620   10.1126/science.1078115

621   Legendre, C. P., Deschamps, F., Zhao, L., & Chen, Q.-F. (2015). Rayleigh-wave dispersion reveals
622   crust-mantle decoupling beneath eastern Tibet. *Scientific Reports*, 5(1), 1–7. doi:
623   10.1038/srep16644

624   Lei, J., Li, Y., Xie, F., Teng, J., Zhang, G., Sun, C., & Zha, X. (2014). Pn anisotropic tomography
625   and dynamics under eastern Tibetan Plateau. *Journal of Geophysical Research: Solid Earth*,
626   119(3), 2174–2198. doi: 10.1002/2013JB010847

627   Lev, E., Long, M. D., & van der Hilst, R. D. (2006). Seismic anisotropy in Eastern Tibet from
628   shear wave splitting reveals changes in lithospheric deformation. *Earth and Planetary*
629   *Science Letters*, 251(3-4), 293-304. doi: 10.1016/j.epsl.2006.09.018

630   Li, H., Su, W., Wang, C.-Y., & Huang, Z. (2009). Ambient noise Rayleigh wave tomography in
631   western Sichuan and eastern Tibet. *Earth and Planetary Science Letters*, 282(1-4), 201–211.
632   doi: 10.1016/j.epsl.2009.03.021

633   Li, W., Chen, Y., Liang, X., & Xu, Y.-G. (2021). Lateral seismic anisotropy variations record
634   interaction between Tibetan mantle flow and plume-strengthened Yangtze Craton. *Journal of*
635   *Geophysical Research: Solid Earth*, 126, e2020JB020841.
636   https://doi.org/10.1029/2020JB020841

637   Lin, Y.-P., Zhao, L., & Hung, S.-H. (2014a). Full-wave effects on shear wave splitting,
638   *Geophysical Research Letters*, 41(3), 799–804. doi: 10.1002/2013GL058742

639   Lin, Y.-P., Zhao, L., & Hung, S.-H. (2014b). Full-wave multiscale anisotropy tomography in
640   Southern California. *Geophysical Research Letters*, 41(24), 8809–8817. doi: 10.1002/
641   2014GL061855

642   Link, F., Reiss, M. C., & Rümpker, G. (2022). An automatized XKS-splitting procedure for large
643   data sets: Extension package for SplitRacer and application to the USArray. *Computers &*
644   *Geosciences*, 158, 104961. doi: 10.1016/j.cageo.2021.104961

645   Liu, J., Wu, J., Wang, W., Fang, L., & Chang, K. (2020). Seismic anisotropy beneath the eastern
646   margin of the Tibetan Plateau from SKS splitting observations. *Tectonophysics*, 785, 228430.

doi: 10.1016/j.tecto.2020.228430

Liu, Q. Y., van Der Hilst, R. D., Li, Y., Yao, H. J., Chen, J. H., Guo, B., Qi, S. H., Wang, J., Huang, H., & Li, S. C. (2014). Eastward expansion of the Tibetan Plateau by crustal flow and strain partitioning across faults. *Nature Geoscience*, 7(5), 361–365. doi: 10.1038/NGEO2130

Long, M. D., & Becker, T. W. (2010). Mantle dynamics and seismic anisotropy. *Earth and Planetary Science Letters,* 297(3-4), 341–354.

Mondal, P., & Long, M. D. (2019). A model space search approach to finite-frequency SKS splitting intensity tomography in a reduced parameter space. *Geophysical Journal International*, 217, 238-256. doi: 10.1093/gji/ggz016

Mondal, P., & Long, M. D. (2020). Strong seismic anisotropy in the deep upper mantle beneath the Cascadia backarc: Constraints from probabilistic finite-frequency SKS splitting intensity tomography. *Earth and Planetary Science Letters*, 539, 116172. doi: 10.1016/j.epsl.2020.116172

Monteiller, V., & Chevrot, S. (2011). High-resolution imaging of the deep anisotropic structure of the San Andreas Fault system beneath southern California. *Geophysical Journal International*, 186(2), 418-446. doi: 10.1111/j.1365-246X.2011.05082.x

Paige, C. C., & Saunders, M. A. (1982). LSQR–an algorithm for sparse linear-equations and sparse least-squares. *ACM Transactions on Mathematical Software*, 8(1), 43–71.

Pasyanos, M. E., Masters, T. G., Laske, G., & Ma, Z. (2014). LITHO1. 0: An updated crust and lithospheric model of the Earth. *Journal of Geophysical Research: Solid Earth*, 119(3), 2153–2173. doi: 10.1002/2013JB010626

Quatieri, T. F. (2006). *Discrete-time Speech Signal Processing: Principles and Practice*. Pearson Education India.

Royden, L. H., Burchfiel, B. C., & van der Hilst, R. D. (2008). The geological evolution of the Tibetan Plateau. *Science*, 321(5892), 1054–1058. doi: 10.1126/science.1155371

Shen, Z.-K., Lü, J., Wang, M., & Bürgmann, R. (2005). Contemporary crustal deformation around the southeast borderland of the Tibetan Plateau. *Journal of Geophysical Research: Solid Earth*, 110(B11). doi: 10.1029/2004JB003421

Shi, Y., Gao, Y., Su, Y., & Wang, Q. (2012). Shear-wave splitting beneath Yunnan area of Southwest China. *Earthquake Science*, 25(1), 25–34. doi: 10.1007/s11589-012-0828-4

Sieminski, A., Paulssen, H., Trampert, J., & Tromp, J. (2008). Finite-frequency SKS splitting:

678   measurement and sensitivity kernels. *Bulletin of the Seismological Society of America*, 98(4),
679   1797–1810. doi: 10.1785/0120070297

680   Sun, Y., Niu, F., Liu, H., Chen, Y., & Liu, J. (2012). Crustal structure and deformation of the SE
681   Tibetan plateau revealed by receiver function data. *Earth and Planetary Science Letters*, 349,
682   186-197. doi: 10.1016/j.epsl.2012.07.007

683   Wang, C.-Y., Chan, W. W., & Mooney, W. D. (2003). Three-dimensional velocity structure of
684   crust and upper mantle in southwestern China and its tectonic implications. *Journal of*
685   *Geophysical Research: Solid Earth*, *108*(B9). doi: 10.1029/2002JB001973

686   Wang, C.-Y., Flesch, L. M., Silver, P. G., Chang, L.-J., & Chan, W. W. (2008). Evidence for
687   mechanically coupled lithosphere in central Asia and resulting implications. *Geology*, 36(5),
688   363–366. doi: 10.1130/G24450A.1

689   Wang, C.-Y., Lou, H., Silver, P. G., Zhu, L., & Chang, L. (2010). Crustal structure variation along
690   30°N in the eastern Tibetan Plateau and its tectonic implications. *Earth and Planetary Science*
691   *Letters*, 289(3-4), 367–376. doi: 10.1016/j.epsl.2009.11.026

692   Wang, M., & Shen, Z.-K. (2020). Present-day crustal deformation of continental China derived
693   from GPS and its tectonic implications. *Journal of Geophysical Research: Solid Earth*, 125(2),
694   e2019JB018774. doi: 10.1029/2019JB018774

695   Wang, W., Wu, J., Fang, L., Lai, G., & Cai, Y. (2017). Crustal thickness and Poisson's ratio in
696   southwest China based on data from dense seismic arrays. *Journal of Geophysical Research:*
697   *Solid Earth*, 122(9), 7219–7235. doi: 10.1002/2017JB013978

698   Wei, W., Xu, J., Zhao, D., & Shi, Y. (2012). East Asia mantle tomography: New insight into plate
699   subduction and intraplate volcanism. *Journal of Asian Earth Sciences*, 60, 88–103. doi:
700   10.1016/j.jseaes.2012.08.001

701   Wei, Z., & Zhao, L. (2019). Lg-Q model and its implication on high-frequency ground motion for
702   earthquakes in the Sichuan and Yunnan region. *Earth and Planetary Physics*, 3(6), 526–536.
703   doi: 10.26464/epp2019054

704   Wei, Z., & Zhao, L. (2022). P-wave velocity structure of the lower crust and uppermost mantle
705   beneath the Sichuan-Yunnan (China) region. *Seismological Research Letters*, 93(4). doi:
706   10.1785/0220210357

707   Wessel, P., Luis, J., Uieda, L., Scharroo, R., Wobbe, F., Smith, W. H., & Tian, D. (2019). The
708   generic mapping tools version 6. *Geochemistry, Geophysics, Geosystems*, 20(11), 5556–5564.

709   doi: 10.1029/2019GC008515

710   Xu, L., Rondenay, S., & van der Hilst, R. D. (2007). Structure of the crust beneath the southeastern

711   Tibetan Plateau from teleseismic receiver functions. *Physics of the Earth and Planetary*

712   *Interiors*, 165(3-4), 176–193. doi: 10.1016/j.pepi.2007.09.002

713   Xu, M., Huang, Z., Wang, L., Xu, M., Zhang, Y., Mi, N., Yu, D., & Yuan, X. (2020). Sharp lateral

714   Moho variations across the SE Tibetan margin and their implications for plateau growth.

715   *Journal of Geophysical Research: Solid Earth*, 125(5), e2019JB018117. doi:

716   10.1029/2019JB018117

717   Xu, Y., Chung, S.-L., Jahn, B.-m., & Wu, G. (2001). Petrologic and geochemical constraints on

718   the petrogenesis of Permian–Triassic Emeishan flood basalts in southwestern China. *Lithos*,

719   58, 145–168.

720   Yang, S., Liang, X., Jiang, M., Chen, L., He, Y., Mon, C. T., Hou, G., Thant, M., Sein, K., & Wan,

721   B. (2022). Slab remnants beneath the Myanmar terrane evidencing double subduction of the

722   Neo-Tethyan Ocean. *Science Advances*, 8(34), eabo1027. doi: 10.1126/sciadv.abo1027

723   Yang, Y., Liang, C., Fang, L., Su, J., & Hua, Q. (2018). A comprehensive analysis on the stress

724   field and seismic anisotropy in eastern Tibet. *Tectonics*, 37(6), 1648–1657. doi:

725   10.1029/2018TC005011

726   Yang, Y., Yao, H., Wu, H., Zhang, P., & Wang, M. (2019). A new crustal shear-velocity model in

727   Southwest China from joint seismological inversion and its implications for regional crustal

728   dynamics. *Geophysical Journal International*, 220, 1379–1393.

729   https://doi.org/10.1093/gji/ggz514

730   Yang, Y., Zheng, Y., Chen, J., Zhou, S., Celyan, S., Sandvol, E., Tilmann, F., Priestley, K., Hearn,

731   T. M., Ni, J. F., Brown, L. D., & Ritzwoller, M. H. (2010). Rayleigh wave phase velocity

732   maps of Tibet and the surrounding regions from ambient seismic noise tomography.

733   *Geochemistry, Geophysics, Geosystems*, 11(8). doi:10.1029/2010GC003119

734   Yao, H. J., van der Hilst, R. D., & Montagner, J. P. (2010). Heterogeneity and anisotropy of the

735   lithosphere of SE Tibet from surface wave array tomography. *Journal of Geophysical*

736   *Research: Solid Earth*, 115. doi: 10.1029/2009JB007142

737   Yin, A., & Harrison, T. M. (2000). Geologic evolution of the Himalayan-Tibetan orogen. *Annual*

738   *Review of Earth and Planetary Sciences*, 28(1), 211–280.

739   Zhang, F., Wu, Q., Li, Y., Zhang, R., Sun, L., Pan, J., & Ding, Z. (2018). Seismic tomography of

740   eastern Tibet: Implications for the Tibetan Plateau growth. *Tectonics*, 37(9), 2833–2847. doi:
741   10.1029/2018TC004977

742 Zhang, G. W., Guo, A. L., Wang, Y. J., Li, S. Z., Dong, Y. P., Liu, S. F., He, D. F., Cheng, S. Y.,
743   Lu, R. K., & Yao, A. P. (2013). Tectonics of South China Continent and its implications.
744   *Science China Earth Sciences*, 56, 1804–1828. doi: 10.1007/s11430-013-4679-1

745 Zhang, P., Deng, Q., Zhang, G., Ma, J., Gan, W., Min, W., Mao, F., & Wang, Q. (2003). Active
746   tectonic blocks and strong earthquakes in the continent of China. *Science China Earth*
747   *Sciences*, 46(2), 13–24. doi: 10.1360/03dz0002

748 Zhang, P.-Z. (2013). A review on active tectonics and deep crustal processes of the western
749   Sichuan region, eastern margin of the Tibetan Plateau. *Tectonophysics*, 584, 7–22. doi:
750   10.1016/j.tecto.2012.02.021

751 Zhang, Z., Wang, Y., Chen, Y., Houseman, G. A., Tian, X., Wang, E., & Teng, J. (2009). Crustal
752   structure across Longmenshan fault belt from passive source seismic profiling. *Geophysical*
753   *Research Letters*, 36(17). doi: 10.1029/2009GL039580

754 Zhang, Z., Yao, H., & Yang, Y. (2020). Shear wave velocity structure of the crust and upper mantle
755   in Southeastern Tibet and its geodynamic implications. *Science China Earth Sciences*, 63,
756   1278–1293. https://doi.org/10.1007/s11430-020-9625-3

757 Zhang, Z., Feng, J., & Yao, H. (2023). 3-D azimuthal anisotropy structure reveals different
758   deformation modes of the crust and upper mantle in the southeastern Tibetan Plateau.
759   *Frontiers in Earth Science*, 11, 1095609. doi: 10.3389/feart.2023.1095609

760 Zhao, G., Unsworth, M. J., Zhan, Y., Wang, L., Chen, X., Jones, A. G., Tang, J., Xiao, Q., Wang,
761   J., Cai, J., Li, T., Wang, Y., & Zhang, J. (2012). Crustal structure and rheology of the
762   Longmenshan and Wenchuan Mw 7.9 earthquake epicentral area from magnetotelluric data.
763   *Geology*, 40(12), 1139–1142. doi: 10.1130/ G33703.1

764 Zhao, L., & Chevrot, S. (2011). An efficient and flexible approach to the calculation of three-
765   dimensional full-wave fréchet kernels for seismic tomography—II. Numerical results.
766   *Geophysical Journal International*, 185(2), 939–954. doi: 10.1111/j.1365-
767   246X.2011.04984.x

768 Zhao, L., Jordan, T. H., & Chapman, C. H. (2000). Three-dimensional Fréchet differential kernels
769   for seismic delay times**,** *Geophysical Journal International*, 141(3), 558–576. doi:
770   10.1046/j.1365-246x.2000.00085.x

771   Zhao, L. F., Xie, X. B., He, J. K., Tian, X., & Yao, Z. X. (2013). Crustal flow pattern beneath the

772   Tibetan Plateau constrained by regional Lg-wave Q tomography. *Earth and Planetary*

773   *Science Letters*, 383, 113–122. doi: 10.1016/j.epsl.2013.09.038.

1 *Manuscript submitted to Journal of Geophysical Research: Solid Earth*

2 **Supporting Information for**

3 **Upper-mantle anisotropy in the southeastern margin of the Tibetan Plateau revealed by**
4 **fullwave SKS splitting intensity tomography**

5 Yi Lin[1,2] and Li Zhao[1,3*]

6 [1] *School of Earth and Space Sciences, Peking University, Beijing 100871, China.*

7 [2] *Key Laboratory of Earth Exploration and Information Techniques of the China Ministry of*

8 *Education, Chengdu University of Technology, Chengdu 610059, China.*

9 [3] *Hebei Hongshan National Geophysical Observatory, Peking University, Beijing 100871, China.*

10 * Corresponding author: Li Zhao (lizhaopku@pku.edu.cn)

11

12 **This Supporting Information contains 8 Supplementary Figures S1-S8.**

13 **Figure S1**: Resolution test results at different depths for the azimuth of symmetry axis
14 using 1º x 1º checkerboard and different damping factors.

15 **Figure S2**: Resolution test results at different depths for anisotropy strength using 1º x 1º
16 checkerboard and different damping factors.

17 **Figure S3**: Resolution test results at different depths for the azimuth of symmetry axis
18 using 1.5º x 1.5º checkerboard and different damping factors.

19 **Figure S4**: Resolution test results at different depths for anisotropy strength using 1.5º x
20 1.5º checkerboard and different damping factors.

21 **Figure S5**: Resolution tests for the azimuth of symmetry axis using a 2-layer input model
22 and different damping factors.

23 **Figure S6**: Resolution tests for anisotropy strength using a 2-layer input model and
24 different damping factors.

25 **Figure S7**: Resolution tests for the azimuth of symmetry axis using a 4-layer input model
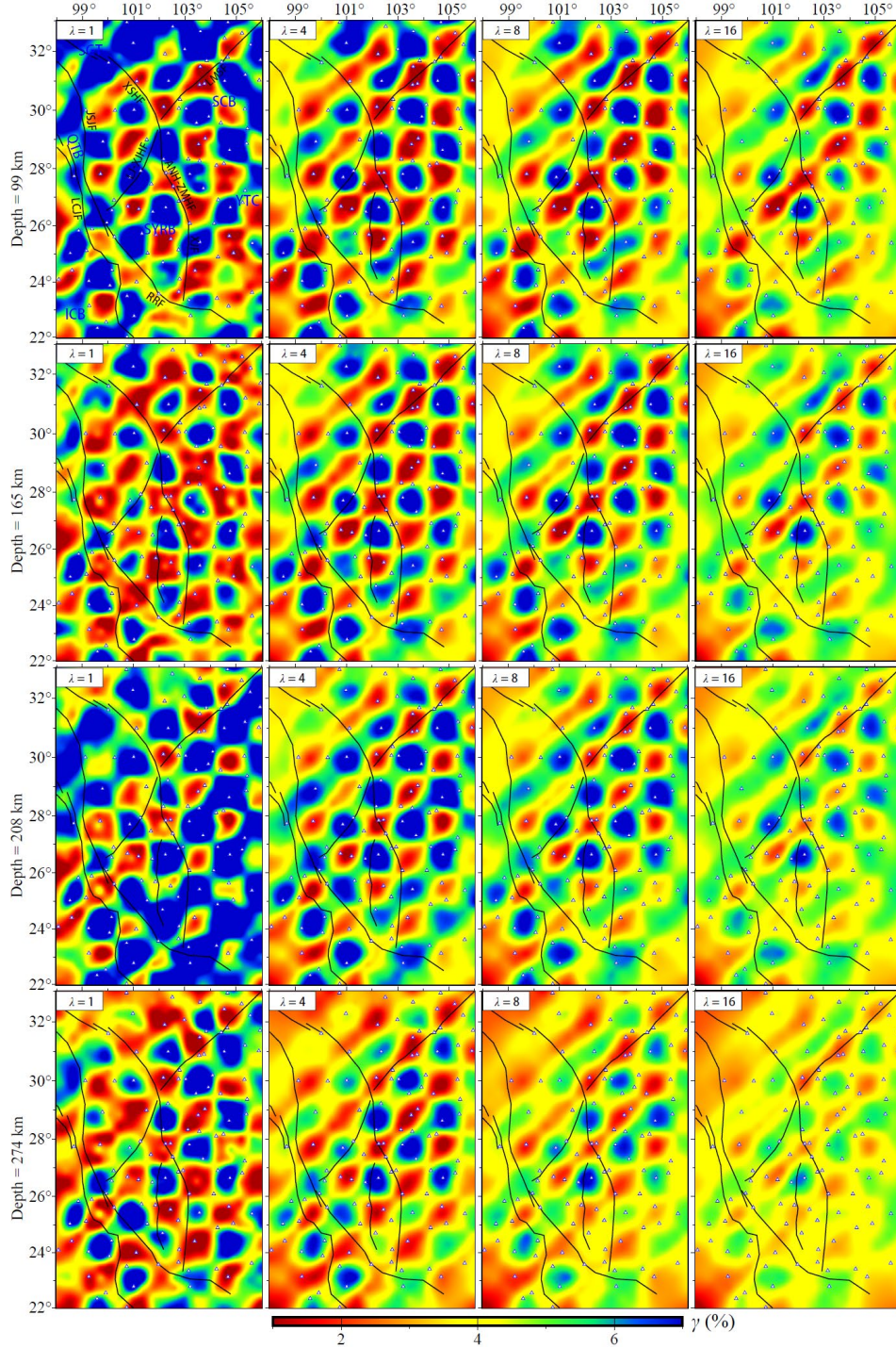26 and different damping factors.

27 **Figure S8**: Resolution tests for anisotropy strength using a 4-layer input model and
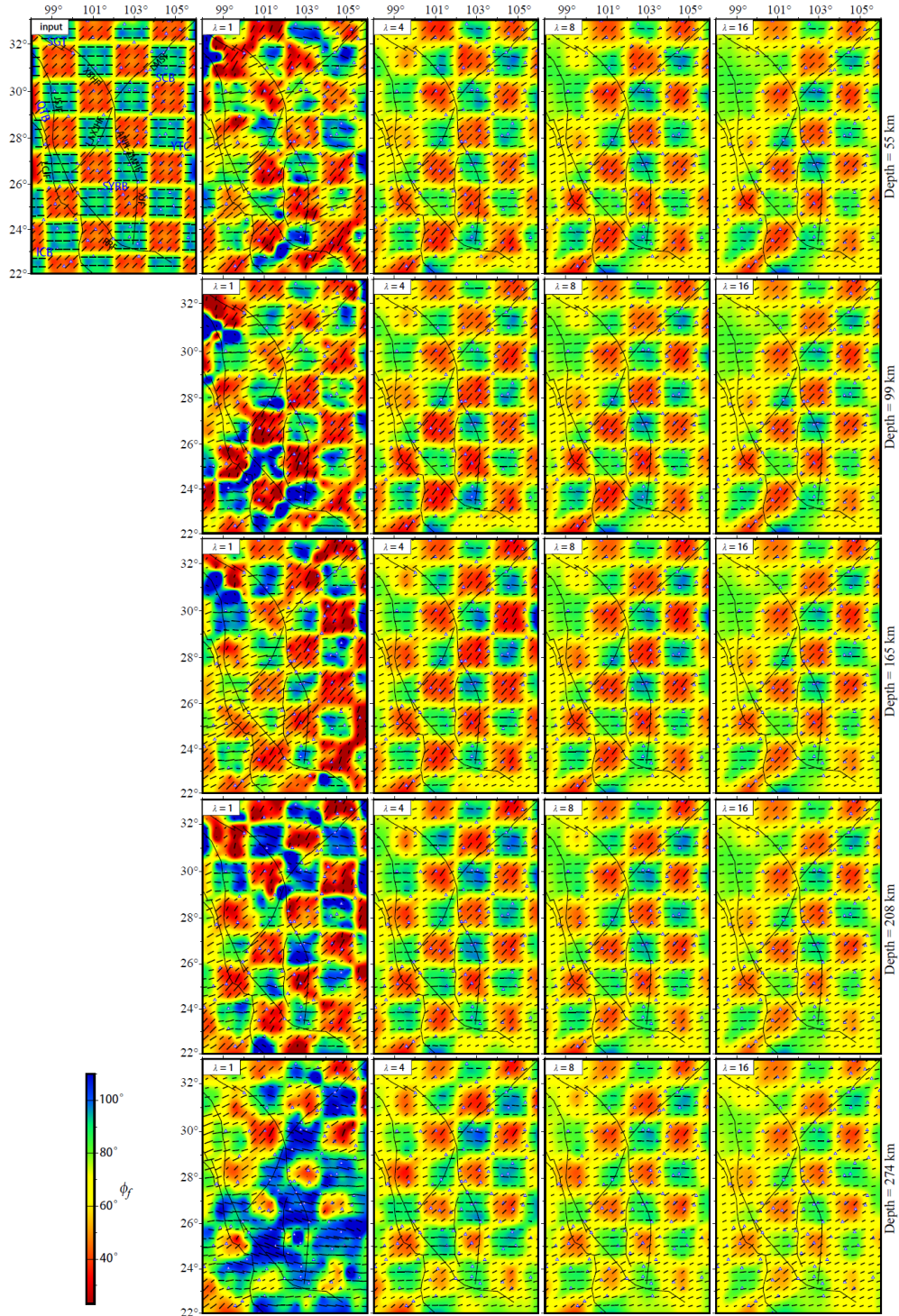28 different damping factors.

Supplementary Figures

31 **Figure S1**. Resolution tests for the azimuth of symmetry axis using 1° x 1° checkerboard.
32 The input model (top-left panel of Figure 8) has horizontally alternating azimuthal angles
33 of fast axes $\phi_f = 90°$ and $\phi_f = 45°$ shown by both the color and the directions of the line
34 segments, and a fixed anisotropy strength $\gamma = 4\%$ represented by the lengths of the line
35 segments. Shown here are recovered models using different damping factors (left to right)
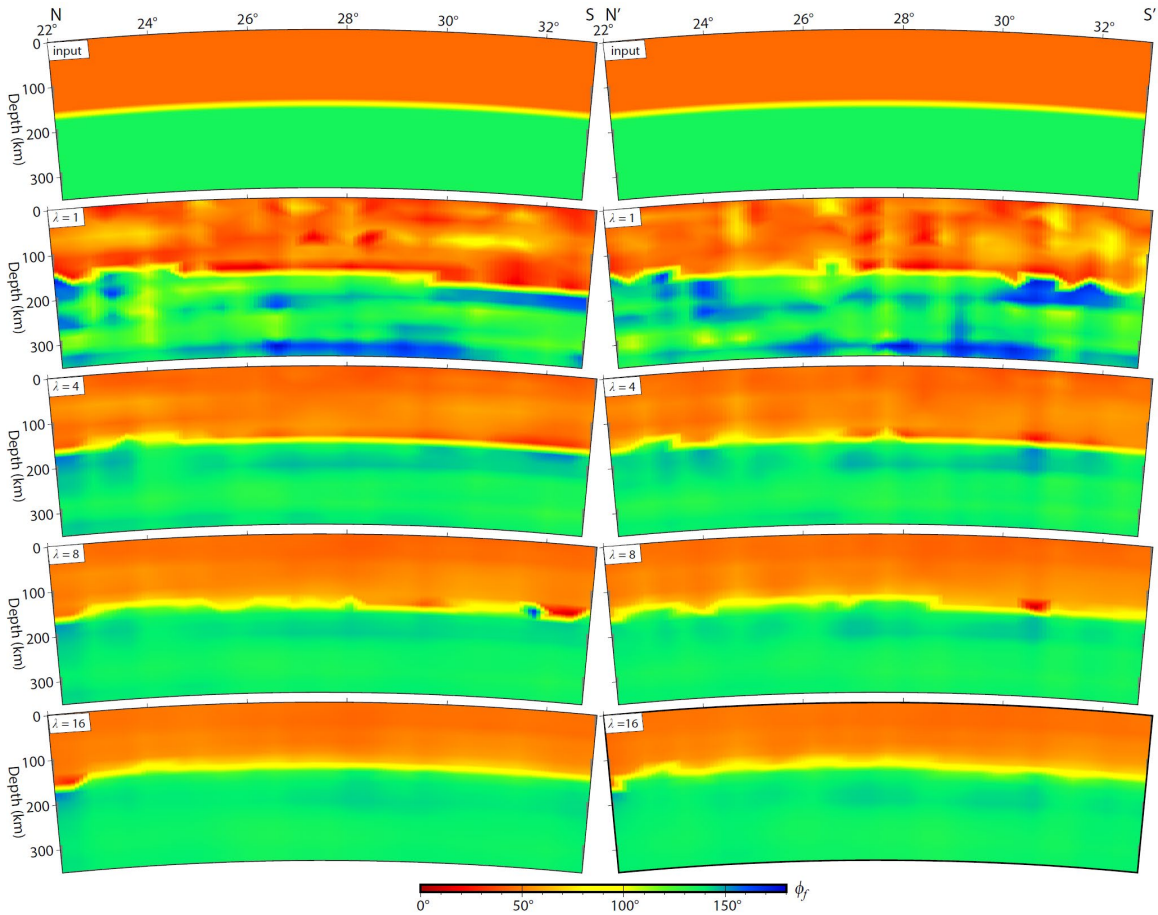36 at different depths (top to bottom).

1

Figure S2. Resolution tests for anisotropy strength using 1° x 1° checkerboard. The input model (top-left panel of Figure 8) has horizontally alternating anisotropy strengths shown by the colors representing perturbations of $\delta\gamma = \pm 0.03$ relative to a background anisotropy strength of $\gamma = 0.04$ and a fixed azimuthal angle of symmetry axis $\phi_f = 22.5°$. Shown here are recovered models using different damping factors (left to right) at different depths (top to bottom).

2

44

Figure S3. Resolution tests for the azimuth of symmetry axis using 1.5º x 1.5º checkerboard. The input model (top-left panel) has horizontally alternating azimuthal angles of fast axes $\phi_f = 90^{\circ}$ and $\phi_f = 45^{\circ}$ shown by both the color and the directions of the line segments, and a fixed anisotropy strength $\gamma = 4\%$ represented by the lengths of the line segments. The rest of the panels show recovered models using different damping factors (left to right) at different depths (top to bottom).

51

Figure S4. Resolution tests for anisotropy strength using 1.5º x 1.5º checkerboard. The input model (top-left panel) has horizontally alternating anisotropy strengths shown by the colors representing perturbations of $\delta\gamma = \pm 0.03$ relative to a background anisotropy strength of $\gamma = 0.04$ and a fixed azimuthal angle of symmetry axis $\phi_f = 22.5^\circ$. The rest of the panels show recovered models using different damping factors (left to right) at different depths (top to bottom).
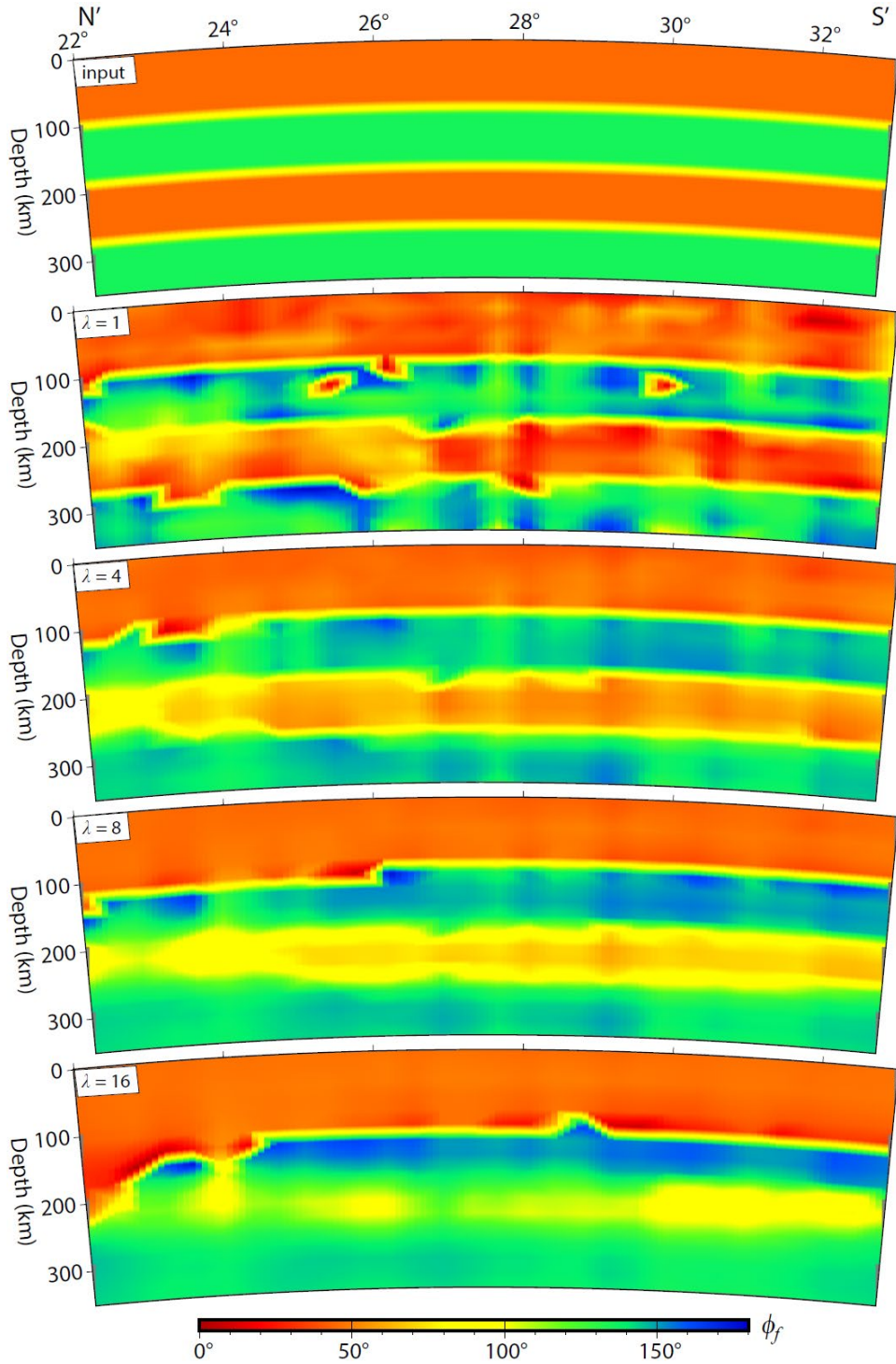
1

Figure S5. Resolution tests for an input model with 2 layers of different azimuthal angles of symmetry axes $\phi_f = 45°$ and $\phi_f = 135°$ but a fixed anisotropy strength of $\gamma = 4\%$. Shown here are the input models (top two panels) along the NS and N'S' cross-sections (see top-left panel in Figure 8 for the locations of the cross-sections) and recovered models for different damping factors λ (lower panels).
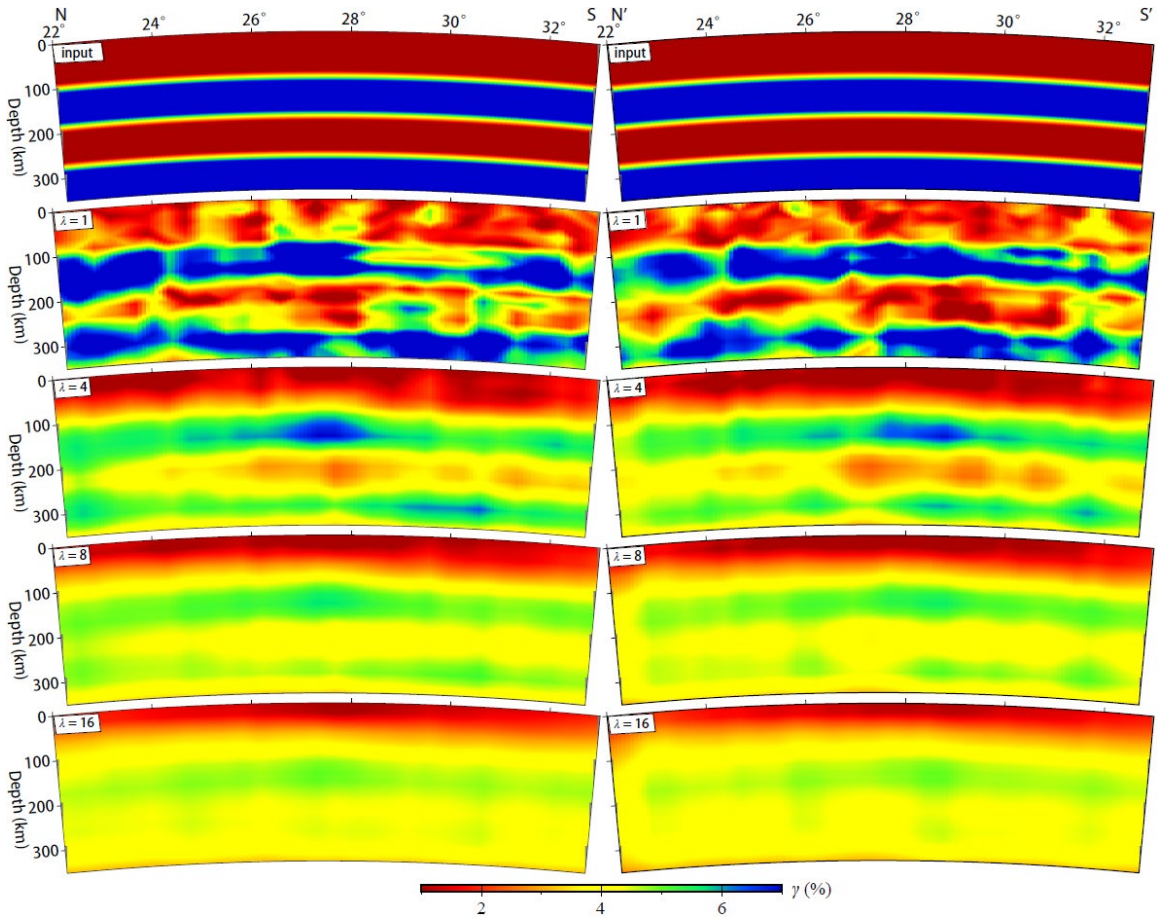
Figure S6. Resolution tests for an input model with 2 layers of different anisotropy strengths shown by the colors representing perturbations of $\delta\gamma = \pm0.03$ relative to a background anisotropy strength of $\gamma = 0.04$ and a fixed azimuthal angle of symmetry axis $\phi_f = 22.5°$. Shown here are the input models (top two panels) along the NS and N'S' cross-sections (see top-left panel in Figure 8 for the locations of the cross-sections) and recovered models for different damping factors λ (lower panels).

Figure S7. Resolution tests for an input model with 4 layers of alternating azimuthal angles of symmetry axes $\phi_f = 45°$ and $\phi_f = 135°$ but a fixed anisotropy strength of $\gamma = 4\%$. Shown here are the input model (top panel) along the N'S' cross-section (see top-left panel in Figure 8 for the location of the cross-section) and recovered models for different damping factors λ (lower panels).

Figure S8. Resolution tests for an input model with 4 layers of alternating anisotropy strengths shown by the colors representing perturbations of $\delta\gamma = \pm 0.03$ relative to a background anisotropy strength of $\gamma = 0.04$ and a fixed azimuthal angle of symmetry axis $\phi_f = 22.5°$. Shown here are the input models (top two panels) along the NS and N'S' cross-sections (see top-left panel in Figure 8 for the locations of the cross-sections) and recovered models for different damping factors λ (lower panels).